Linking Coastal Urbanization to Water Quality and Habitat Changes of the Upper Laguna Madre

A report funded by a Texas Coastal Management Program Grant approved by the Texas Land Commissioner pursuant to National Oceanic and Atmospheric Administration Award No. NA17NOS4190139

September 2019

Prepared by:
Hua Zhang, Principal Investigator
Paul Zimba, Co-Principal Investigator

Texas A&M University-Corpus Christi
6300 Ocean Dr., Unit 5797
Corpus Christi, Texas 78412
Phone: 361-825-2467
Email: hua.zhang@tamucc.edu

Submitted to:
Texas General Land Office
1700 Congress Ave.
Austin, TX 78701-1495

Table of Contents

Executive Summary

Globally, the population density of coastal areas is nearly three times that of inland areas, and coastal development is a proven threat to estuarine ecosystems. Impervious surface is an effective indicator of coastal development. Studies have shown that coastal areas with greater impervious coverage have exhibited higher nutrient loads, enlarged salinity range, increased peak flow, and accelerated habitat degradation. The Corpus Christi-Kingsville metropolitan area surrounding the Upper Laguna Madre (ULM) is a fast-growing coastal area in Texas. Since 1970, its population and impervious surface have increased by 52.9% and 44.5%, respectively. The population is projected to have a further 27.5% increase by 2050, indicating an unprecedented challenge to the management of freshwater inflow and estuarine resources. However, there is a lack of understanding of the coupled processes of urbanization, water quality, and habitat changes. First, the changes of land cover and land use often exhibit spatial heterogeneity, temporal nonlinearity, complex interactions with socioeconomic and ecological factors, and feedback to local zoning and taxation polices. Second, the applications of high-resolution aerial imagery in coastal mapping and assessment are hindered by the lack of effective methods for radiometric correction. Third, there is a lack of tools for quantitatively linking coastal human and environmental stresses to the responses of habitat and water quality and associated management strategies. Therefore, there is a need to apply advanced hydrological, geospatial, and data-driven techniques to develop cost-effective, robust tools for improving the assessment and management of water quality and habitat in urbanizing coastal regions.

This project aimed to qualitatively analyze the impact of long-term coastal development on water and habitat quality of ULM over the past four decades. Project activities consisted of several interlinked tasks over two years, starting with hydrological monitoring and analysis, transitioning into comprehensive remote sensing and predictive modeling, and culminating in outreach and decision support efforts. The hydrological monitoring efforts resulted in the establishment of the first evaporation pan station in ULM. Observations at this station provided essential information to estimate monthly evaporation rates in ULM. Such results were extended to adjust an existing state freshwater dataset that was based on evaporation stations outside UTM. The results led to the reconstructed monthly freshwater balance of ULM since January 1977. Long-term landscape changes in ULM and its neighborhoods were characterized using a combination of satellite and aerial imagery using Google Earth Engine. Ground truth was established based on data from field surveys using small unmanned aerial vehicles and historical images from the National Agriculture Imagery Program. We developed a hybrid method to estimate annual changes of impervious surface using the time series of Landsat imagery. It built seasonal composite images within a multi-year window, trained a classification model using multiple spectral predictors, and improved the initial classification results by temporal filtering. We further developed a pseudoinvariant near-infrared threshold (PINT) method for converting digital numbers into surface reflectance based on pseudoinvariant pixels identified from Landsat imagery. The extensive remote sensing efforts provided inputs to the development of different analytic models for analyzing urbanization-induced stress on estuarine water quality and habitat, including: (i) a nonlinear autoregressive network ensemble with exogenous inputs as a cost-effective tool to characterize nonlinear relationships; (ii) an integrated Markov-Chain Cellular-Automata model as a spatially-explicit tool to estimate the evolution of landscape. These predictive tools could generate future patterns of land cover and habitat under different scenarios of environmental change and socioeconomic development, providing essential information for the planning and management of coastal land and water resources. Finally, a set of decision support systems was established for enhancing the awareness of urbanization process and its impact on coastal ecosystems. Built on Google Earth Engine Apps, these decision support systems are publicly accessible to the world, and users can view and interact with the tools without the need to register for a Google Earth Engine account.

The achievements of this project highlighted the advantages of Google Earth Engine, a revolutionary geospatial tool that can process decadal satellite images through customized algorithms and cloud computation. The integration of Google Earth Engine, process-based models, and analytic tools provided a highly-efficient means to analyze the long-term spatiotemporal dynamics of linkages between impervious surface, freshwater fluxes, and estuarine health. Through providing new data and tools to better manage coastal land and water resources, this project could contribute to a sustainable development strategy that could provide needed jobs, stimulate economic activity, minimize the stress on coastal ecosystems, and ascertain the sources and timing of freshwater inflows needed to protect the quality and functions of coastal natural resource areas in ULM and other coastal regions.

1. Introduction

Over half the Earth's population now resides in cities (WHO, 2016). Population growth and urbanization rates in low elevation coastal zones are outpacing the demographic development of peri-urban regions (Neumann *et al.*, 2015). A characteristic indicator of urbanization is the increase of impervious surface, a unique land cover category that involves paved roads, sidewalks, parking lots, buildings, and other built structures, through which precipitation does not readily infiltrate into the underlying soil (Sexton *et al.*, 2013; Weng, 2012). Impervious surface affects hydrological and energy balances, as well as biological composition and ecosystem functions (Sexton *et al.*, 2013). Increase in impervious surface results in higher nutrient loads, increased hyposalinity impacts, elevated surface temperature, increased peak flow, and accelerated habitat degradation in many urban areas and watersheds (Arnold and Gibbons, 1996; Paul and Meyer, 2001), indicating the value of impervious surface as an effective indicator of environmental quality. Understanding the spatiotemporal pattern of impervious surface has important implications for studies of urban stormwater (Gobel *et al.*, 2007), urban heat islands (Imhoff *et al.*, 2010), water quality (Brabec *et al.*, 2002), ecosystem function (Meyer *et al.*, 2005), population growth (Lu *et al.*, 2006), and community resilience (Mignot *et al.*, 2006). Mapping and change detection of impervious surface provide critical information to city managers for a range of issues in environmental management and urban planning (Weng, 2012). This is particularly important for estuaries along the Gulf of Mexico, which represent the transition region between freshwater and marine systems, subjected to both terrestrial and oceanic processes by the gradients of salinity and nutrients present (Montagna *et al.*, 2011). Estuaries are ecologically and economically important to human society, with ~16% of our food produced in the ocean, and 85% of commercially important fish species dependent on estuaries for at least one life stage (NRC, 1997).

Understanding the patterns of coastal urbanization and its ecological and environmental implications is critical to the sustainability of Upper Laguna Madre (ULM), a long narrow bay that runs south from Corpus Christi Bay past Baffin Bay to the Land Cut. There are no significant freshwater flows or cuts from the Gulf of Mexico into the Laguna Madre, resulting in prevailing hypersaline conditions and a unique habitat for many important marine species. ULM is surrounded by flat coastal plains and barrier islands across five Texas counties: Nueces, Aransas, San Patricio, Kleberg, and Kenedy. Land elevation varies from sea level to 70 m with an average slope of 0.5%. Soils are mainly Victoria clay and Orelia fine sandy loam (Bumguardner *et al.*, 2013). Major crops include sorghum and cotton (Bumguardner *et al.*, 2013). Natural vegetation is dominated by woody and emergent herbaceous estuarine wetlands. This region has a humid subtropical climate with average annual precipitation and temperature of 805 mm and 22.3 °C, respectively. The local economy depends heavily on tourism and petroleum industry (Irish *et al.*, 2010). The Corpus Christi-Kingsville metropolitan area surrounding ULM is a fast-growing coastal area. The total population was 486,820 in 2016, with the City of Corpus Christi accounting for 67% of the total. The population has increased by 52.9% since the 1970s and a further increase of 27.5% is projected by 2050. Data from the NOAA Coastal Change Analysis Program indicate significant expansion in both high- and low-density development concomitant with population growth (Wetz *et al.*, 2016). The continuous growth of population and urban areas pose an unprecedented challenge to the management of coastal water, land, and biological resources. This challenge is particularly associated with the lack of scientific knowledge and tools in several aspects.

First, the changes of land cover and land use often exhibit spatial heterogeneity, temporal nonlinearity, complex interactions with socioeconomic and ecological factors, and feedback to local zoning and taxation polices. A variety of remote sensing methods have been proposed to characterize and quantify impervious surface from satellite imagery, which can be broadly divided into three categories: regression, unmixing, and classification. For example, Torbick and Corbiere (2015) employed the Classification And Regress Tree (CART) algorithm to map urban sprawl in the northeast United States and showed improvements compared to the National Land Cover Database (NLCD). Liu *et al.* (2018) developed a Normalized Urban Areas Composite Index by integrating three multispectral urban indices with nighttime light data and applied this new index at the global scale. Piyoosh and Ghosh (2017) enhanced the Biophysical Composition Index by incorporating the panchromatic band of Landsat 8 and a flexible search algorithm to determine the index threshold. A number of studies successfully used spectral mixing analysis (SMA), a process of decomposing the spectral signature of a mixed pixel into a set of end-members and their corresponding abundances (Kuang *et al.*, 2014; Shi and Wang, 2014; Xu *et al.*, 2018). Recently, a number of new technologies have been applied in impervious surface mapping, such as unmanned aerial vehicles (Gevaert *et al.*, 2017), LIDAR data (Hamedianfar *et* *al.*, 2014), cloud computation (Huang *et al.*, 2017), and deep learning (Wang *et al.*, 2015). While many global and national remotely-sensed land cover products include urban categories, they often have coarse spatial and/or temporal resolutions (Li *et al.*, 2015; Sexton *et al.*, 2013). Landsat imagery is often selected as source data for mapping impervious surface, mainly due to its availability since the 1980s, sufficient resolution for urban features, and stable revisiting frequency (Homer *et al.*, 2004; Midekisa *et al.*, 2017; Xian and Homer, 2010; Xu *et al.*, 2018). Milestone reviews on the remote sensing of impervious surface have been provided by Lu and Weng (2006), Weng (2012), and Li and Zhou (2017).

The classification accuracy of impervious surface is the lowest among all land cover categories at regional, national and global scales, averaging 40~70% in an assessment of the NCLD dataset (Wickham *et al.*, 2013) and <30% in a recent global study (Gong *et al.*, 2013). The challenge of accurate impervious surface characterization is in the complex spectral, texture, spatial, and temporal characteristics of various development features, which are often presented in a latticework of soil and vegetation features. In particular, bare soils are often confused with impervious surface due to their similar texture and spectral characteristics. It is difficult to differentiate them visually or using the thresholds of existing urban indices (Li *et al.*, 2017; Piyoosh and Ghosh, 2017). The misclassification of bare land resulted in noisy, salt-and-pepper appearances in the NLCD maps of fractional impervious cover (Sun *et al.*, 2017). Also, per-pixel classification methods assign each pixel to only one land cover category and all categories are mutually exclusive. These *hard* classifiers must compartmentalize mixed pixels, a common problem in residential areas on medium and coarse spatial resolution images having single pixels representing buildings, roads, trees, lawns, and water (Weng, 2012). Subpixel *soft* classifiers have been proposed to address this problem (Hu and Weng, 2011; Lee and Lathrop, 2006), but their implementation generally requires high-resolution training data to fully reflect the subpixel fractions of the various impervious surface. Furthermore, most classifications are implemented for one image at a time or a composite image from stacked images. As the temporal sequence of different images are not necessarily incorporated in the classification process, inconsistency between classification results cannot be avoided. For example, impervious area identified in one year might classify as pervious area in a subsequent year in areas where this change is unrealistic (Gray and Song, 2013; Mertes *et al.*, 2015; Schneider and Mertes, 2014). Heuristic approaches, applied temporally, are needed to ensure the consistency and stability of the time series of land cover maps (Li *et al.*, 2015). The difficulty with impervious area mapping is further complicated in coastal regions, where significant interfering cloud, sparse vegetation and tidal water levels introduce additional uncertainties into the interpretation of multi-temporal satellite imagery.

Second, the applications of high-resolution aerial imagery in coastal mapping and assessment are hindered by the lack of radiometric correction approaches. The National Agriculture Imagery Program (NAIP) data are available nationwide at the spatial resolution of 0.6 to 2 meters with very low cloud coverage and consists of repeat images in the growing season with 2- or 3-year cycles for more than 15 years (Maxwell *et al.*, 2017). It has been a unique choice for a variety of geospatial mapping applications in coastal regions, such as analysis of land cover and land use change (Nagel and Yuan, 2016; Shapero *et al.*, 2017; Singh *et al.*, 2018), evaluation of ecosystem services (Anderson *et al.*, 2016; Byrd *et al.*, 2018; Woodward *et al.*, 2018), monitoring of forest health (Bishop *et al.*, 2014; Hart and Veblen, 2015; Hartfield and van Leeuwen, 2018; Liu *et al.*, 2017), and assessment of urban green infrastructure (Lee, 2017; Ucar *et al.*, 2018). The NAIP imagery will likely continue to be the one of the best data sources for many research and operational efforts that need high-resolution multispectral imagery for feature extraction, change detection, or collection of ground truth for validate coarse-resolution satellite products.

While available with low or no cost, the NAIP data have not been recognized and utilized as effectively as one might expect, since important challenges in data preprocessing have hindered the exploration of this often-overlooked valuable data (Maxwell *et al.*, 2017). Compared to satellite imagery programs such as Landsat and MODIS, the NAIP data are acquired from aerial platforms using different sensors that have lower radiometric resolutions and the information on sensor characteristics is less available and consistent over time (Maxwell *et al.*, 2017). Because of the small swath of NAIP images (approximately 7 km × 8 km), the acquisition of imagery for one region usually involves multiple flights that may last weeks or potentially even months, and the mosaics of NAIP images have artifacts associated with atmospheric interference, viewing geometry, illumination, shadows, time of the day, and plant phenology (Hogland *et al.*, 2018; Maxwell *et al.*, 2017). More importantly, NAIP images are distributed in the format of digital numbers (DNs), which are integer values to facilitate computation and transmission and to scale brightness for convenient display (Campbell and Wynne, 2011). The number of brightness values within a DN image is determined by the number of bits (e.g., 256 values for an 8-bit NAIP image) available. DNs only express relative brightness within the scene, but they lack the physical units that are necessary to understand the optical processes behind the observed brightness and the interference of atmosphere. Due to the differences in acquisition times and dates, DNs can vary between adjacent image tiles (Maxwell *et al.*, 2017). DNs cannot be directly used to examine brightness over time, to match one scene with another, to prepare mosaic of large regions, nor to serve models of physical processes such as those in agriculture, forestry, and hydrology (Campbell and Wynne, 2011). The conversion from DNs to surface reflectance is increasingly understood as a minimum standard for analysis ready data in order to ensure consistency when comparing images over time and from different sensors (Wulder *et al.*, 2019). This is important to the calculations of many multispectral indices, such as the Normalized Difference Vegetation Index (NDVI) and the Normalized Difference Water Index (NDWI), which are very sensitive to atmospheric effects. However, many studies directly applied NAIP without correction for spectral analysis such as surface water mapping, land cover classification and vegetation cover estimation (Byrd *et al.*, 2018; Hart and Veblen, 2015; Hartfield and van Leeuwen, 2018; Hogland *et al.*, 2018; Lee, 2017; Liu *et al.*, 2017; Nagel and Yuan, 2016; Shapero *et al.*, 2017; Ucar *et al.*, 2018; Wu *et al.*, 2019). This is mainly due to a lack of easy access to radiometric response data for the sensors used and the lack of methods for retrieving surface reflectance from NAIP DN values (Maxwell *et al.*, 2017).

Third, there is a lack of effective methods for linking coastal human and environmental stresses to the responses of habitat and water quality and associated management strategies. Analytic methods have been substantially advanced for simulating processes of streamflow, groundwater discharge, evaporation, and storms at different scales, as well as examining the impacts of human interventions on such processes. The major challenge, however, lies in quantitatively translating freshwater changes to geochemical and biological responses of an estuarine ecosystem (Montagna *et al.*, 2011). Different methods have been developed to deal with this challenge, and preference has been generally given to various statistical regression approaches and process-based hydrodynamic and ecological models that involve inflow as a component (Gillson, 2011; Kim and Montagna, 2012; Powell *et al.*, 2002; Qiu and Wan, 2013; Robins *et al.*, 2005; Sun and Koch, 2001; Yáñez-Arancibia and Day, 2004). However, the development, configuration and calibration of these models are often associated with substantial data requirements, time commitment, and specialized personnel. Such demands often exceed the expectation of decision makers that require a quick turnaround time in comparing the impacts of different strategies.

Artificial intelligence approaches such as artificial neural networks (ANN) are efficient tools to characterize nonlinear stress-response relationships in a variety of complex environmental systems, such as oyster norovirus outbreaks (Wang and Deng, 2016), fish abundance (Froeschke *et al.*, 2013), $PM_{2.5}$ exposures (Di *et al.*, 2016), occurrence of toxic algal blooms in the Great Lakes (Millie *et al.*, 2012), and suspended sediment load (Melesse *et al.*, 2011). These studies have shown that ANN models are efficient data-driven methods that can produce output with comparable or better performance than other methods including physically process-based models, with substantially less data and time requirements. ANN models perform best when all patterns contained in the available data are included in the training set and the models are not used to extrapolate beyond the range of the training data (Maier *et al.*, 2010). Hansen and Salamon (1990) originally described multiple neural networks. Their use as an ensemble is an effective way to improve model performance (Chan and Paelinckx, 2008; Granitto *et al.*, 2005; Shu and Burn, 2004; Zhou *et al.*, 2002). The ability of ANN ensembles to analyze the impacts of freshwater inflow on estuarine water quality and ecosystems is a new application. More importantly, previous studies have not considered the combined effects of freshwater inflow, precipitation, and evaporation. Such knowledge gaps have been a critical obstacle to the development, implementation and evaluation of freshwater polices (Buzzelli *et al.*, 2014; Gillson, 2011; Ji and Chang, 2005; Robins *et al.*, 2005). Without a reliable and efficient tool to determine the freshwater need of biota, ill-regulated freshwater process could result in inadequate inflow with severe damage to fishery or excessive water release that might hinder the prosperity of other water-intensive economic sectors. Ecological damage resulting from reduced food resources, such as blue-crab and fish for migratory birds such as whooping cranes or piping plovers, can be manifested by reduced reproductive success the following year (Milne, 1976).

Current freshwater inflow management policies for ULM is established within the context of an estuarine freshwater balance that accounts for both freshwater inputs and losses. Freshwater losses are dominated by evaporation from open water surface and the estimated total evaporation in ULM often exceeds the total freshwater inputs (i.e., precipitation and surface inflows). However, current evaporation estimates rely on inland stations that do not reflect the unique hydrological, geophysical, and climatic conditions of ULM that can affect evaporation. For example, compared to inland areas, ULM has both higher wind speed that enhances evaporation and high salinity that reduces evaporation. A local evaporation station will improve the understanding of the combined effects of these processes and contribute to the development of a more robust freshwater balance in ULM. Second, the determination of freshwater requirement depends on the quantification of the responses of estuarine water and habitat quality to freshwater flux variations. This has been mostly achieved through establishing linear or nonlinear regression models for individual species or water quality parameters, as demonstrated in the landmark TxEMP model. Google Earth Engine is a revolutionary data mining tool that can process decadal satellite images through customized algorithms and cloud computation. The integration of Google Earth Engine and artificial intelligence methods could provide a highly-efficient means to analyze the spatiotemporal dynamics of linkages between impervious coverage, freshwater fluxes, and estuarine health status conditions over the long term.

Therefore, this project was aimed to qualitatively analyze the impact of coastal development in the Corpus Christi-Kingsville metropolitan area on water and habitat quality of ULM for the past four decades. The objectives of this projected included: i) establishing the first evaporation station in ULM and reconstruct the freshwater balance of this estuary; ii) characterizing landscape changes around ULM using high-resolution satellite and aerial images through Google Earth Engine; iii) analyzing urbanization-induced stress on estuarine water quality and habitat using hybrid artificial intelligence, geospatial, and statistical methods; and (iv) developing decision support systems to facilitate the quantitative assessment of urbanization process and its impact on coastal habitat over long term. Based on GIS-aided platforms, the project findings could contribute to a variety of education and outreach efforts and provide scientific support to state agencies (TWDB, TCEQ and TPWD) and local decision makers in ULM and other coastal regions.

2. Hydrological Monitoring and Analysis

2.1 Estimation of evaporation rate

A pan evaporation monitoring station (27˚32’38.18”N, 97˚17’03.26”W) was established in November 2017. As shown in Figure 2-1, it is the only pan evaporation station located in the Upper Laguna Madre and compliments the coverage of two existing pan evaporation stations managed by Texas Water Development Board (TWDB) for this region. As shown in Figures 2-2 to 2-3, the main facilities of this station includes consisted of: (i) two standard Class-A evaporation pans equipped with analog gauge and autofill systems (Nova Lynx, Grass Valley, CA) for comparing evaporation rates from freshwater and estuarine water, respectively; and (ii) a wireless Vantage Pro 2 weather station (Davis Instruments, Hayward, CA) that monitors rain, wind speed and direction, temperature, humidity sensors, ultraviolet radiation, and solar radiation in a rugged sensor suite (Figure 2-3).

The evaporation pans were cylinders made of stainless steel. Each pan had a diameter of 120 cm and a depth of 25 cm. The pans was placed on a carefully leveled, wooden base that was away from bushes, trees, and other obstacles which obstruct a natural air flow around the pans, thus representing open water in an open area. For each pan, an analog output evaporation gauge was used to determine the evaporation rate by measuring the changing water level in an evaporation pan. The gauge consisted of a float, pulley, and counterweight attached to a 1000-ohm potentiometer mounted through a gear assembly in a weatherproof housing. The gauge connected to the pan using stainless steel pipe and fittings. The potentiometer was able to produce a resistance output proportional to the change of the position of the float, which was monitored using a voltage data logger with a system accuracy of ±0.25% over the 25-cm range. The logger was mounted in a waterproof enclosure attached to the outside of the evaporation gauge. The clear cover allowed viewing of the current evaporation pan level.

The pans were refilled using an autofill system. It consisted a digital electronic water timer and an automatic float valve. The water timer switches on in the early morning every two days , allowing water from an external water tank to flow into the pan by gravity. When the water depth reached 20 cm, the float valve would stop, and the timer would shut off until the next programmed day. The monitoring system was easy to use and maintain and provided two years of accurate and reliable measurements during the project period. If precipitation occurred, it was taken into account in calculating the evaporation at both hourly and daily levels. If the rainfall events resulted in the overflow of the pan, the data of the associated 24-hour period were excluded.

The integrated sensor suite of the weather station was placed on the wooden base of the evaporation pan. It consisted a rain collector, a temperature sensor, a humidity sensor, an anemometer, a solar radiation sensor, and an ultraviolet radiation sensor. Temperature and humidity sensors were mounted in a passive radiation shield to minimize the impact of solar radiation on sensor readings. The integrated sensor suite sent the data to a station console via a low-power radio. Placed inside the cabin of the Laguna Madre Field Station, the console recorded sensor data and provided graph and alarm functions for on-site data visualization.

Since November 2017 and throughout the project period, the station has been operated to automatically measure the pan evaporation rate at five-minute intervals and weather conditions at 30-minute intervals. Regular maintenance and data downloading were conducted by the Center for Coastal Studies at a monthly basis. Additional trips were implemented to replace system components in the case of device malfunction or weather extremes.

2.2 Reconstruction of freshwater balance

The rate of evaporation was considered as a function of temperature, humidity, wind, and other ambient conditions. Figures 2-4 to 2-9 show the hourly average condition of pan evaporation, air temperature, dew point, humidity, wind speed, and solar radiation, respectively, in different months from 2017 to 2019. The peak of evaporation (Figure 2-4) tended to occur in late afternoon across all months, which was consistent with high temperature (Figure 2-5) and strong wind (Figure 2-8).

Observed daily evaporation rates after quality control were compared to the records from an existing station located in Port Aransas, which was managed by University of Texas Marine Science Institute station (UTMSI). The data were further converted into quadrangular lake evaporation rates by multiplying the pan evaporation rates with the monthly pan-to-lake coefficients, following the guideline of TWDB. The resulted evaporation rates were multiplied by the water surface of ULM to yield the volumetric estimates of evaporation. Compared to existing estimates that were mainly based on the UTMSI station and other nearby stations outside ULM, the evaporation estimates derived from this project were higher in February, November, and December, but lower in January, April, May, June, August, and October (Figure 2-10). Applying the monthly evaporation rates of this project to historical data, the results provided the adjusted estimation of evaporation loss of ULM over the past four decades (Figure 2-11).

The revised evaporation dataset was coupled with TWDB precipitation and inflow datasets to reconstruct the monthly freshwater balance of the Upper Laguna Madre since 1970. The calculation of freshwater balance at the monthly scale took into consideration: (i) the estimates of combined freshwater inflow to the estuary, consisting of gaged inflows, ungagged inflows, returned flows, and diversions (Schoenbaechler *et al.*, 2011); (ii) precipitation on the water surface of the estuary; and (iii) adjusted evaporation from this project. The results of freshwater balance reconstruction consisted of monthly freshwater loss and gain since January 1977 (Figure 2-12), providing essential information to analyze the impact of hydrological controls on ecosystem system health.

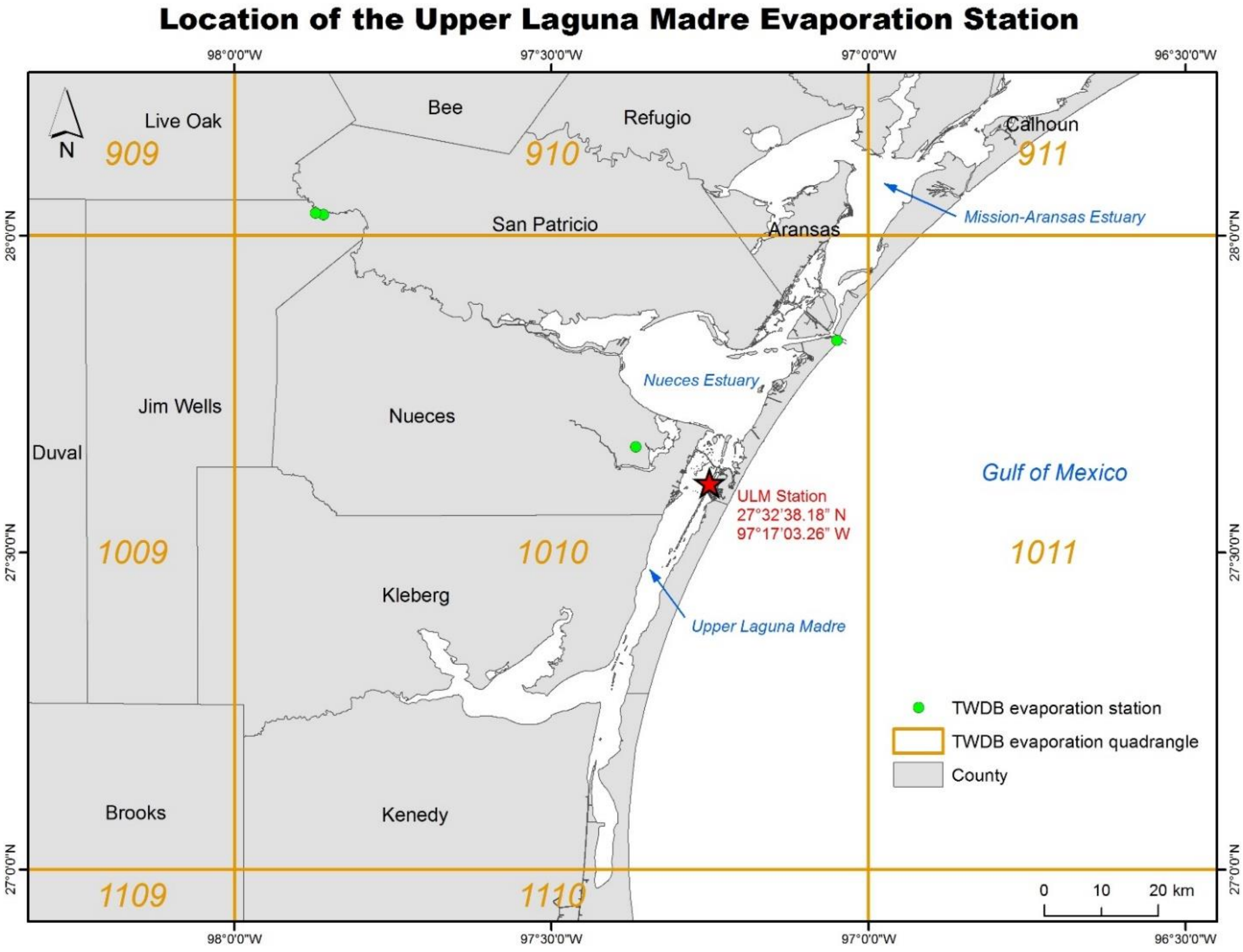

Figure 2-1. Map of the Laguna Madre Evaporation Station.

Figure 2-2. The construction of the Laguna Madre Evaporation Station.

Figure 2-3. The completed Laguna Madre Evaporation Station.

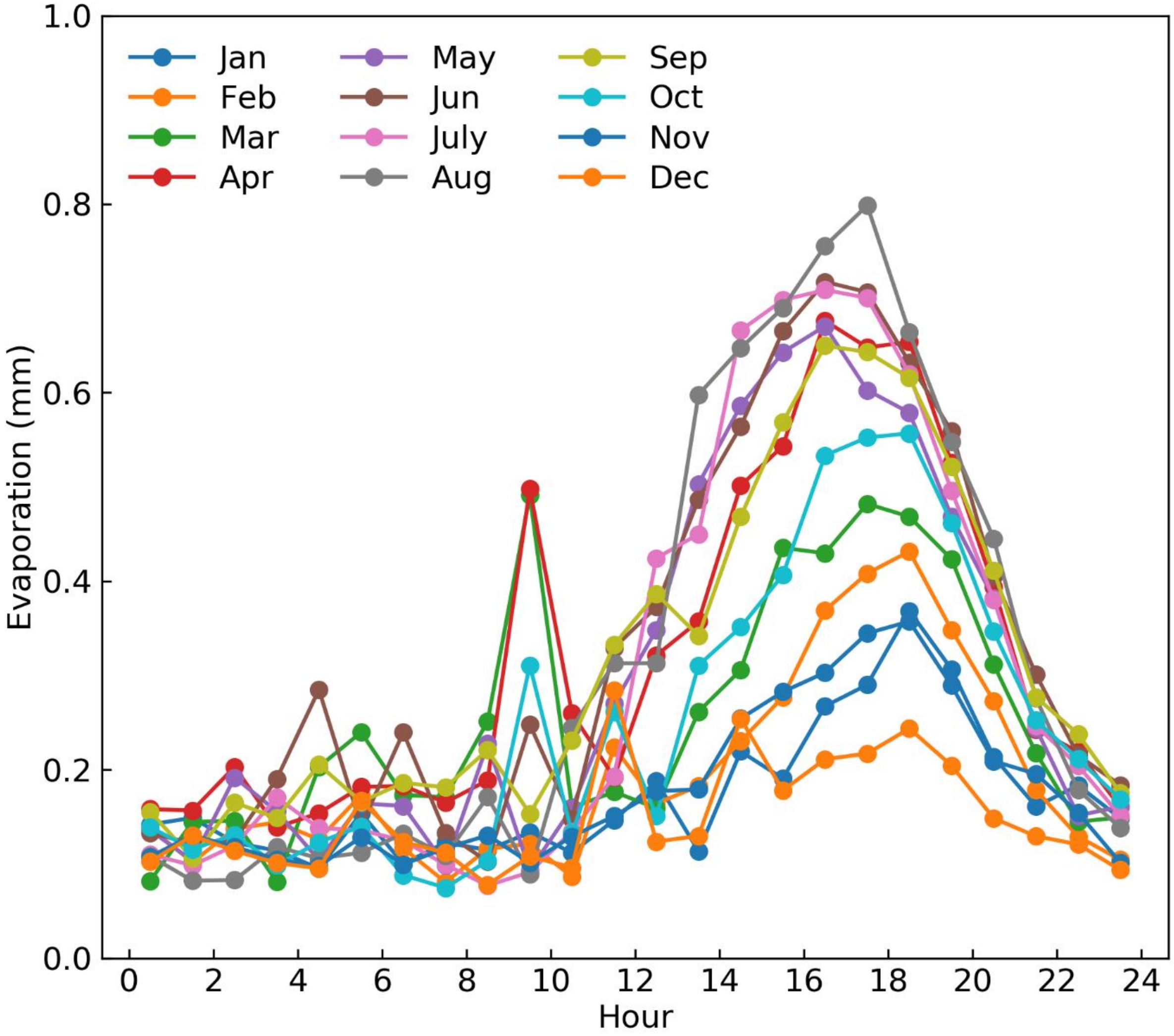

Figure 2-4. Hourly average pan evaporation of different months observed at the Laguna Madre Evaporation Station.

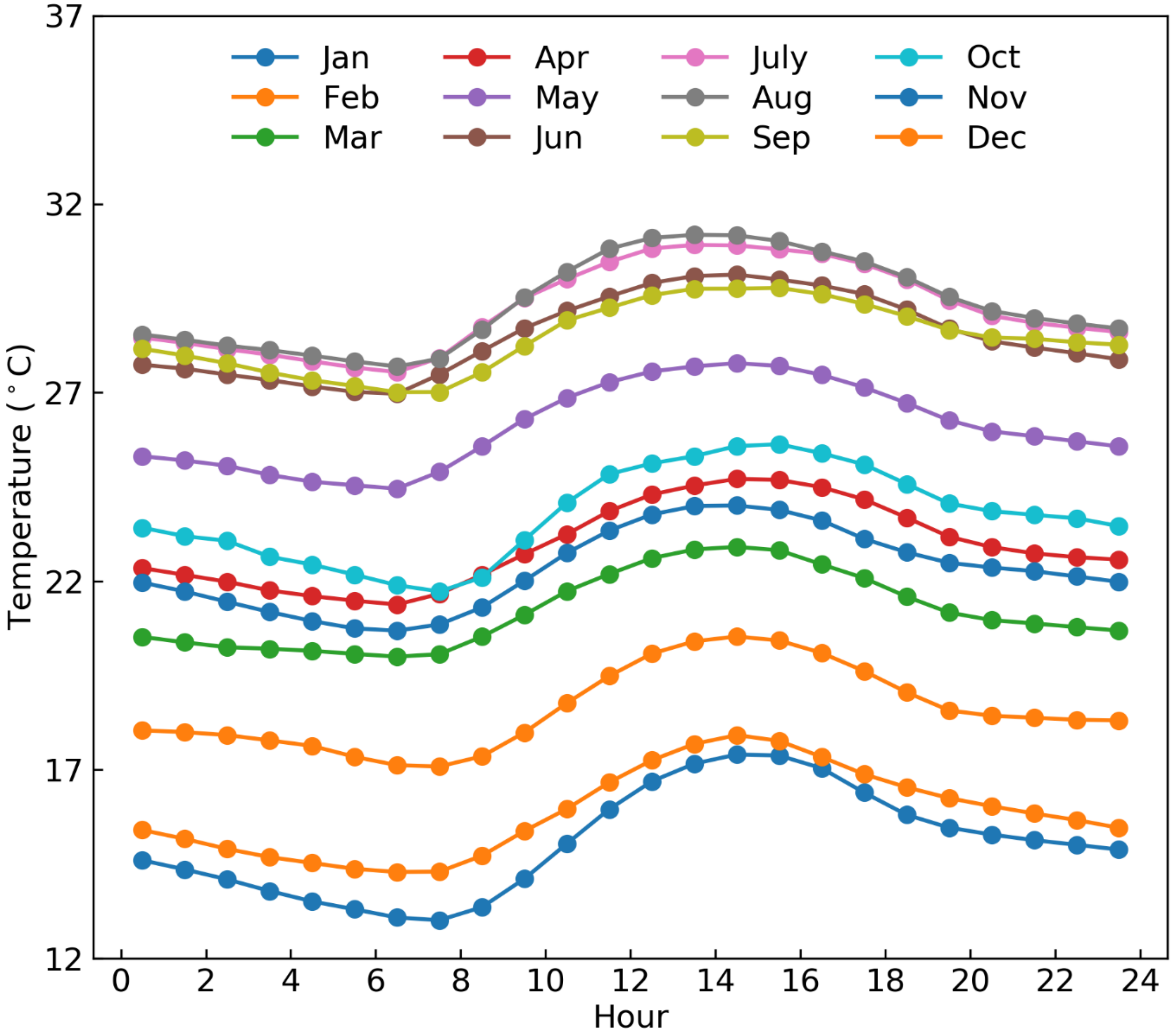

Figure 2-5. Hourly average temperature of different months observed at the Laguna Madre Evaporation Station.

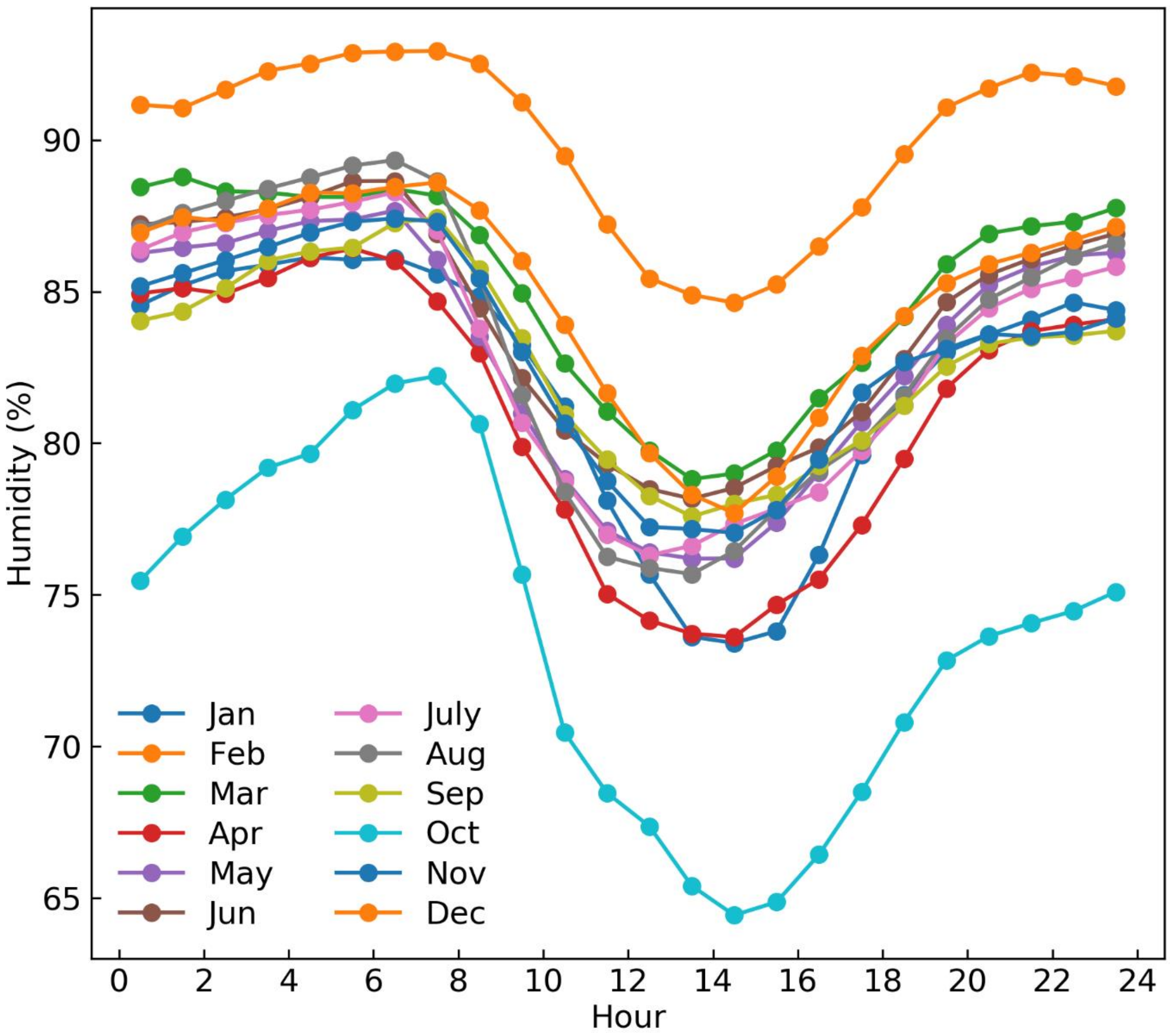

Figure 2-6. Hourly average humidity of different months observed at the Laguna Madre Evaporation Station.

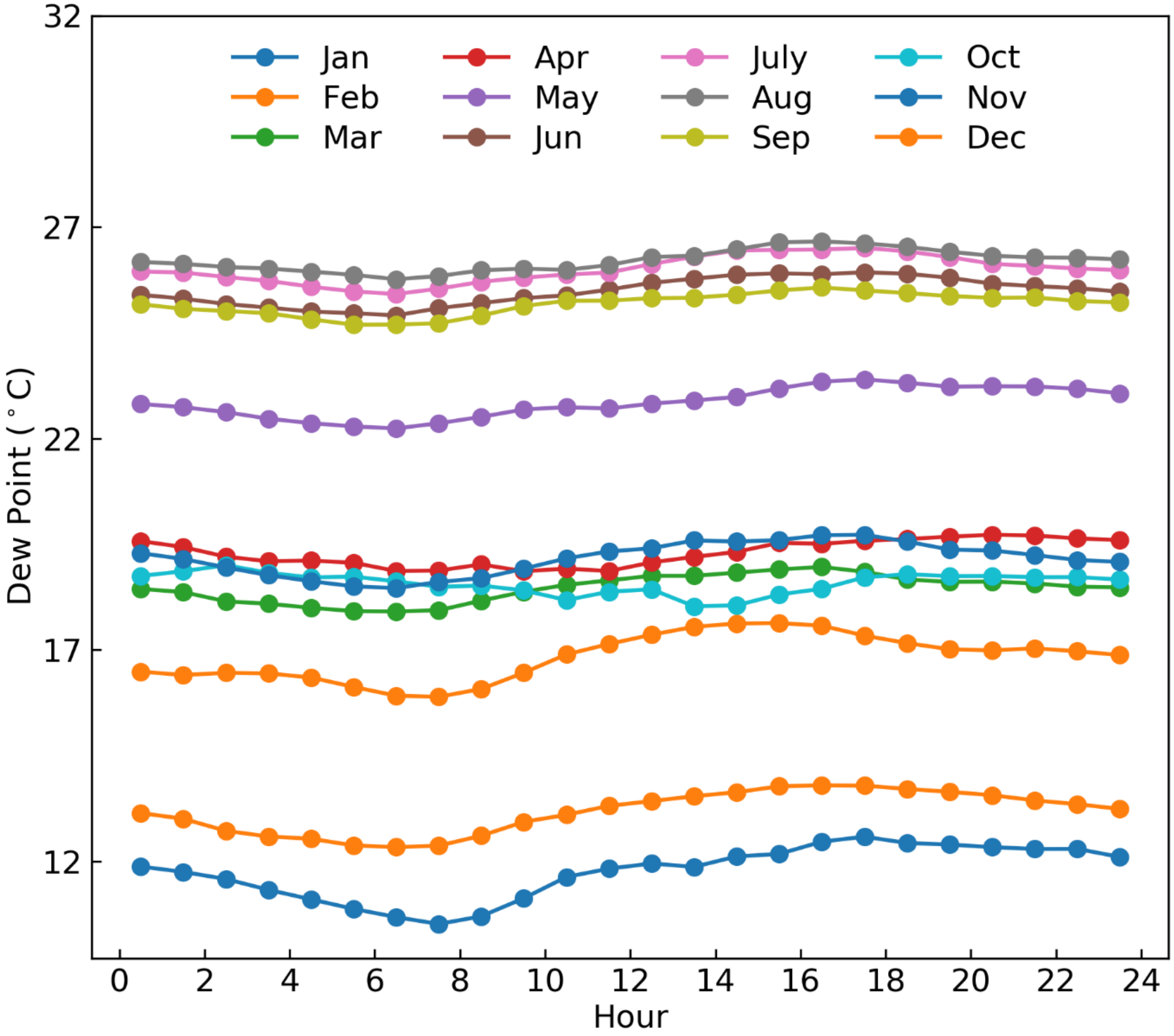

Figure 2-7. Hourly average dew point of different observed at the Laguna Madre Evaporation Station.

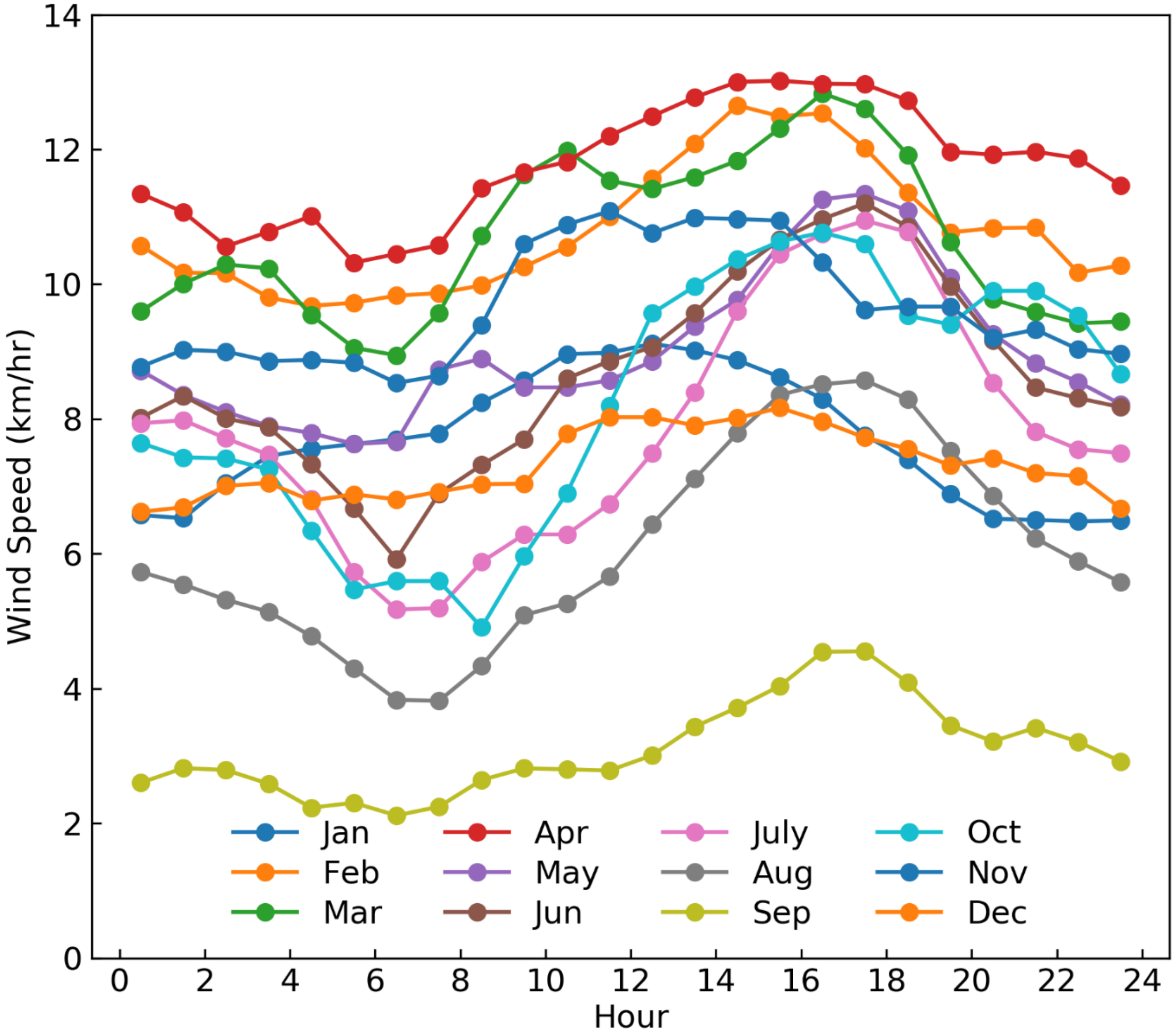

Figure 2-8. Hourly average wind speed of different months observed at the Laguna Madre Evaporation Station.

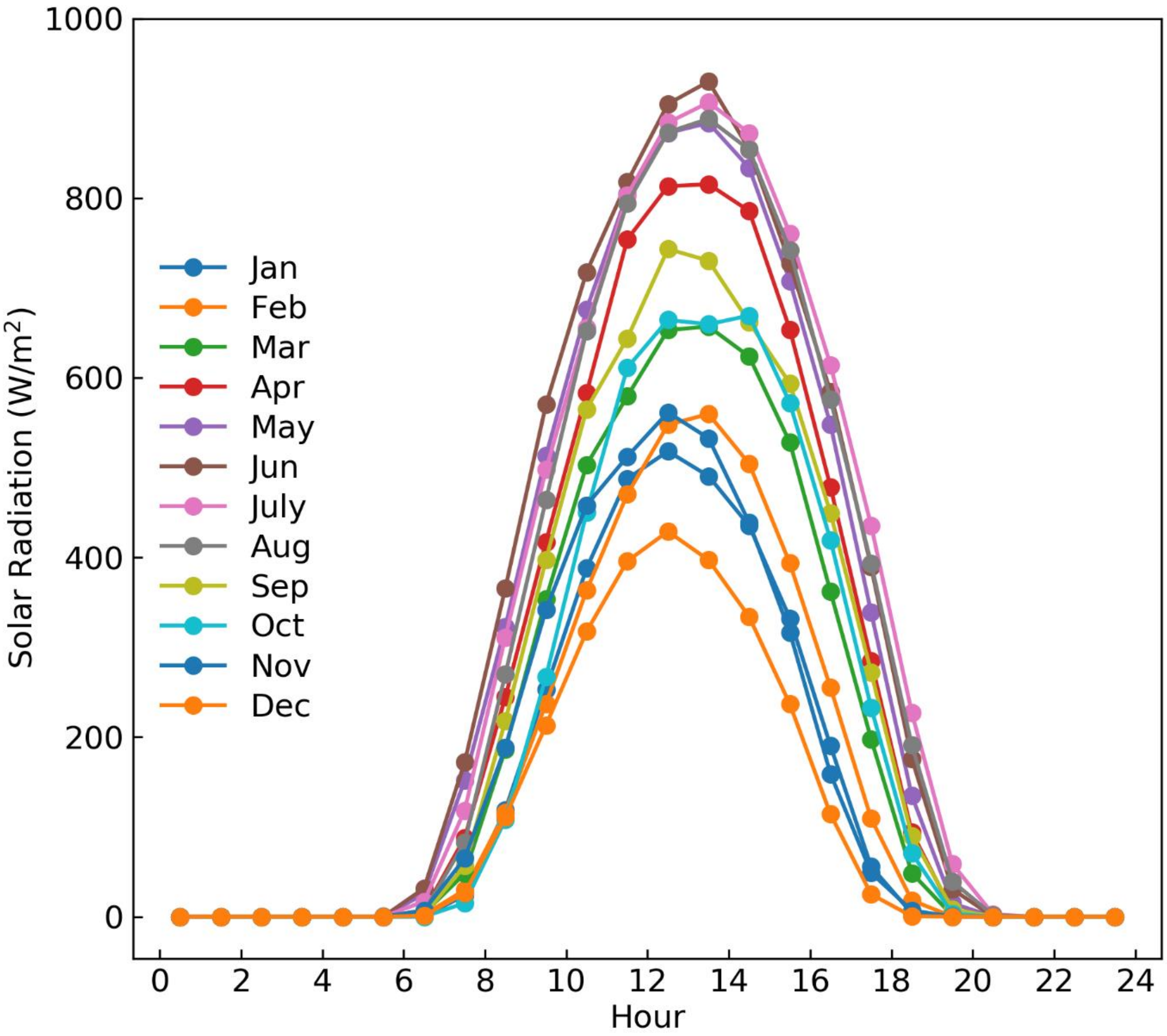

Figure 2-9. Hourly average solar radiation of different months observed at the Laguna Madre Evaporation Station.

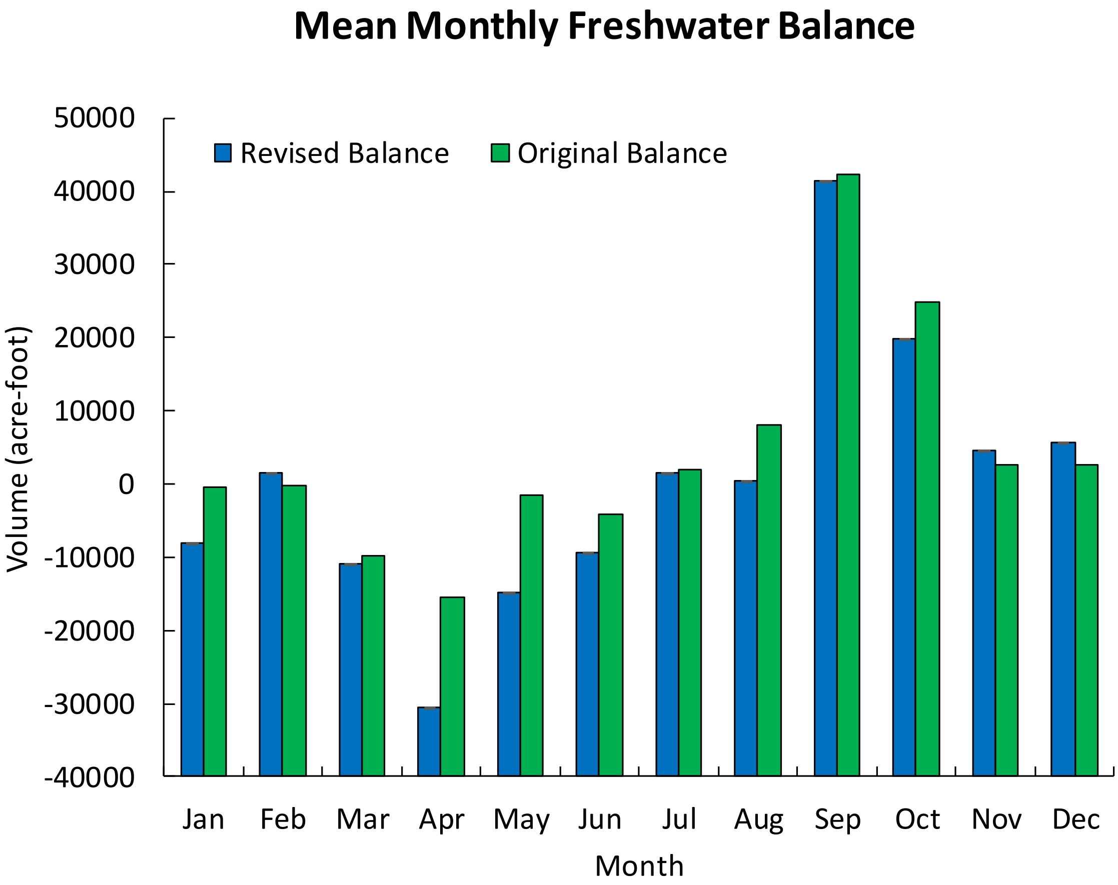

Figure 2-10. Comparison of original and revised average monthly evaporation in Upper Laguna Madre.

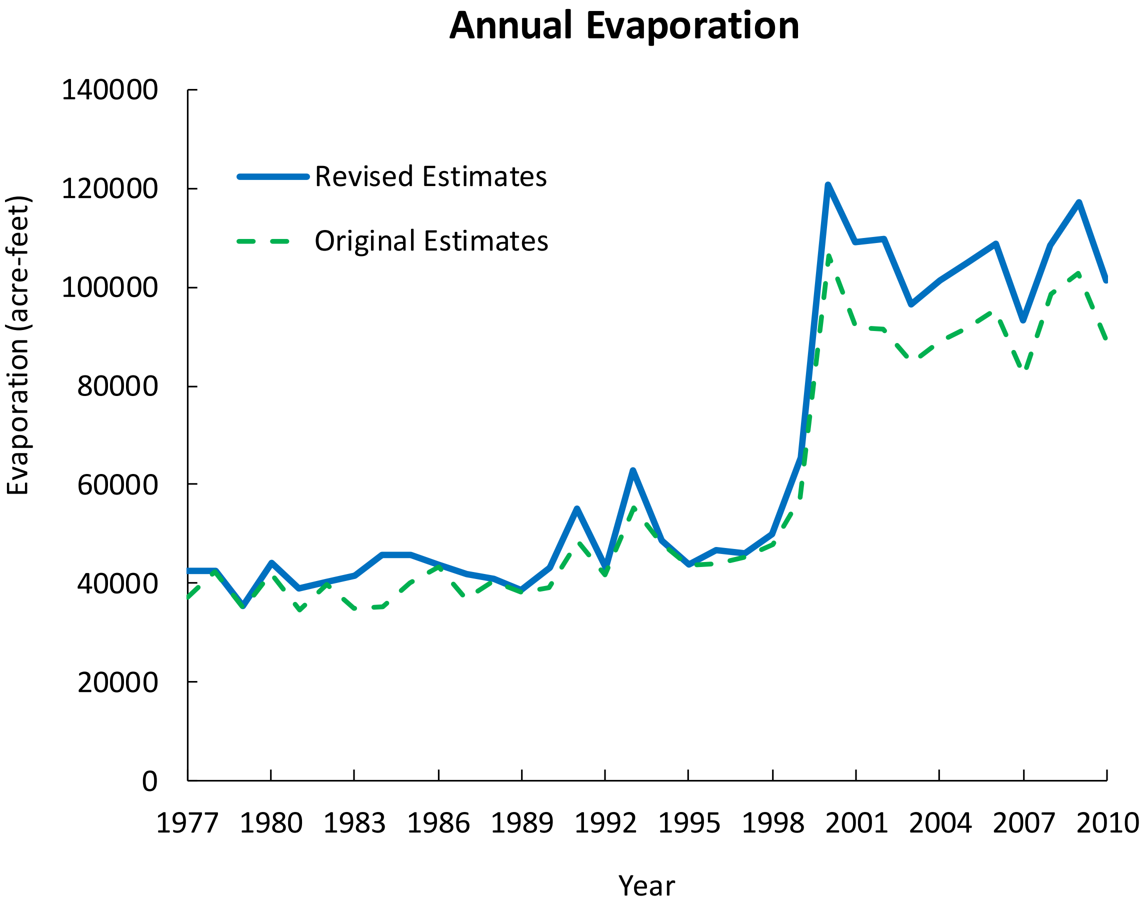

Figure 2-11. Revised annual freshwater balance of Upper Laguna Madre.

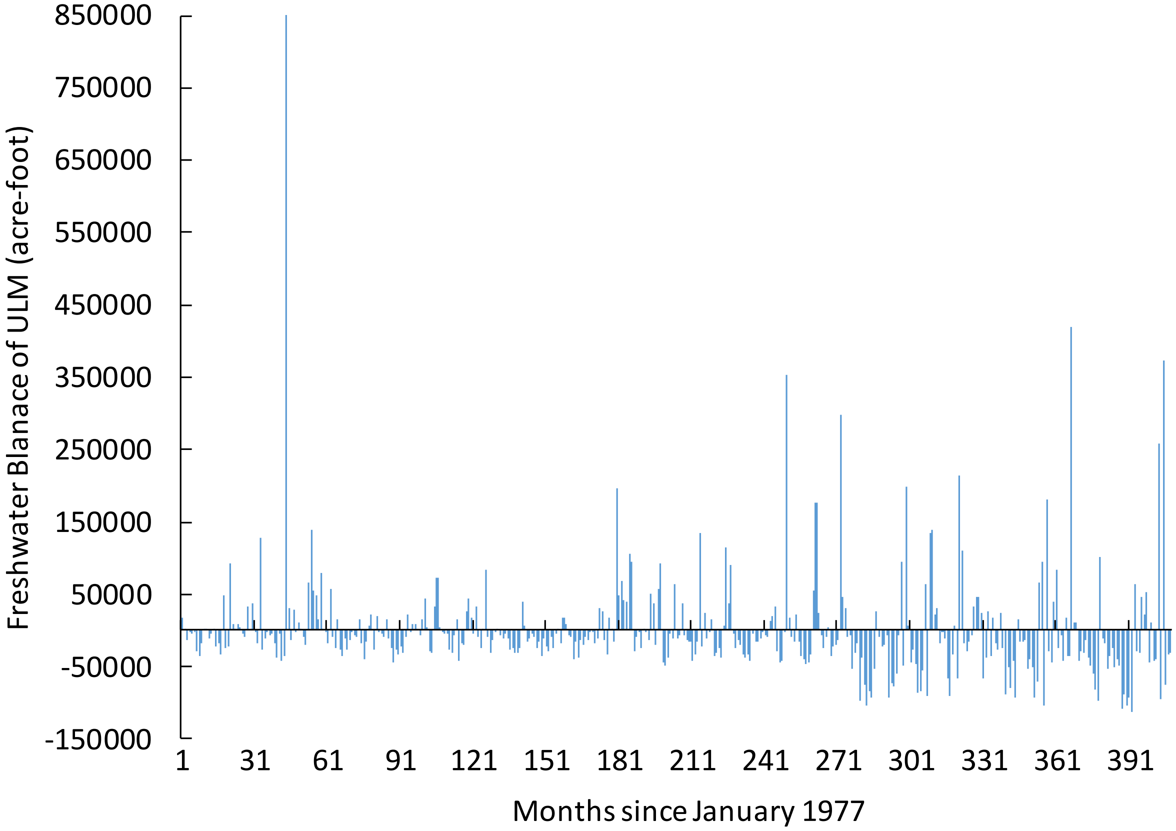

Figure 2-12. Revised monthly freshwater balance of Upper Laguna Madre.

3. Characterization of Coastal Land Cover and Habitat Changes

3.1. Generation of reference data

Pixel-level reference data were generated to represent different land cover and habitat categories in ULM (Figure 3-1) using high-resolution aerial images of the National Agriculture Imagery Program (NAIP). High-intensity impervious surface was defined as areas with high development intensity and >90% impervious surface coverage. These areas primarily consisted of highways, road intersections, large parking lots, and large buildings. Low-intensity impervious surface was defined as areas with low development intensity and impervious surface coverage of 50-90%. These were mainly residential areas with a heterogeneous mixture of impervious surface and vegetation. We also incorporated 1/3 arc-second USGS National Elevation Dataset to improve the delineation of coastal regions. The collection of reference data involved multiple field surveys and analysis of existing land cover datasets from National Wetland Inventory (NWI), National Land Cover Database (NLCD), Texas Natural Resource Information System (TNRIS), and Texas Statewide Seagrass Monitoring Program for the ground truth of different land cover and habitat categories.

We developed a stratified systematic semi-automatic method for developing reference data from aerial images. The study area was divided into uniform $0.05^{o} \times 0.05^{o}$ subregions and sampling pixels were generated for each land cover category in each subregion through several steps (Figure 3-2). First, the centroids of 30-m Landsat pixels were overlaid on the 1-m NAIP image. Second, the NAIP image was converted into a binary water/non-water layer using an NDWI threshold and the fractional vegetation cover (F_v) was calculated for each Landsat pixel. Among pixels with $F_v > 0.9$, three pixels were randomly chosen as samples for vegetation. Third, the NAIP image was converted into a binary vegetation/non-vegetation layer using an NDVI threshold and the fractional water cover (F_w) was calculated for each Landsat pixel. Among pixels with $F_w > 0.9$, three pixels were randomly chosen as samples for water. Fourth, among pixels with $F_v < 0.1$ and $F_w < 0.1$, six pixels were randomly chosen. These pixels were inspected and assigned as bare land or high-intensity impervious surface if appropriate. Finally, among pixels with $0.1 < F_v < 0.5$ and $F_w < 0.1$, three pixels were randomly chosen. These pixels were visually inspected to generate samples for low-intensity impervious surface. The stratified random sampling was implemented several times across the subregions to obtain enough samples. Using the NAIP images for 2008, a total of 1,583 sample pixels were obtained for the five land cover categories: water (218), vegetation (413), bare land (150), high-intensity impervious surface (361), and low-intensity impervious surface (362). Then the developed reference data were inspected using NAIP images of 2016 to update pixels with changed land cover, resulting in a new reference data set for 2016.

The NAIP-derived reference data for land cover and habitat changes were enhanced using ground surveys with the aid of small unmanned surface vehicles (UAVs). The project team deployed multiple platforms (e.g., Inspire 1, Mavic Pro, and Phantom 3) with RGB, near-infrared, and thermal infrared cameras to cover a variety of representative sites including impervious surface, marshes, seagrasses, and tidal flats (Figures 3-3 and 3-4). Ground control points were established using the new Trimble Catalyst technology with 0.3-m horizontal and vertical accuracies. Flight plans were developed using a combination of DroneDeploy and Pix4D Capture. Centimeter-level images were captured through flights at different altitudes, ranging from 20 m to 120 m. The images captured by UAVs were mosaicked using the structure from motion (SfM) technology in Pix4D Mapper (Figure 3-5). These orthomosaic images were upscaled to the resolution of the 30-m Landsat images to generate training samples for classification (Figures 3-6 and 3-7). More than 300 GB UAV data were generated from this project and significantly improved the quality of our land cover and habitat mapping efforts.

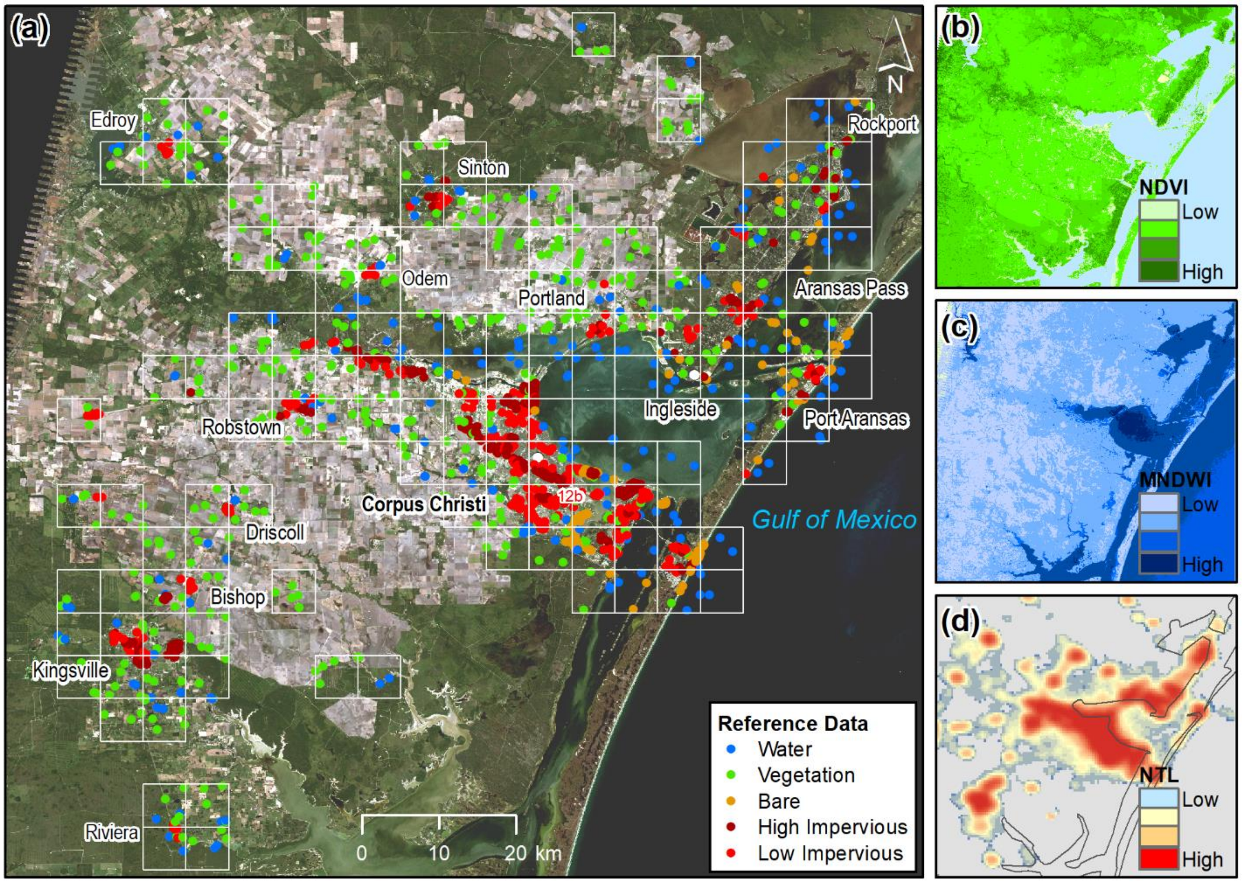

Figure 3-1. Reference data across the study area: (a) Landsat TM false color composite (bands 4, 3 and 2); (b) mean value of the normalized difference vegetation index (NDVI); (c) mean value of the modified normalized difference water index (MNDWI); (d) DMSP/OLS stable night-time light (NTL) data of 2013. White boxes in (a) indicate 0.05-degree subregions designed for obtaining reference data.

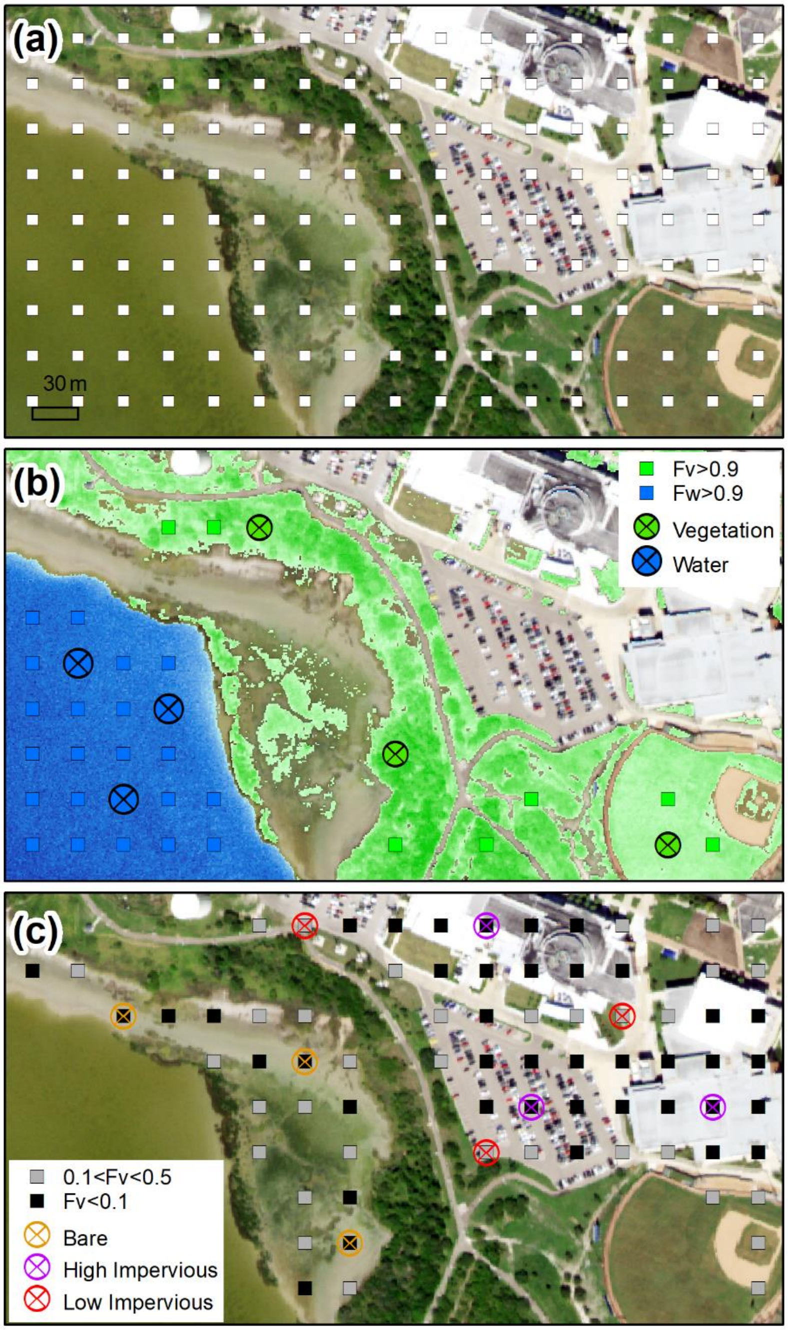

Fig. 3-2. Procedures for generating reference data from aerial imagery. (a) Centroids of 30-m Landsat pixels are overlaid on 1-m resolution NAIP imagery. (b) Pixels for water are randomly selected from pixels with fractional water coverage ($F_w > 0.9$). Pixels for vegetation are randomly selected from pixels with fractional vegetation coverage ($Fv > 0.9$). (c) Pixels for bare land and high impervious surface are selected from pixels with $F_v < 0.1$ and $F_w < 0.1$; pixels for low impervious surface are selected from pixels with $0.1 < F_v < 0.5$.

Figure 3-3. Field surveys for ground truthing at different sites.

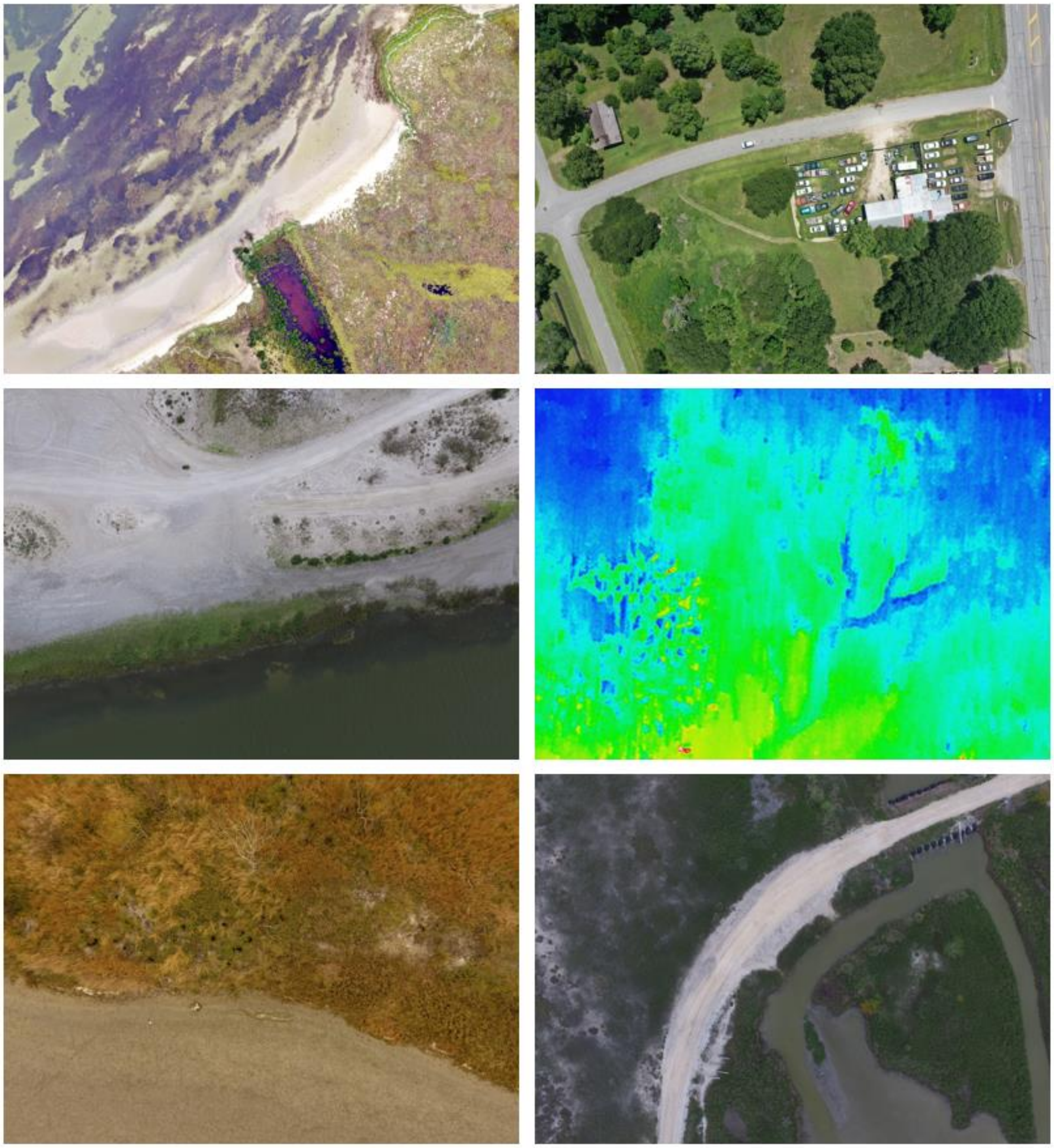

Figure 3-4. Examples of UAV images acquired at different sites.

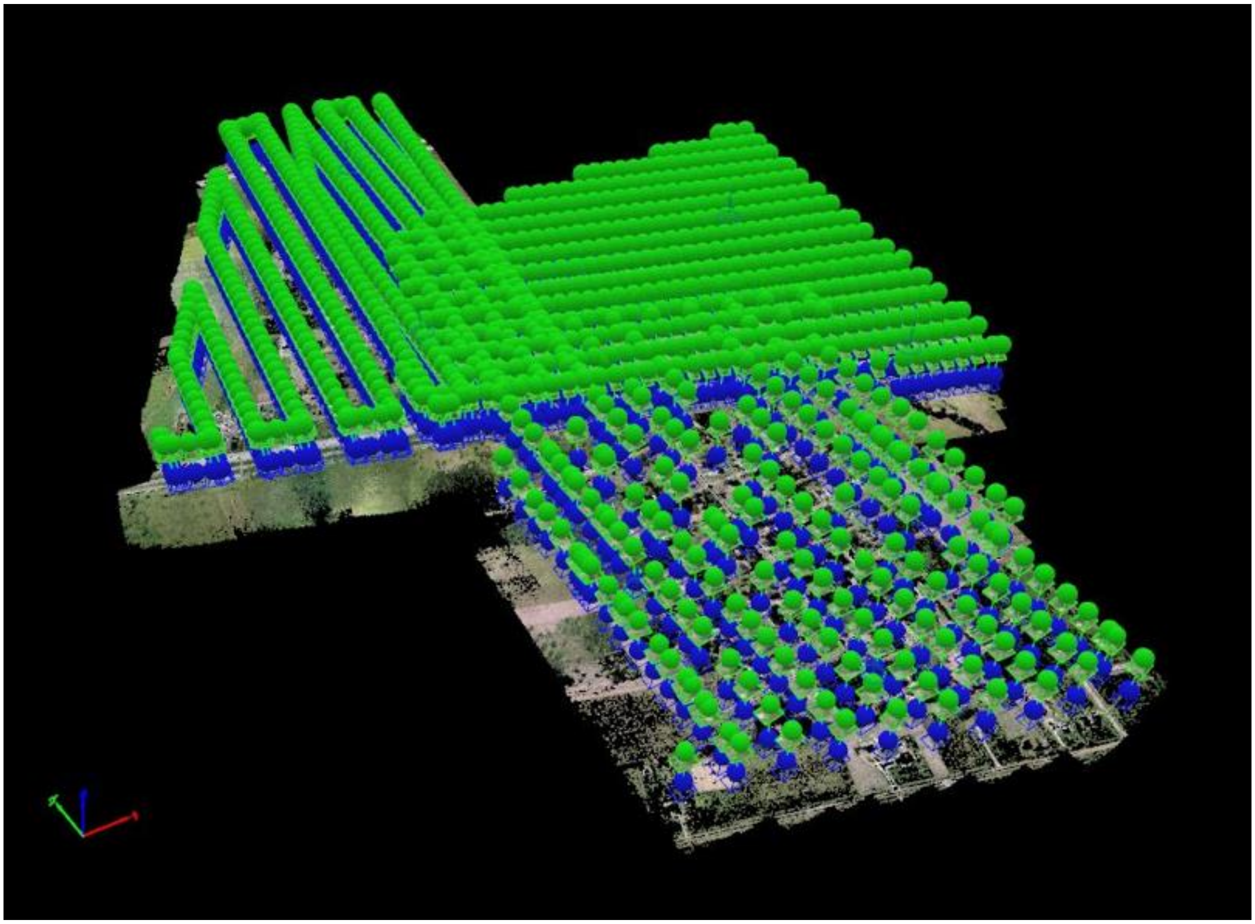

Figure 3-5. The processing of UAV images using the structure from motion (SfM) technology in Pix4D Mapper.

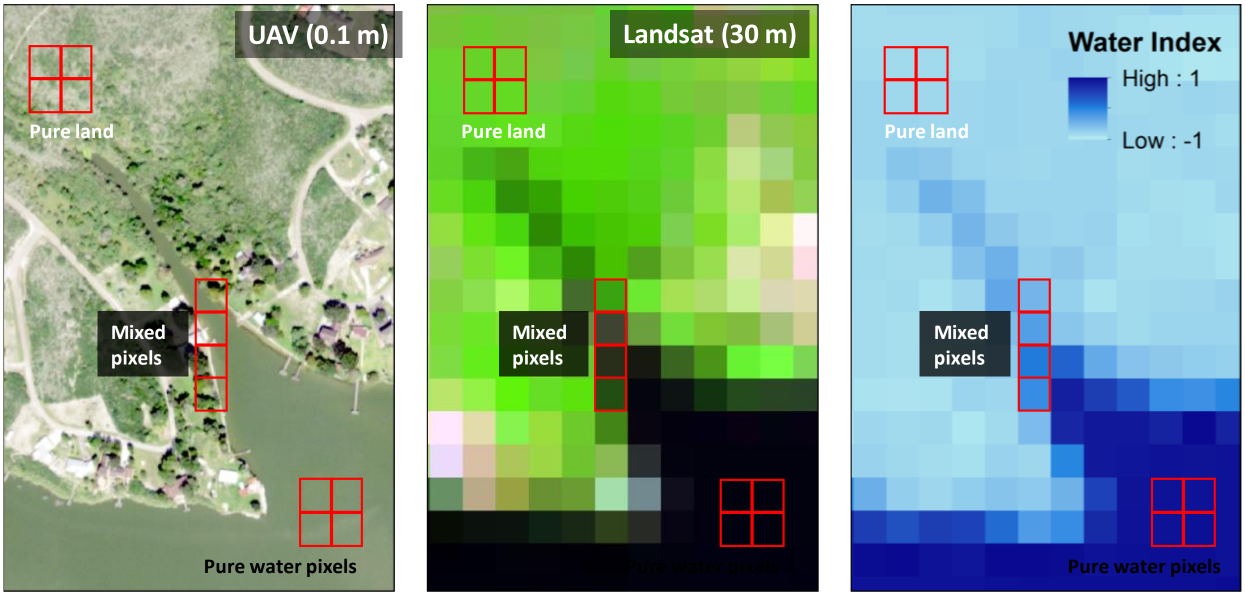

Figure 3-6. The establishment of sampling points through upscaling UAV data to the resolution of satellite images for water fraction.

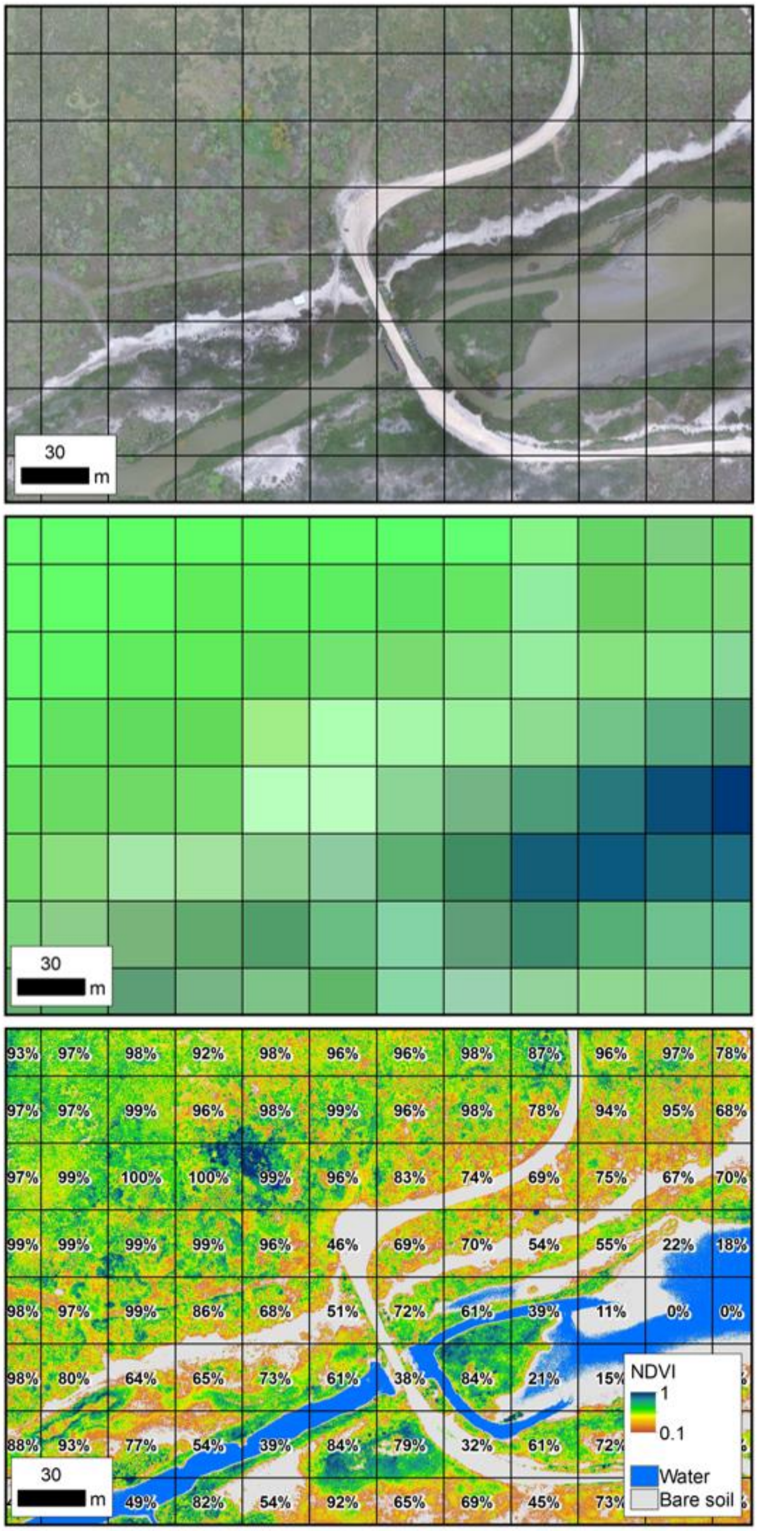

Figure 3-7. The establishment of sampling points through upscaling UAV data to the resolution of satellite images for vegetation fraction.

3.2 Analyzing land cover and habitat changes using a multisource imaging approach

We developed a hybrid method to estimate annual changes of impervious surface using the time series of Landsat images. It builds seasonal composite images within a multi-year window, trains a classification model using multiple spectral predictors, and improves the initial classification results by temporal filtering.

(1) Screening of satellite imagery

Landsat images were screened using a cloud cover threshold of 65%, the average global cloud cover over land (Foga *et al.*, 2017). Pixels covered by cloud and shadow were masked out. Images with acceptable cloud conditions were grouped based on seasons, defined using a ten-year time series of the Normalized Difference Vegetation Index (NDVI) (Rouse *et al.*, 1974) from MODerate-resolution Imaging Spectrometer (MODIS) images over vegetated pixels (Figure 3-8). Each calendar year was divided into two seasons: i) summer, from DOY 105 to DOY 227, and ii) winter, from DOY 1 to DOY 30 and from DOY 305 and 366 (Figure 3-9). Based on their acquisition dates, Landsat images were assigned to winter or summer groups. For the mapping of each year, the classification inputs included images in three consecutive summers and four consecutive winters across a five-year window centered on the targeted year. For example, the classification for year 2003 included images for the summers of 2002, 2003 and 2004 and images for the winters of 2001-2002, 2002-2003, 2003-2004, and 2004-2005. Images acquired between summers and winters (i.e., DOY 31- 104 and DOY 228-304) were removed as mapping of impervious surface tended to be more accurate with contrasting spectral response from green vegetation. On average, the classification for each year used 12.4 summer images and 10.1 winter images. The use of multi-annual seasonal groups for classification minimized the residual atmospheric effects of cloud contamination and reduced the phenological variations within the season (Sexton *et al.*, 2013). The years 2012 and 2013 were excluded due to the gap between Landsat 5 and Landsat 8 missions. The year 1989 was also excluded due to the lack of summer images.

(2) Generation of seasonal predictors

For the winter of each year, the median of each band was calculated from all available images. The use of median images instead of individual images minimized the effects of phenological variation and atmospheric correction. The median winter images were preprocessed through band-specific standardization and cross-band normalization for six bands with brightness temperature excluded. In the standardization process, pixel values in each band were divided by an a priori upper limit of that band (Sexton *et al.*, 2013). In the normalization process, the total reflectance in each pixel was calculated across six bands for each image and the pixel values were then divided by the across-band sum. Both standardization and normalization procedures have been used in remote sensing studies for transforming pixel values to a common dynamic range and reducing both within-class and inter-annual spectral variations (Luo *et al.*, 2014; Sexton *et al.*, 2013; Weng, 2012; Wu, 2004; Yang *et al.*, 2010). Figure 3-10 shows the mean surface reflectance of five land cover categories of reference data in the preprocessed median winter images. Water pixels were readily identified using the median winter surface reflectance due to the unique spectral signature of water in the short-wave infrared region.

The separation of other land cover categories was augmented by incorporating additional seasonal predictors. First, multispectral indices were calculated from the normalized surface reflectance to enhance the spectral contrast of impervious and pervious features. The selected indices included NDVI, the Modified Normalized Difference Vegetation Index (MNDWI) (Xu, 2006), and the Normalized Difference Built-up Index (NDBI) (Zha *et al.*, 2003). Specifically, the maximum summer NDVI, mean winter MDNWI, and mean winter NDBI were selected as seasonal predictors based on exhaustive comparisons of different statistical measures. As shown in the spectral space defined by these indices (Figure 3-10), the four land cover categories (excluding water) tend to form two groups. Low-intensity impervious surface and vegetation show a gradient of variable vegetation abundance, leading to strong positive NDVI values and negative MDNWI values. In contrast, high-intensity impervious surface and bare land were similar in the absence of vegetation, resulting in low NDVI values and neutral MDNWI and NDBI values. To further enhance the separation of high-intensity impervious surface from bright bare land, seasonal maximum brightness temperature was incorporated. High-intensity impervious surface tended to be warmer than bare soil, particularly in summer. The maximum temperature was used instead of the minimum or mean temperature to reduce the disturbance of clouds and shadows.

The predictors for each year were eventually constructed as an 11-band image, consisting of nine winter bands (i.e., six bands of normalized median surface reflectance, maximum brightness temperature, mean MNDWI, and mean NDBI) and two summer bands (i.e., maximum NDVI and maximum brightness temperature). The inclusion of summer median images did not improve classification performance. Also, this seasonal cluster procedure was not affected by the number of images available in each year, as the images were classified into seasonal groups and the predictors were either seasonal medians or maximum values. As long as the year contained enough images for calculating pixel-level median and maximum values, the input to the Random Forest model was always an 11-band composite image.

(3) Classification

Reference data were randomly assigned to training (70%) and validation (30%) datasets for developing a random forest (RF) classifier in Google Earth Engine (GEE). RF classifiers are efficient methods for per-pixel classification and have the advantages of small training time and easy parameterization (Heydari and Mountrakis, 2018; Midekisa *et al.*, 2017). We set the number of decision trees to 50, the bag fraction to 0.5, the minimum leaf size to 1, and the number of randomly-selected features at each node as 4. Classification accuracy was evaluated using a confusion matrix. Results of sensitivity tests indicate that 50 decision trees were sufficient for differentiating five land cover categories and that employing more decision trees resulted in little improvement of classification performance. RF parameters were very stable and the difference of classification accuracy was about 1% between the worst and the best parameter configurations (Pelletier *et al.*, 2016). The trained classifier was applied to the predictor images to retrieve initial estimates of annual areas of impervious surface from 1984 to 2017.

(4) Temporal filtering

We developed a temporally consistent approach to correct satellite-derived impervious surface using a set of pixel-level change detection and correction rules. This approach could reduce temporal inconsistency in the results of classification performed separately for each year for land cover change analysis. For example, a pixel could switch between impervious and pervious conditions multiple times. This type of problems could be caused by spectral similarity: (i) between high-intensity impervious surface and bright bare land, particularly near the shorelines of estuaries or large inland water bodies, and (ii) between low-intensity impervious surface and vegetation, particularly in residential areas with single houses and ample vegetation cover. We assume that that the conversion from pervious surfaces to impervious surface is irreversible. The following rules were applied within a time window of *n* years to modify pixel values (Figure 3-11):

(a) If a bare land pixel is classified as high-intensity impervious surface at least once in n preceding years and at least once in n subsequent years, this pixel is updated as high-intensity impervious surface in the current year;

(b) If a vegetation pixel is classified as low-intensity impervious surface at least once in n preceding years and at least once in n subsequent years, this pixel is updated as low-intensity impervious surface in the current year;

(c) If a high-intensity impervious surface is classified as neither high-intensity impervious surface nor low-intensity impervious surface in n subsequent years, this pixel is updated as bright bare land, unless this pixel is classified as impervious surface for >90% of the study period;

(d) If a low-intensity impervious surface is classified as neither high-intensity impervious surface nor low-intensity impervious surface in n subsequent years, this pixel is updated as vegetation, unless this pixel is classified as impervious surface for >90% of the study period.

Rules (a) and (b) were developed to correct for errors of omission. They were implemented together for each year of the time series. The process was repeated again once after all years were corrected. Rules (c) and (d) were developed to correct for errors of commission. They were executed together through a moving window, starting from the most recent year for only one pass. Thus, the correction of one year was affected by the correction of its subsequent years. The 90% threshold in rules (3) and (4) was used to avoid the over-correction caused by the first image in the time series. The size of the correction window was set to three years in this study. For other regions, the window size could be adjusted according to cloud cover conditions and the availability of seasonal predictor images.

(5) Results and Discussion

The confusion matrix of validation is presented in Tables 3-1 and 3-2. The proposed hybrid method yielded an overall validation accuracy of ~90% for both 2008 and 2016. The results indicate high confidence in identifying water and vegetation. The accuracies for both categories of impervious surface were accurately identified with accuracies varying from 87% to

93%. The accuracies for the bare land were between 75% and 81%, slightly affected by the confusion with high-intensity impervious surface.

Satellite-derived annual maps of impervious surface provided a spatially-explicit understanding of the local urbanization process. Figure 3-12 shows the expansion of impervious surface and habitat changes over the same time period. The value of each pixel is the number of years that the pixel is impervious during the study period and can indicate the year of the development at that pixel. As the development of impervious surface is a unidirectional process, the duration of imperviousness essentially reveals the trajectory of the urbanization process. Our results revealed two interlinked patterns of urbanization in ULM: (i) intensification, the gradually filling of pervious gaps within existing developed areas; and (ii) expansion, the fast encroachment of farmlands and natural areas that are fringing urban centers. The intensification process occurred mainly within stable urban centers or heavily-developed industrial zones. Figure 3-13 shows an example of intensification in northwestern Corpus Christi. The area was an established industrial zone with oil refineries and transportation infrastructure centered around the country's sixth largest port. The continuous development over three decades resulted in more plants, enhanced port facilities and expanded land transportation infrastructures, coupled with the emergence of concentrated residential neighborhoods. In comparison, the expansion process was associated with the loss of farmland and natural vegetation. Figure 3-14 shows an example of expansion in south Corpus Christi, where substantial low-intensity impervious areas bloomed along the Oso Creek indicate the development of large residential communities. For small cities and towns such as Kingsville, Robstown and Ingleside, the urbanization process was slow, and the high-intensity impervious areas were stable. The observed occurrence of parallel urbanization processes confirmed the finding from other metropolitan regions (Li *et al.*, 2015; Schneider and Mertes, 2014; Sexton *et al.*, 2013).

The use of fractional impervious coverage had been proposed to improve the accuracy of quantifying impervious surface. These methods usually estimated the fraction of a pixel as impervious surface by regression or spectral mixing methods. The estimates of fractional impervious coverage could be further grouped into different subcategories to facilitate decision-making processes. However, the performance of these fractional estimates relied on the quality of reference data. Reference data were often generated by on-screen manual digitalization with possible support of some automation procedures. Georeferenced municipal data of streets and residence were converted into submeter binary pixels and then aggregated to satellite pixel level for estimating percent impervious cover, but it was very challenging to obtain these local data in many regions. NLCD data were used as alternative ground truth because it provided a highly accurate delineation of bare land and impervious surface. However, this accuracy was mainly due to the reference data of NLCD including the National Wetland Inventory (NWI) data that were derived from high-standard on-screen digitalization of aerial imagery. For schemes that involved the phenological discrimination of impervious surface, the spatial domain needed to be confined to humid temperate biomes, where rapid vegetation regrowth distinguished intermittently bare soil from persistently bare urban surfaces

The use of satellite thermal infrared data improved the accuracy of impervious surface mapping, mainly due to the unique thermal response of construction materials. In this study, we proposed the use of seasonal maximum brightness temperature to improve the separation of high-intensity impervious surface from bare land. In coastal regions, as the two categories could be highly similar in visible and short-wave infrared regions, classification without using thermal bands led to significant over-estimation of impervious surface alone the shoreline. The use of brightness temperature helped correct misclassified impervious surface into soil and vegetation features (Figure 3-15). The high-intensity impervious surface was warmer than bare land by 1.59 K and 2.79 K in summer and winter, respectively. Such differences were associated with the different specific heat values of construction materials and natural soils, as well as seasonal variations of the surface energy balance. The overpasses of Landsat satellites were approximately 11 AM of the local time, which was close to the peak of surface net radiation. The convenient timing helped to highlight the temperature difference between impervious surface and natural soils.

Furthermore, the proposed temporal filtering approach led to effective improvement of the initial classification results. Our method has several unique characteristics. First, two types of corrections were designed to address different principles of omission and commission errors, respectively. Second, the correction involved two pairs of pervious-impervious categories based on spectral similarity, in contrast to the single impervious category in previous studies. Third, the use of long-term normal status avoided excessive correction and improves the stability of classification results. In this study, the temporal filtering began from the most recent year and moved backwards as this year had the largest impervious area. Spatial enhancement such as “majority filtering” was used in combination with temporal filtering, aimed at reducing the of so-called “salt and pepper” effect. In highly-heterogeneous urban areas, many isolated impervious pixels in classification results were indeed consistent with the real landscape and should not be removed. Without sufficient validation, spatial filtering could result in excessive smoothing of land cover patches and significant distortion of land cover pattern.

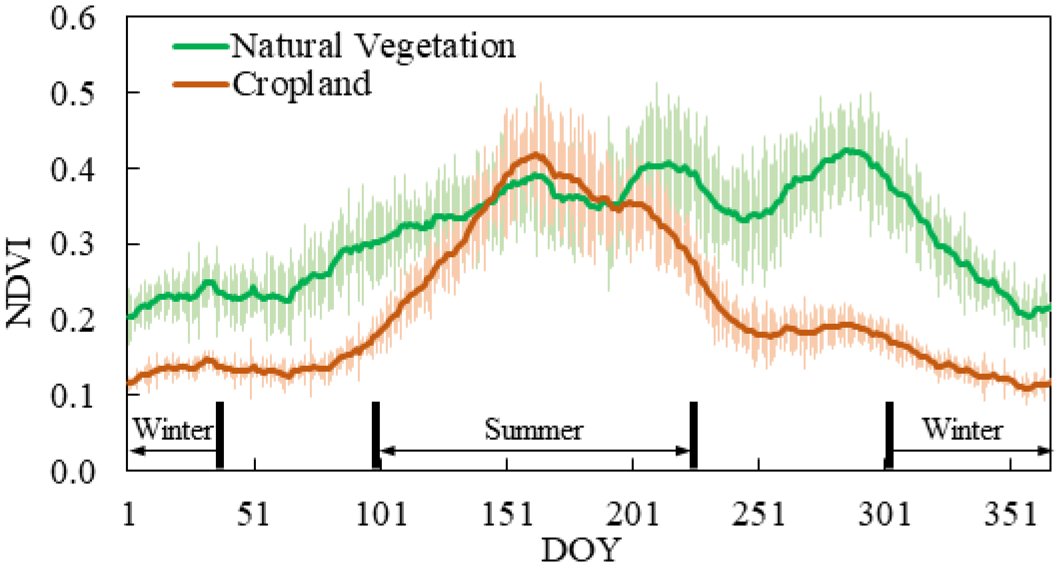

Figure 3-8. Mean NDVI values for natural vegetation and cropland. Data shown are based on the MODIS daily surface reflectance (MOD09GA) between 2007 and 2017 at 20 representative locations. Error bars indicate standard deviations.

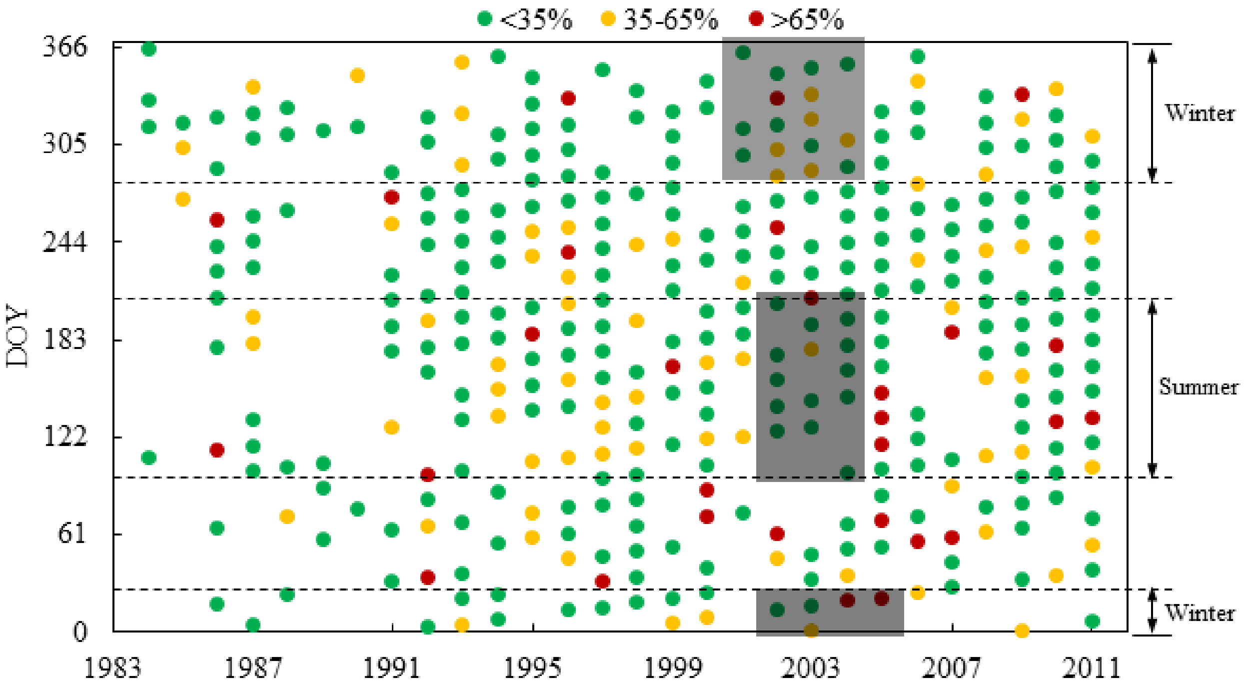

Figure 3-9. Landsat images for each year. Each dot indicates an image and its color indicates the cloud cover condition of this image. Using the year 2003 as an example, the shaded blue area demonstrates the inclusion of three summers and four winters for the classification of a year.

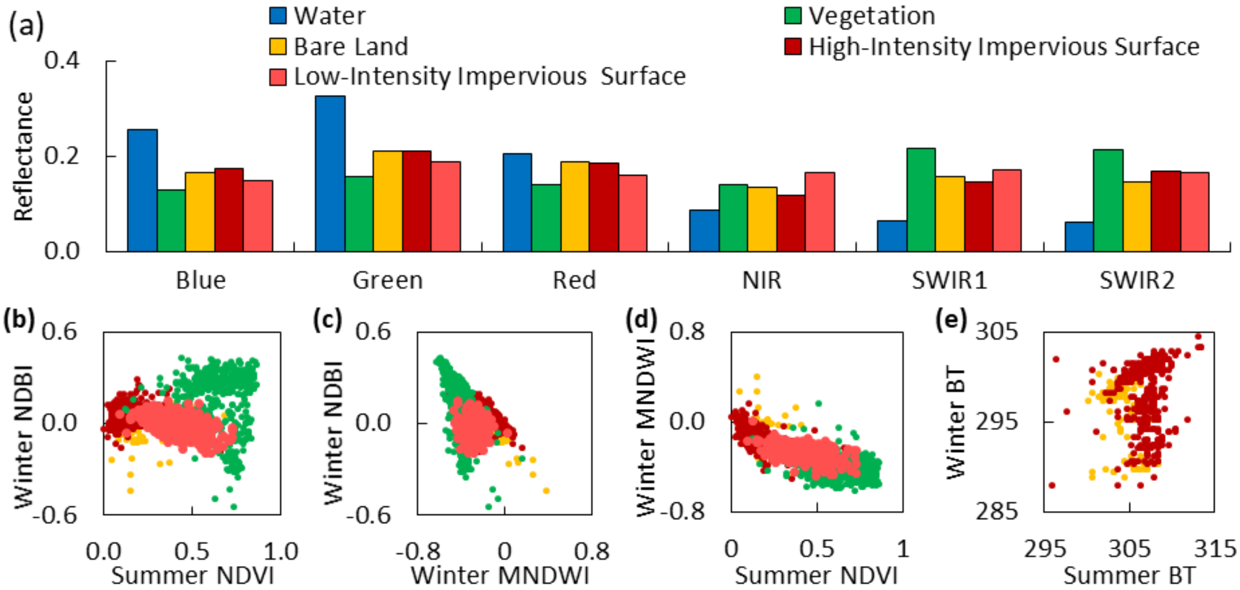

Figure 3-10. Spectral signatures of different land cover categories. Subfigure (a) shows the average surface reflectance of reference data. Subfigures (b)-(d) show the use of seasonal values of multispectral indices to enhance the contrasts between non-vegetated categories and variably-vegetated categories. Subfigure (e) shows the use of brightness temperature (BT) to improve the separation of high-intensity impervious surface from bare land.

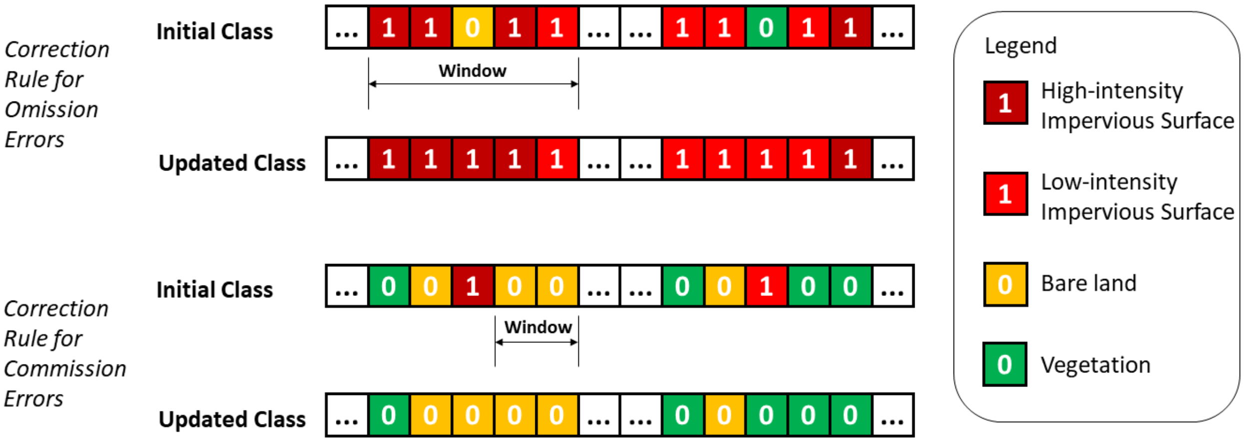

Figure 3-11. Temporal filtering. Each box denotes a year. In the rules for omission errors, years of pervious conditions that occur between consecutive years showing impervious conditions are corrected to be delineated as having impervious conditions. In the rules for commission errors, years showing impervious conditions that occur after consecutive years of pervious conditions are corrected to be delineated as having pervious conditions. Conversion is only allowed either (i) between high-intensity impervious surface and bare land or (ii) between low-intensity impervious surface and vegetation.

Table 3-1. Validation accuracy for the year 2008. VEG, HIS and LIS denote vegetation, high-intensity impervious surface and low-intensity impervious surface, respectively.

	Water	VEG	Bare	HIS	LIS	Use. (%)
Water	45	2	1	1	5	83.33
VEG	1	119	0	1	3	95.97
Bare	3	1	29	3	0	80.56
HIS	0	2	4	91	4	90.10
LIS	0	2	3	5	83	89.25
Pro. (%)	91.84	94.44	78.38	90.10	87.37	89.95

Table 3-2. Validation accuracy for the year 2016.

	Water	VEG	Bare	HIS	LIS	Use. (%)
Water	45	7	0	0	2	83.33
VEG	1	115	3	1	3	93.50
Bare	1	1	27	4	3	75.00
HIS	1	1	2	94	3	93.07
LIS	0	3	2	7	81	87.10
Pro. (%)	93.75	90.55	79.41	88.68	88.04	88.94

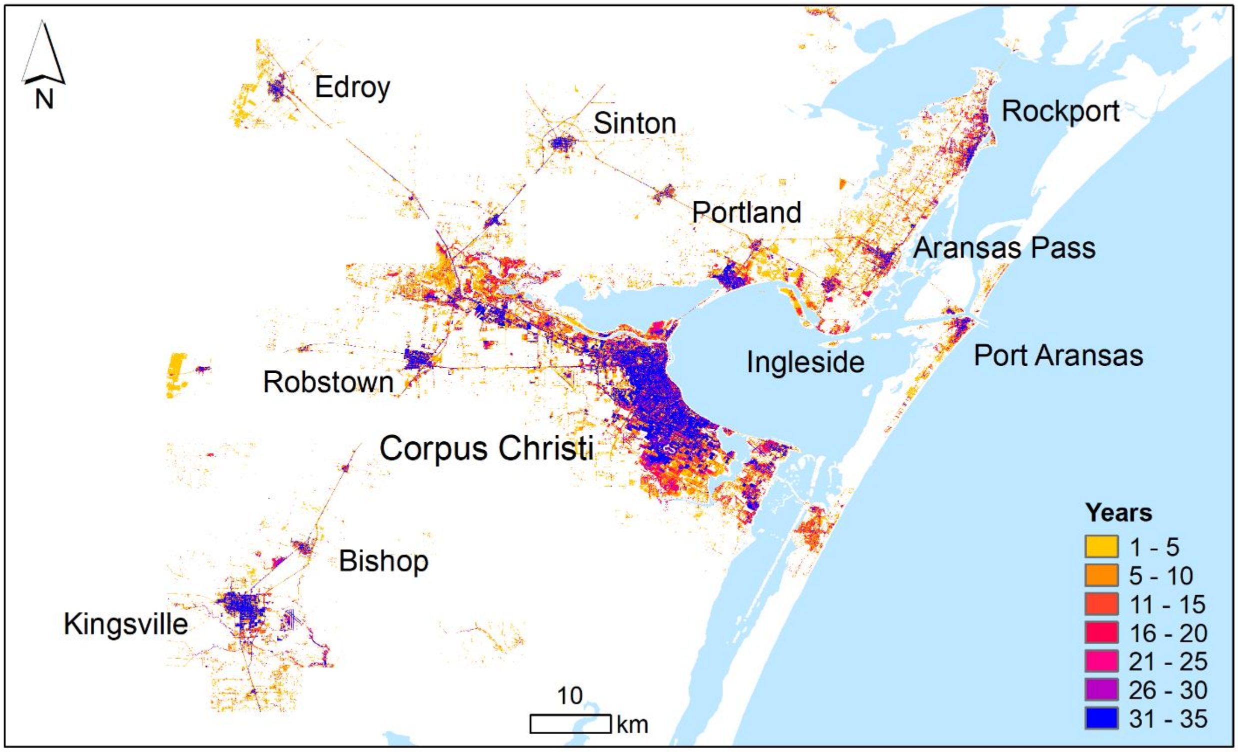

Figure 3-12. The growth of impervious surface in ULM over 30 years.

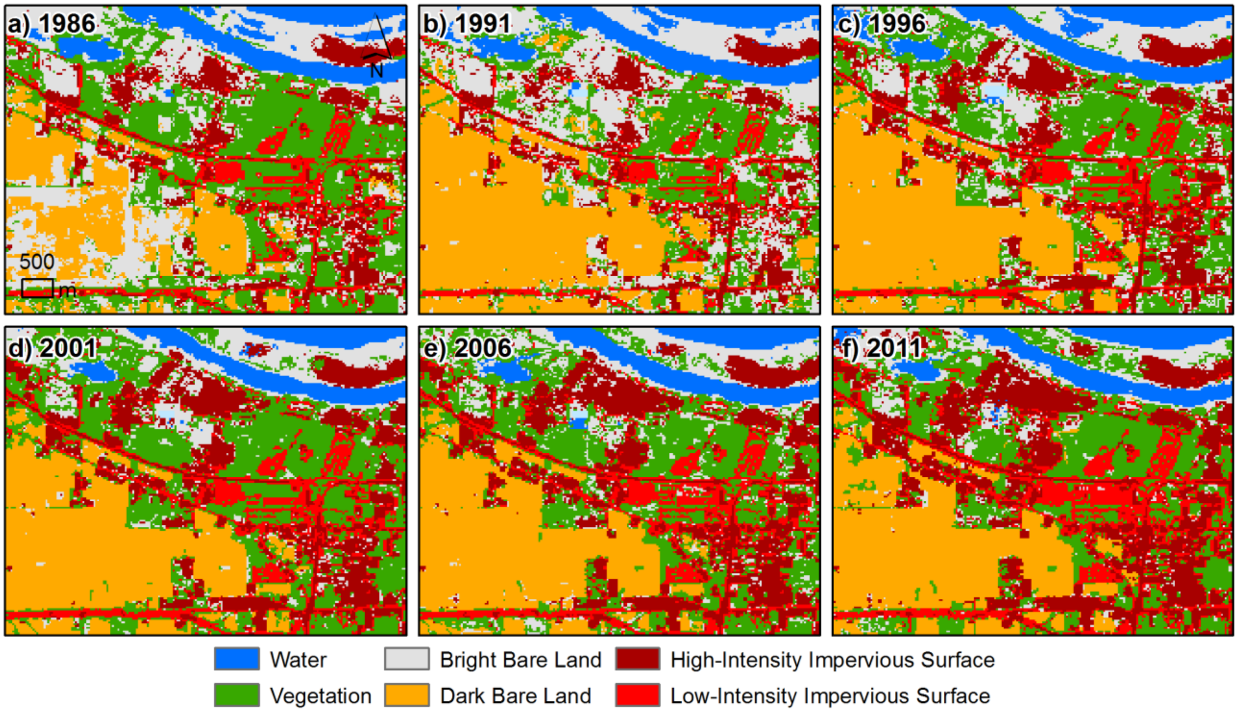

Figure 3-13. Expansion of impervious surface in northwestern Corpus Christi. The land cover change was dominated by the intensification and filling of existing impervious surface in a heavily-developed industrial zone.

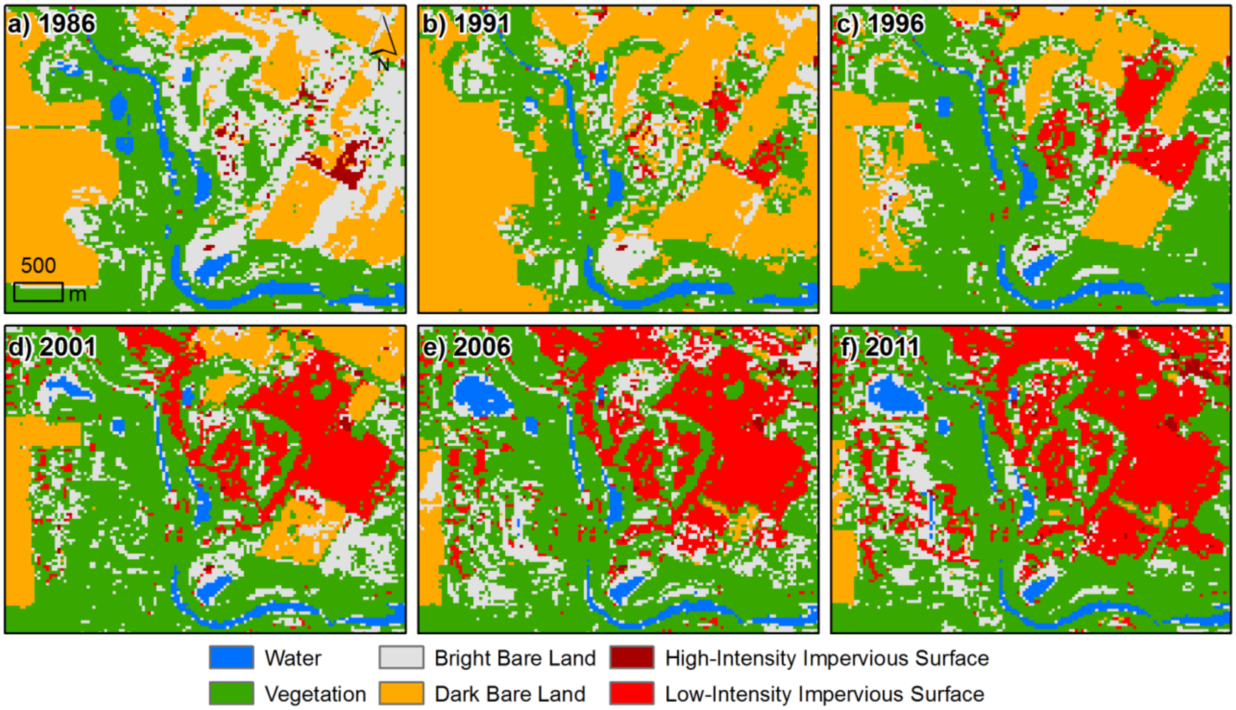

Figure 3-14. Expansion of impervious surface in south Corpus Christi. The dominant land use change was the conversion of agricultural land and natural vegetation into low-density impervious surface.

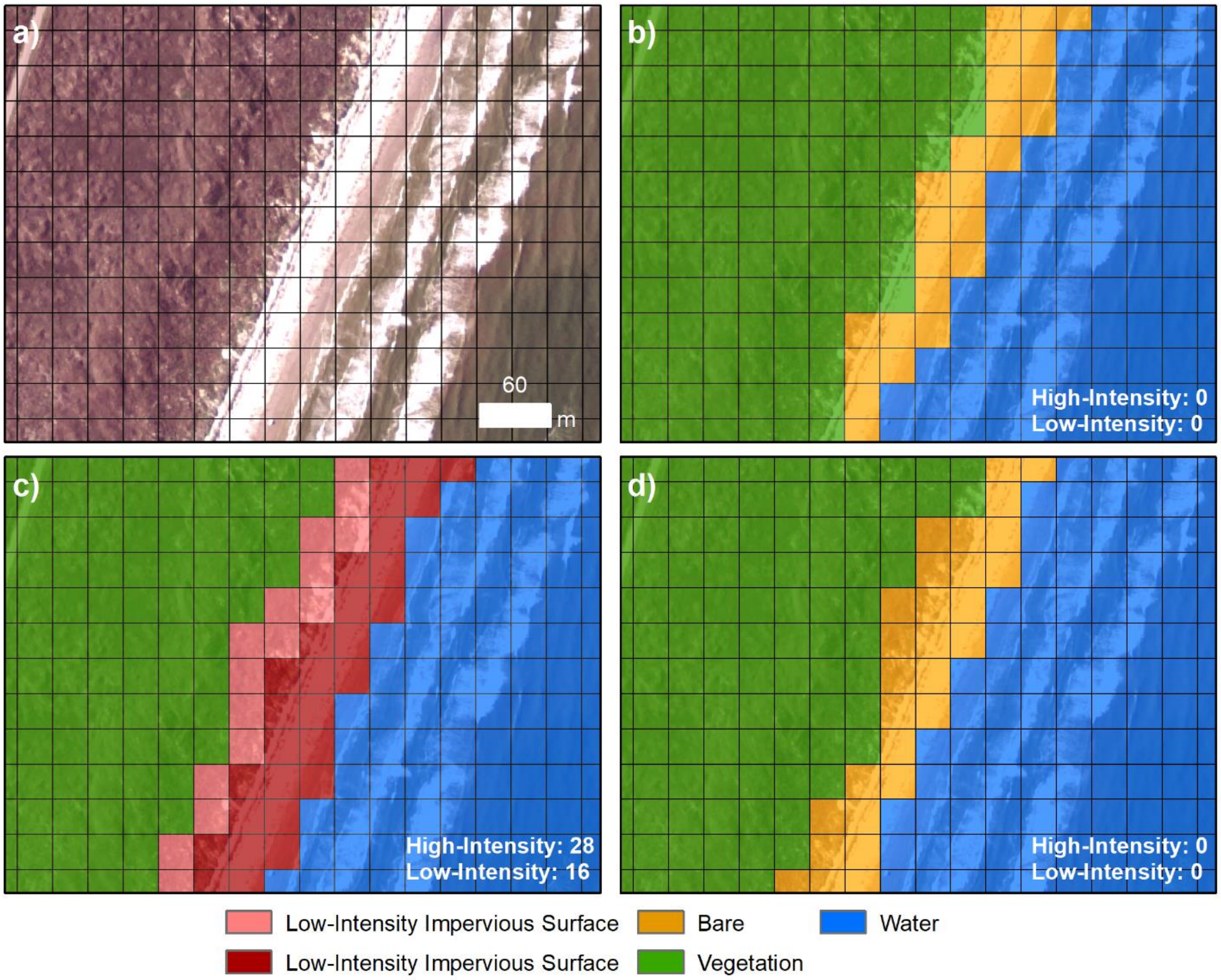

Figure 3-15. The effects of including brightness temperature in classification. The location of this area is shown in Figure 1. Subfigure (a) shows the 1-m NAIP image. Subfigure (b) shows the ground truth generated by on-screen digitalization. Subfigure (c) shows the result based on the conventional classification scheme that does not use brightness temperature. Subfigure (d) shows the result of the proposed method that includes brightness temperature as predictors.

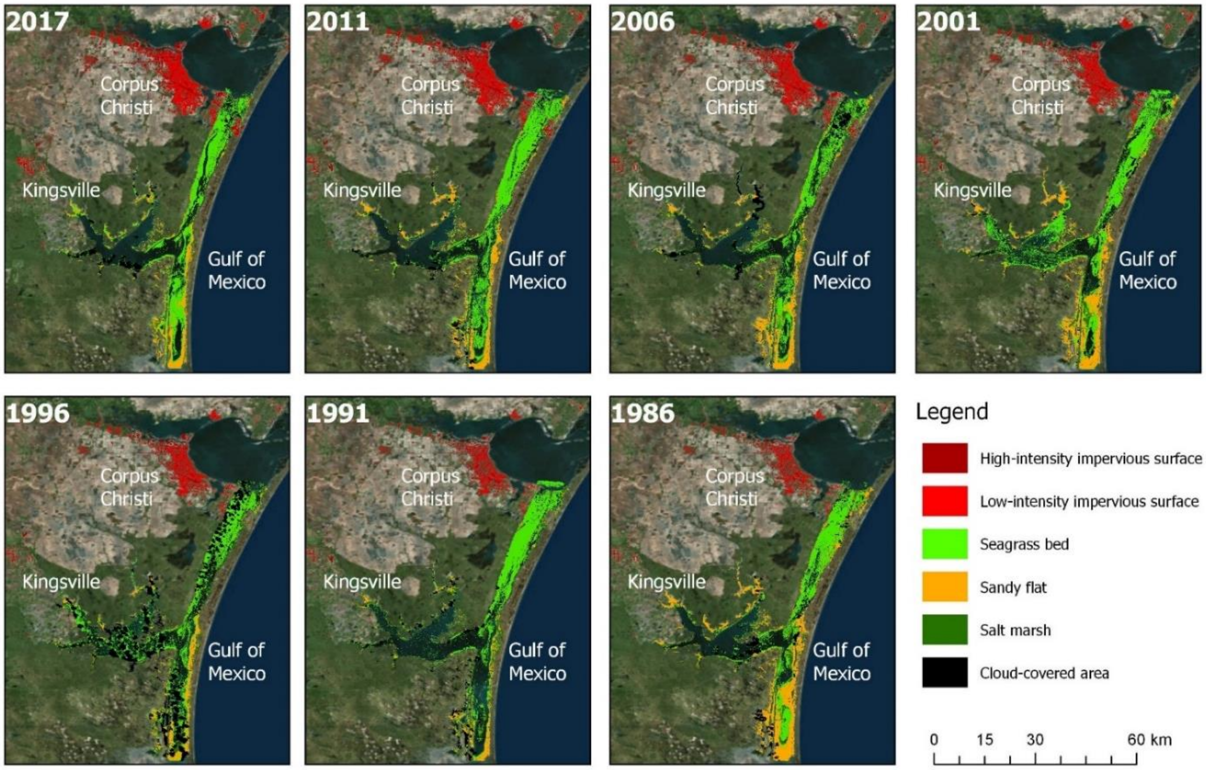

Figure 3-16. Combined changes of coastal impervious surface and habitat in ULM over 30 years.

3.3 Enhancing aerial remote sensing analysis through radiometric correction

We developed a pseudoinvariant near-infrared threshold (PINT) method that can convert the digital numbers of NAIP imagery into surface reflectance based on pseudoinvariant (PIV) pixels identified from Landsat imagery (Figure 3-17). It assumes that a linear relationship exists between digital numbers from a 1 m NAIP image and surface reflectance from a 30 m Landsat image for overlapping areas, if the two images are acquired simultaneously and the atmospheric condition is homogenous within the scene. The Landsat surface reflectance image is considered as a proxy of actual ground-level reflectance measurements for PIV pixels, which follows a strategy that has been used for the correction and validation of satellite images with different resolutions (Hadjimitsis et al., 2009; Padró et al., 2017). Landsat has been used as a reference radiometer against which many other satellite payloads have their performance gauged against. The overall uncertainty of Landsat Tier-1 surface reflectance product is on the order of 6-10% around the world, depending on spectral channel, underlying atmospheric conditions and radiometric calibration characteristics (Vermote et al., 2016; Wulder et al., 2019). The correlation between Landsat and MODIS surface reflectance products is high and the bias is mostly around 1 to 5% with the largest difference in the blue band (Vermote et al., 2016).

The procedure of PINT is centered on the identification of PIV pixels that can best define the linear transformation between surface reflectance and digital numbers, consisting of several steps as shown in Figure 3-18. First, when the targeted NAIP image and the coincident Landsat image are determined, a ten-year Landsat collection of TM and ETM+ images at this location is rigorously filtered. Images with cloud cover >50% in the scene are discarded. For the rest of the collection, pixels detected as clouds or shadows are masked out on each image. In the pixel quality band, the value of a pixel indicates the levels of confidence that a cloud and/or shadow condition exists at this pixel. Pixels with high cloud or shadow confidence are identified and masked out. Then areas within 90 m (i.e., three Landsat pixels) of the edge of the targeted NAIP image are excluded to avoid the influence of boundary pixels. The temporal standard deviation of the near-infrared band at the pixel level is calculated over the ten years of Landsat images. By specifying a percentile of the temporal standard deviation image for thresholding, pixels that have sufficiently low variations are identified as potential PIV pixels. Because the NIR band tends to have greater variations than the visible bands, it is easier and more robust to identify PIV pixels from the NIR band when all bands have the same radiometric resolution. The locations of tentative PIV pixels are aggregated into a mask that is applied to the coincident pair of NAIP and Landsat images. The NAIP image is upscaled to the 30-m spatial resolution of the Landsat reference image in advance with consideration on the homogeneity of the upscaled pixels. For each of the three bands (i.e., red, green and NIR), digital number and surface reflectance are extracted at locations of PIV pixels from the NAIP and Landsat images, respectively, and linear regression is performed after the removal of outliers. The mean value of the coefficient of determination (R^2) of three bands is taken as the measure of regression performance. Through iteratively testing thresholds starting from 0.01st percentile with an increment of 0.01% until the 5th percentile, the threshold with the highest mean R^2 is determined as the best threshold. Given that an NAIP image covers an area of approximately 53 km2 on average or the equivalence of about 60,000 pixels at the 30 m resolution, the increment of 0.01% is equivalent to the addition of 6 pixels, which is considered to be an appropriate scale for common invariant features. The linear transformation models associated with the best threshold are applied to the bands of upscaled 30 m NAIP for validation and eventually the original 1-m NAIP image for high-resolution mapping applications. To validate the performance of PINT, NDVI is calculated using the 30 m NAIP surface reflectance and compared to NDVI generated from Landsat surface reflectance. Evaluation metrics consist of R^2, Nash-Sutcliffe efficiency (NSE), mean absolute error (MAE), and root mean square error (RMSE).

This method is different from previous studies in two aspects. First, the identification of PIV pixels only requires the temporally variation of the NIR band, eliminating the need to inspect the pixels across all bands for the consistency of spectral brightness. The PIV pixels identified in the NIR region are assumed to be spectrally invariant in visible bands as well. The noise components of some multispectral bands may have larger amplitude than the signal components of other bands (Small, 2002). For Landsat TM and ETM+ sensors, the visible bands record less variation and are more affected by residual clouds and snow, in comparison to the infrared bands (Feng et al., 2013). Second, the number of PIV pixels varies based on the optimal threshold of each image, in contrast to the use of a fixed empirical threshold for all images (Padró et al., 2017; Pons et al., 2014). The adaptive scheme of PINT could alleviate the disturbance of nonlinearity of the spectral variance and enhance the spectral diversity of PIV features (i.e., pixels are well spread other than concentrated in a small range of brightness), all amendable to the robustness of the linear regression.

Figures 3-19 and 3-20 show the results of applying this method to ULM at two sites. PIV pixels were identified in marshes and ship channels to construct the linear transformation. No PIV pixels were identified in the tidal flats which had high NIR variations due to the irregularly wind-driven inundation, while marshes were less flooded due to their higher elevation. Raising the percentile threshold resulted in gradually decreasing R^2, but the performance tended to be stabilizing after more than 2% of pixels were used. The corrected NDVI yielded a slightly lower R^2, but RMSE, NSE and MAE were improved significantly. Figures S1 to S4 show additional results of other selected test sites. Figure 3-21 summarizes the best NIR thresholds and the regression lines that defined these thresholds for all test sites. The average threshold was the 0.69th percentile, or 0.025 in terms of the actual value of the temporal standard deviation of the NIR band. This suggests that approximately 300 pixels on average are needed to define the linear relationship between surface reflectance and digital numbers. The 0.01st percentile (five pixels) was identified as the threshold for 35 sites and the 0.02nd percentile (ten pixels) for 23 sites. On the other end, the thresholds were above 4.5 percentile (i.e., > 2,250 pixels) for ten sites. The range of thresholds determined in this study was comparable to the threshold of 0.020-0.027 recommended for MODIS time series (Padró *et al.*, 2017; Pons *et al.*, 2014). Regarding the regression lines, the average slope and intercept were 0.0017 and 0.017 for the NIR band, respectively, and 0.00092 and −0.013 for the red band, respectively. For both bands, slope was positively skewed, while intercept was negatively skewed. Validation results across all test sites show substantial improvement in the NDVI agreement against the Landsat NDVI reference (Figure 3-22). The values of RMSE were reduced from 0.37±0.14 to 0.08±0.07. The values of MAE were reduced from 0.91±0.64 to 0.18±0.52. The values of R^2 were stable: 0.70±0.19 before the correction and 0.71±0.20 after the correction. The values of NSE was reduced from −41.71±107.68 to −0.65±10.39. The negative mean value of NSE reflects the sensitivity of this measure to extreme values.

The calculation of temporal variation of NIR reflectance is a critical component of the PINT method. A key parameter of this procedure is the number of satellite images to be included in the calculation. How many years of images are sufficient for identifying PIV pixels? Will using more images improve the identification of PIV pixels? Thanks to the multidecadal Landsat legacy, we were able to examine the effect of the quantity of Landsat images on the performance of PINT over different durations ranging from two years to 30 years before the acquisition of the NAIP image.

At our study sites, longer durations led to the inclusion of more Landsat images (Figure 3-23). The changes in the number of images appeared to follow a piecewise linear pattern with a reduced slope for durations longer than 12-15 years, suggesting a reduced availability of Landsat images prior to 1999-2001 as Landsat 7 was launched in 1999. Changes in the NIR threshold, however, were less consistent across the sites. The response of correction performance was reflected in the pattern of different measures. The stability of the NIR threshold was not linked to the stability of the measures. The measure of NSE appeared to be more sensitive to the number of images than other measures. Overall, the use of ten years of Landsat images was sufficient for converting digital numbers into surface reflectance and incorporating a longer time series from the same sensor didn’t not substantially improve the correction of NDVI in this study. This duration of Landsat time series was consistent with the value recommended for the identification of PIV features using MODIS time series (Pons *et al.*, 2014) and could be considered as a reasonable configuration for the implementation of PINT for other regions.

The integration of data from multiple sensors on different satellites should enhance the robustness of the identification of NIR threshold and facilitate the comparison of PINT to existing relative correction approaches. However, the spectral differences among the sensors of interest should be taken into consideration. For example, incorporating additional images from the Landsat 8 Operational Land Imager (OLI) sensor could considerably increase the temporal resolution of time series, but the OLI bands are spectrally narrower than the corresponding TM and ETM+ bands, especially in the near-infrared region, which could result in NDVI differences of about 5% (Flood, 2014; Zhu *et al.*, 2016). Incorporating images from the Sentinel-2A Multispectral Instrument (MSI) sensor is expected have the same problem, as MSI and OLI bands are very spectrally similar except in the thermal infrared region.

The development and validation of PINT in this study was particularly facilitated by the use of Google Earth Engine. Traditionally, NAIP images are downloaded as county-scale mosaics through the Agriculture Farm Service of the United States Department of Agriculture (USDA). Only the data of the most recent year are available on an ArcGIS server. The collection of NAIP data for a large region or a long period is often a very time-consuming procedure. Through hosting the entire NAIP legacy in cloud storage, Google Earth Engine provides a highly-efficient means to improve not only the accessibility of this unique dataset, but also its processing and analysis. The free and open access of NAIP data through Google Earth Engine could result in landmark changes in the utilization of NAIP data and its integration with other remotely sensed data, an information breakthrough comparable to the initiation of Landsat data release in 2008. Also, through Google Earth Engine, the proposed method takes advantage of the archives of Landsat 5 and 7 and identifies PIV features based on hundreds of images that fully address the temporally spectral variation of ground features. This eliminates the previous efforts to calibrate to specific laboratory or field spectra, because the 30-m PIV pixels are stable combinations of a variety of materials instead of the pure presence of a single material.

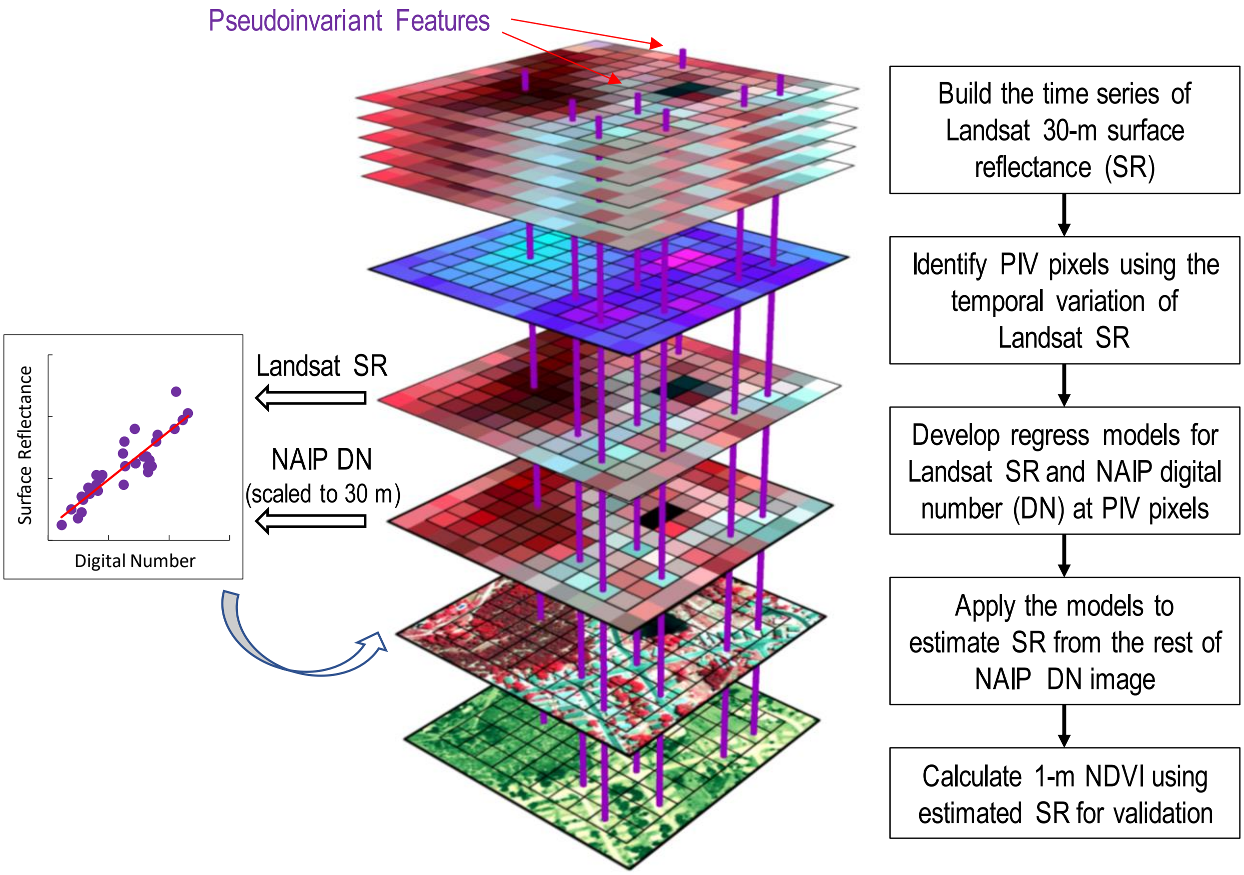

Figure 3-17. The conceptual diagram of the pseudoinvariant near-infrared threshold (PINT) method. DN and SR stand for digital number and surface reflectance, respectively.

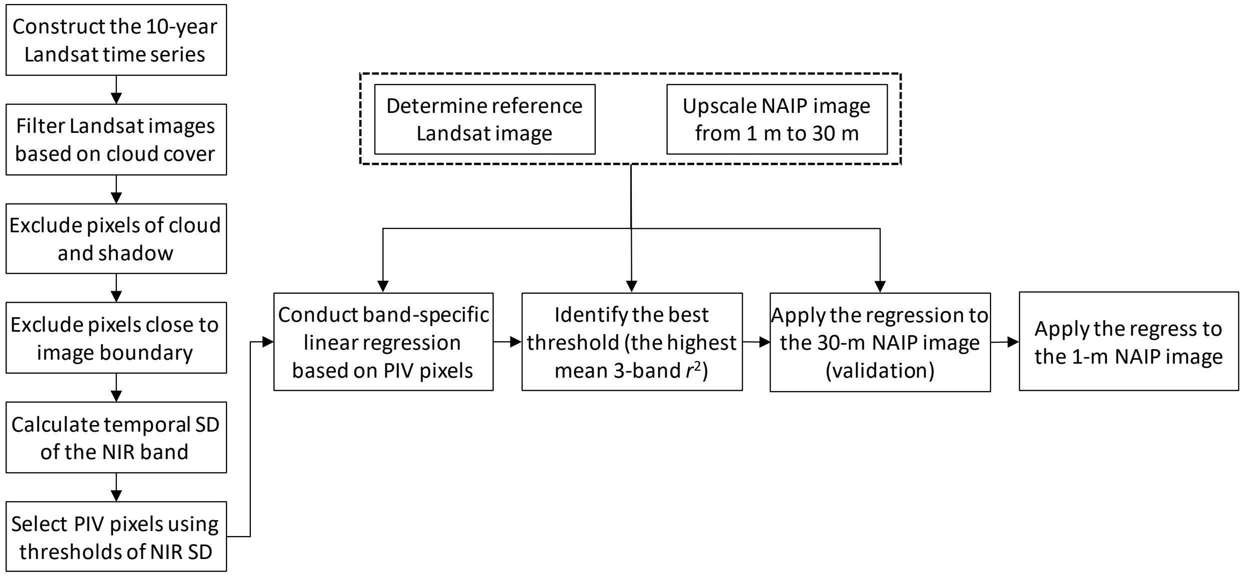

Figure 3-18. The flowchart of the proposed PINT method.

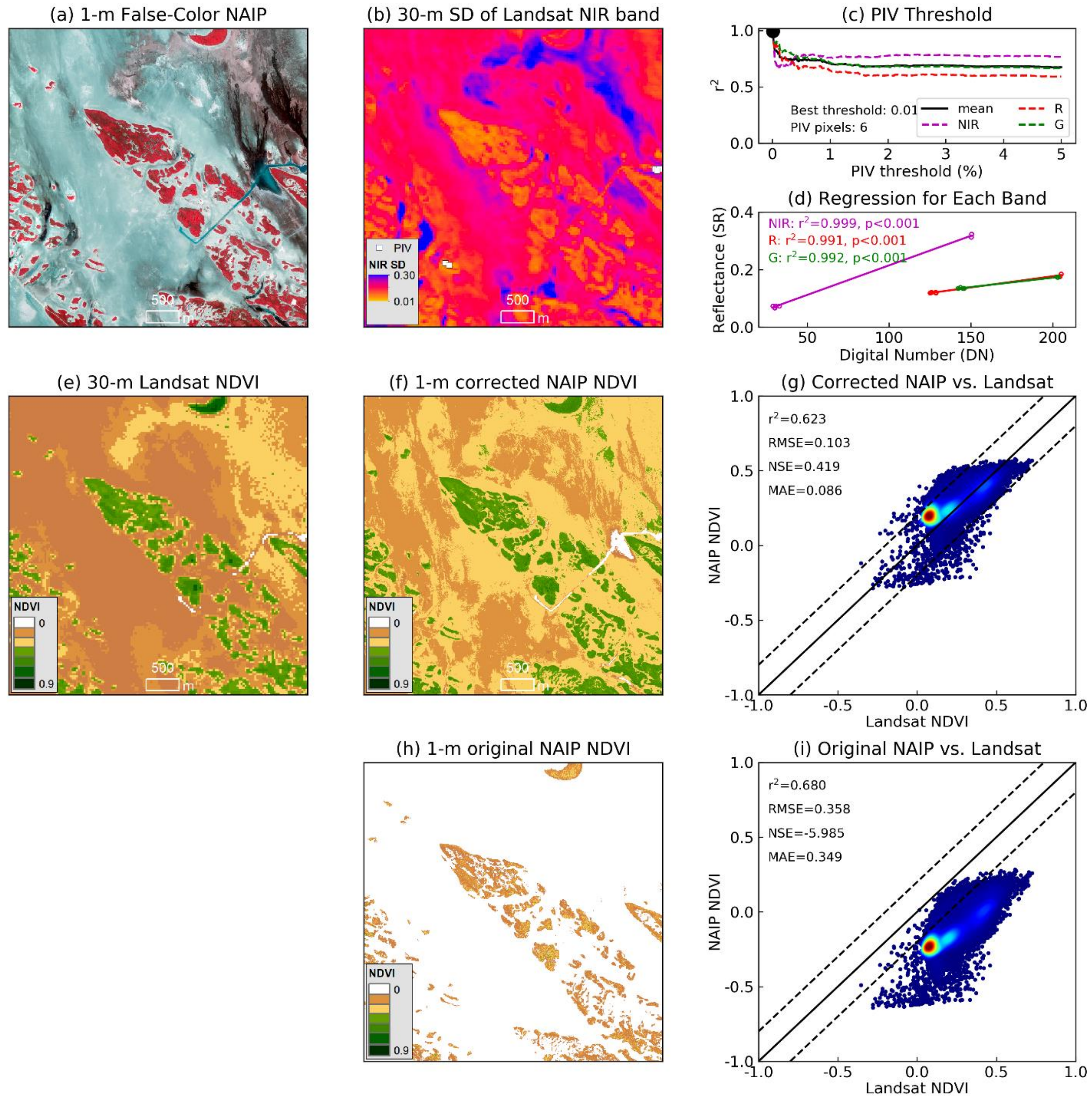

Figure 3-19. Application of PINT at Site 4 in Upper Laguna Madre. Plots (a) – (d) demonstrate the identification of PIV pixels: plot (a) shows the 1-m false-color NAIP image (NIR, red and green bands) before radiometric correction; plot (b) shows pseudoinvariant features (white squares) identified from the 10-year NIR standard deviation of Landsat TM and ETM+ images; plot (c) demonstrates the identification of the best threshold (0.01st percentile); plot (d) shows the linear regressions of Landsat surface reflectance and NAIP digital numbers based on pseudoinvariant pixels. Plots (e) – (i) show the validation of NDVI values: plot (e) shows 30-m Landsat NDVI as the reference; plots (f) and (h) show 1-m NAIP NDVI before and after correction, respectively; plots (g) and (i) show the agreement with Landsat reference before and after correction, respectively. The solid line is the 1:1 line, indicating a perfect match between NAIP and Landsat NDVI values, and the dashed lines represent the upper and lower 10% error bounds.

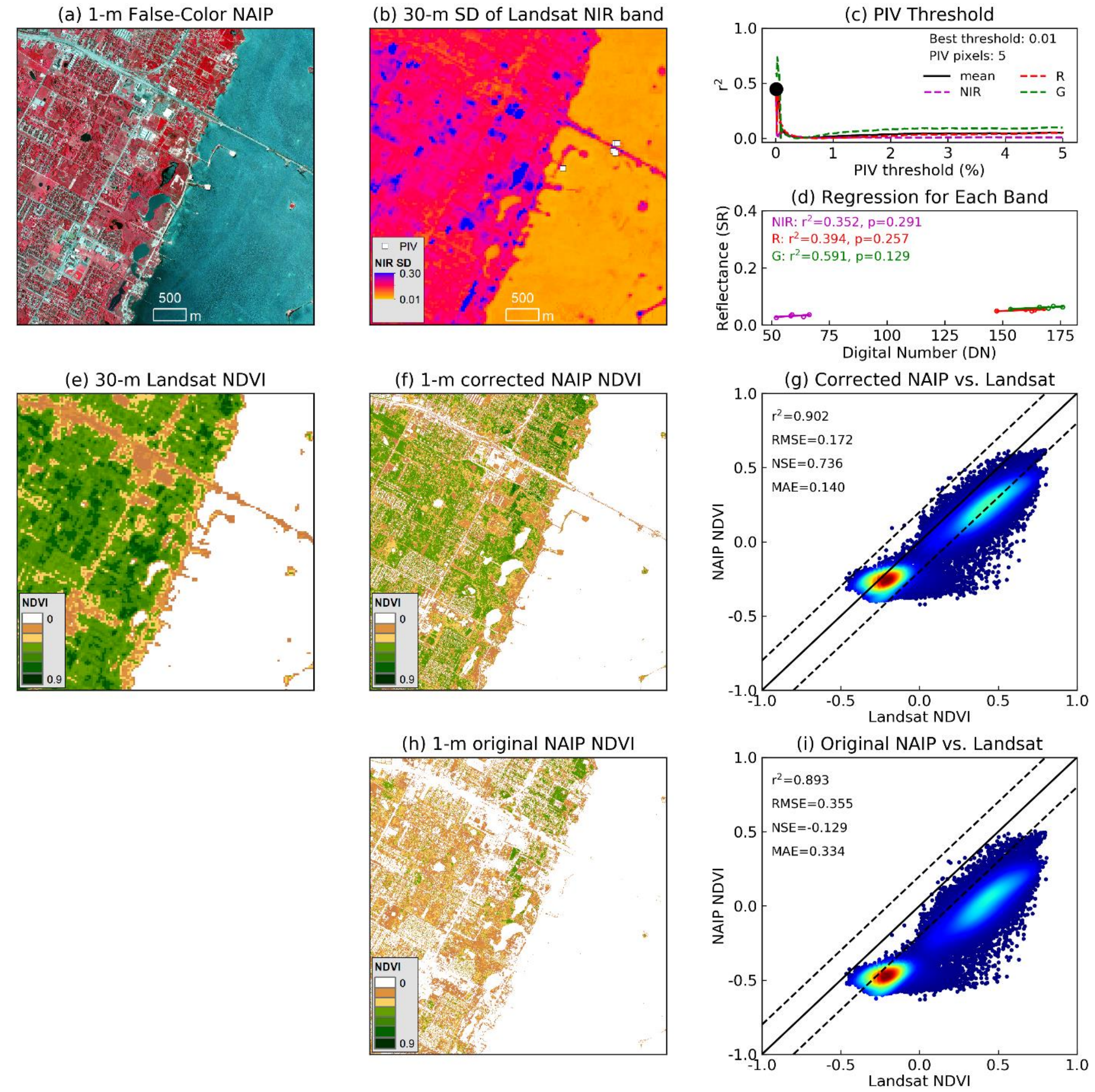

Figure 3-20. Application of PINT at Site 4 in Upper Laguna Madre. Plots (a) – (d) demonstrate the identification of PIV pixels: plot (a) shows the 1-m false-color NAIP image (NIR, red and green bands) before radiometric correction; plot (b) shows pseudoinvariant features (white squares) identified from the 10-year NIR standard deviation of Landsat TM and ETM+ images; plot (c) demonstrates the identification of the best threshold (0.01st percentile); plot (d) shows the linear regressions of Landsat surface reflectance and NAIP digital numbers based on pseudoinvariant pixels. Plots (e) – (i) show the validation of NDVI values: plot (e) shows 30-m Landsat NDVI as the reference; plots (f) and (h) show 1-m NAIP NDVI before and after correction, respectively; plots (g) and (i) show the agreement with Landsat reference before and after correction, respectively. The solid line is the 1:1 line, indicating a perfect match between NAIP and Landsat NDVI values, and the dashed lines represent the upper and lower 10% error bounds.

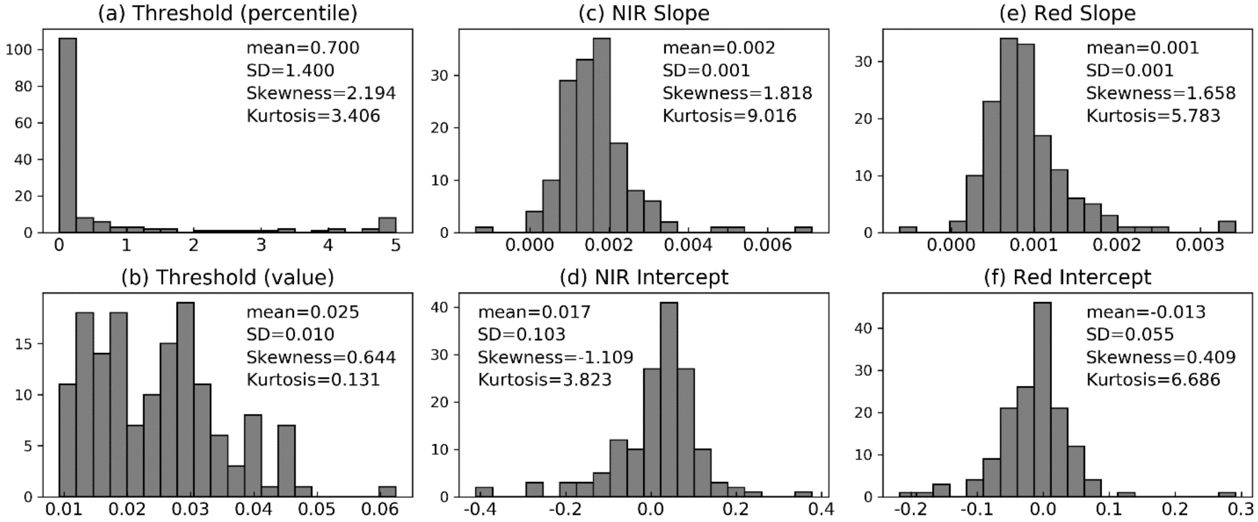

Figure 3-21. Summary of PIV identification across all validation sites.

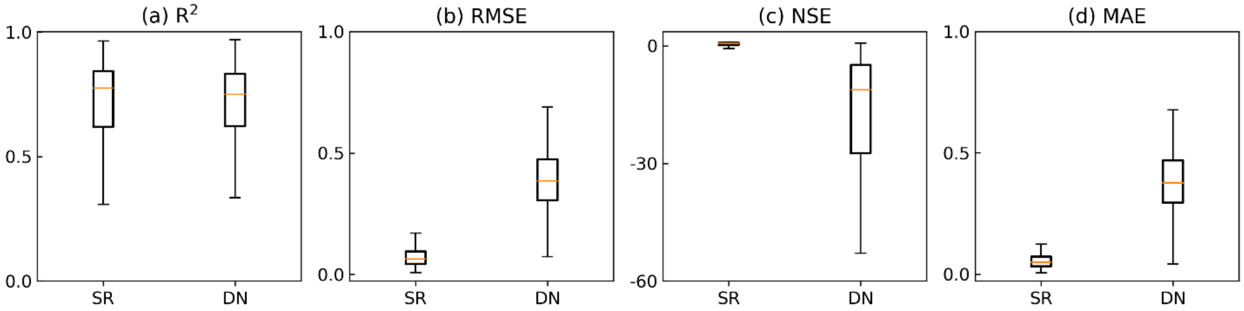

Figure 3-22. Summary of performance metrics across all validation sites.

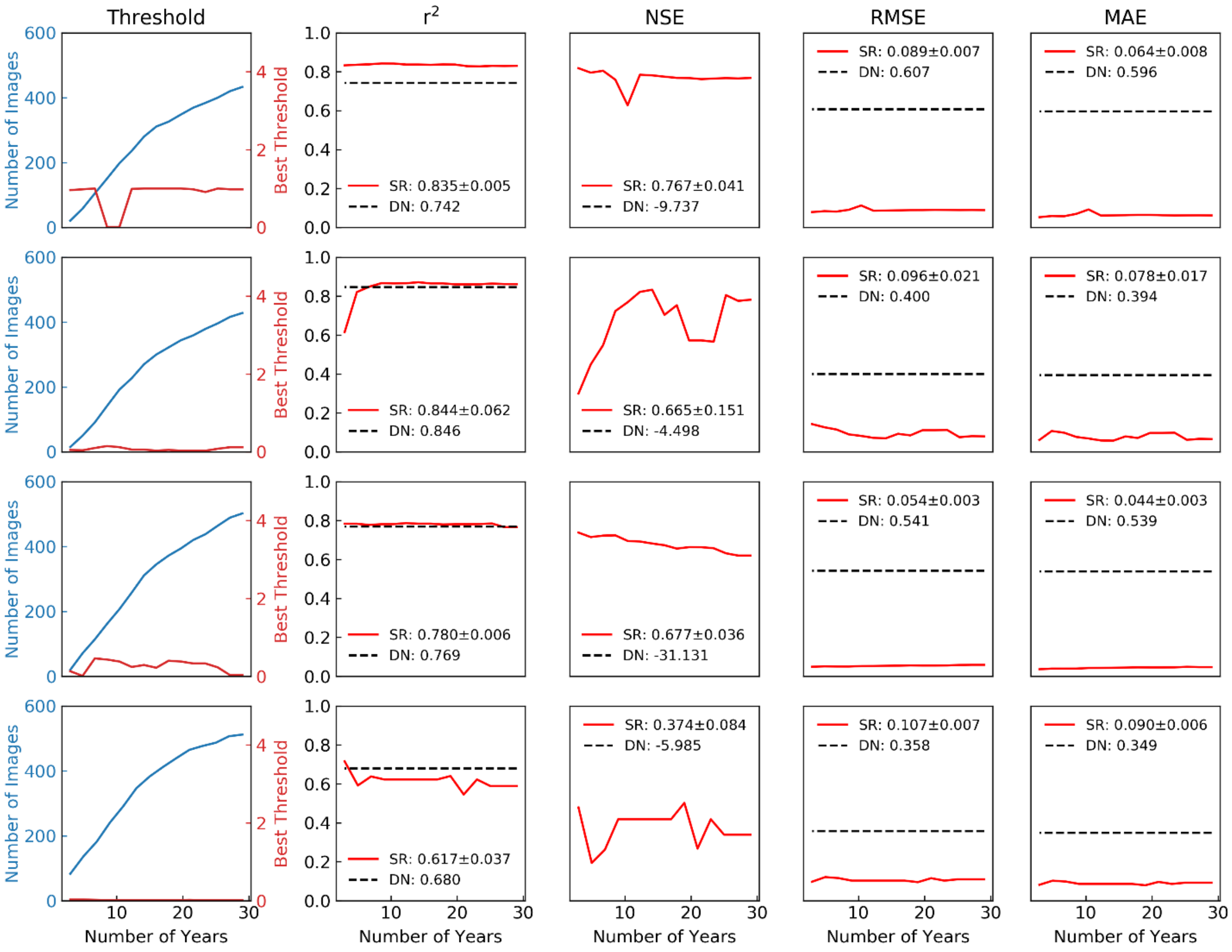

Figure 3-23. Effect of the length of Landsat time series on the identification of NIR thresholds and the quality of the NDVI correction.

4. Development of Urbanization Stress Forecasting Models

Two models were developed to analyze the stresses caused by urbanization processes on estuarine health: (1) a nonlinear autoregressive network ensemble with exogenous inputs (NRAX); (2) an integrated Markov-Chain Cellular-Automata (MCCA) model.

4.1 NRAX model

A nonlinear autoregressive network model with exogenous inputs (NRAX) was developed to analyze the impacts of urbanization on estuarine water quality changes at the seasonal scale from 1985 to 2017 (Figure 4-1). The artificial neural networks developed in this project were multilayer perceptron (MLP) networks that were widely used for classification or regression (Maier *et al.*, 2010; Wu *et al.*, 2014). A major advantage of MLPs is that given sufficient hidden units and training data, they are able to learn an input-output relationship of arbitrary complicity (Shu and Burn, 2004). An MLP consisted of an input layer, a hidden layer and an output layer. The model used two types of inputs over a six-month antecedent period: i) seasonal time series of external forcing, consisting of seasonal evaporation, precipitation, land cover change, and population change (Figure 4-2); and ii) seasonal time series of water quality variables, including salinity, dissolved oxygen, temperature and turbidity (Figure 4-3). The optimal number of neurons in the hidden layer was determined by iteratively comparing the performance of different configurations with different number of hidden units (from 5 to 50). The output layer had only one neuron that represented the targeted environmental quality parameter. Input values were fed to neurons in the input layer and sent to hidden neurons through connections associated with weights. The hidden neurons summed the inputs and applied them through a transfer function that controls the amplitude of the hidden neuron's output (Wan *et al.*, 2015). The output from the hidden layer was then sent to the output layer via connections with another set of weights. The final output was generated by the output neuron using a transfer function. The hyperbolic tangent sigmoid transfer function (Vogl *et al.*, 1988) was used for both hidden and output layers in order to confine the outputs within the range [−1,1]:

$$y = \frac{2}{1+e^{-2x}} - 1 \tag{1}$$

The constructed networks were trained using the Levenberg-Marquardt backpropagation algorithm (Hagan and Menhaj, 1994). This algorithm is a second-order gradient optimization method and is faster and more reliable than other backpropagation algorithms (Jeong and Kim, 2005) and is considered the best method in many ANN studies (Imen *et al.*, 2015; Maier *et al.*, 2010). For the learning parameters of the backpropagation algorithm, the maximum number of training epochs was 300, the minimum performance gradient was 1×10^{-6}, the maximum number of validation failures was 6, and the initial μ, μ decrease factor and μ increase factor were 0.001, 0.1 and 10, respectively. The training of a network stopped when the maximum number of validation failures or epochs was reached, the performance was minimized to the goal, or the performance gradient fell below the threshold. The performance of network calibration was evaluated using the mean squared error function without transformation.

The established MLPs were combined into ensembles to achieve better prediction accuracy, as network ensembles have shown to improve the generalization capability of ANN models. Network ensembles are known to improve the generalization capability of ANN models (Cannon and Whitfield, 2002; Cianfrani *et al.*, 2015; Jeong and Kim, 2005; Shu and Burn, 2004). Linear combination is a commonly used method for combining networks. An ensemble can be created from a set of networks via simple averaging or a weighted average that consider the relative performance of each network (Shu and Burn, 2004). In this study, for each implementation with specified inputs and structure, a total of 500 networks are constructed and trained. The networks are ranked by the overall performance that includes network training, validation and test stages. Networks with top predictive performance are selected as ensemble members, and the ensemble output is the average of outputs from all members. The performance of ANN ensembles is compared to multiple linear regression (MLR) models using the coefficient of determination (R^2), the root-mean-square error (RMSE) and the relative root-mean-square-error (RRE). The R^2 measures the percent of variation of the observed abundance being explained by the modeled abundance. The RMSE and RRE measure the deviation of the modeled abundance from the observed abundance. These performance indicators are widely used in hydrological and environmental modeling studies (Alcázar *et al.*, 2008; Maier *et al.*, 2010; Melesse *et al.*, 2011; Qiu and Wan, 2013; Wan *et al.*, 2015; Wu *et al.*, 2014):

$$R^2 = \left[\frac{\sum_{i=1}^{n} (O_i - \overline{O})(S_i - \overline{S})}{\sum_{i=1}^{n} (O_i - \overline{O})^2 \sum_{i=1}^{n} (S_i - \overline{S})^2} \right] \tag{2}$$

$$RMSE = \sqrt{\frac{\sum_{i=1}^{n} (O_i - S_i)^2}{n}} \tag{3}$$

where n is the number of data points (years) during the period of evaluation, O_i is the observed water quality condition, $\overline{O}$ is the mean of the observed water quality condition, S_i is the simulated water quality condition, and $\overline{S}$ is the mean of the simulated water quality condition.

The 33-year data of the Upper Laguna Madre was divided into ensemble training dataset (85%) and validation dataset (15%). The training dataset was further randomly divided into network training subset (80%), validation dataset (10%), and test dataset (10%). The training and validation performance for seasonal water quality of the Upper Laguna Madre is shown in Figures 4-4 to 4-7. The NRAX ensemble approach yielded good estimations for all targeted variables, particularly for dissolved oxygen and water temperature with validation R^2 above 0.8. Even for the estimation of turbidity that had significant monthly variation, the ensemble achieved a validation R^2 over 0.5. The strong generalization ability of the ensembles is mainly due to two reasons. First, the ensembles can capture nonlinear impact-consequence relationships of complex systems. The interactions among neurons across different layers are able to assemble the interlinked hydrological, geochemical, and biological processes at the interface of riverine and estuarine systems, which has been demonstrated in a number of coastal studies. Second, the inclusion of evaporation and precipitation at the bay surface improves the quantification of estuarine freshwater budget, leading to an improved consideration of the accumulating effects of freshwater fluxes on estuarine water quality changes. The NRAX model developed in this project could benefit decision makers and researchers in other coastal regions along and beyond the Texas Coast.

Freshwater fluxes interact with an estuary ecosystem primarily through affecting the salinity gradient that is the main factor controlling the estuarine community and population structure (Montagna *et al.*, 2011). Many studies demonstrated the importance of evaporation and precipitation to estuarine salinity. Analytical data from biogeochemical studies in coastal regions have shown a strong control relationship between evaporation and chloride and sodium concentrations (Barrie *et al.*, 2015; Mohan and Walther, 2015). In dry seasons or shallow, flow-restricted parts of the estuary, the concentrating effect of evaporation and the diluting effect of precipitation on salinity are even more significant (Montagna *et al.*, 2002; Sumner and Belaineh, 2005). The effect of evaporation can be exacerbated under extended drought conditions in semi-arid regions where high evaporation and hypersaline groundwater discharge occur simultaneously (Bighash and Murgulet, 2015). This indicates a confounded picture of estuarine hydrological conditions, dependent on the competing effects of vertical freshwater fluxes and their interaction with lateral riverine inflows. Such an understanding challenges the widely-accepted dogma that freshwater inflows control estuary salinity gradients. Freshwater inflow has little effect on the salinity at the annual scale in large, shallow estuaries, such as in Florida Bay (Nuttle *et al.*, 2000), the Upper Gulf of California (Lavin *et al.*, 1998) and several estuaries in Northern Australia (Ridd and Stieglitz, 2002), where freshwater inflow was substantially less than the direct rainfall onto the bay and significant evaporation occurred in the bay. Lowered salinity values ultimately are due to freshwater dilution, but they do not exhibit a clear association with freshwater inflow due to the effects of evaporation and other factors (Montagna *et al.*, 2011). Overall, annual evaporation in ULM is 141% higher than the total of annual precipitation and inflows, indicating a negative freshwater budget over the long term. Compared to the great intra-annual variations of freshwater inflows, evaporation and precipitation are more temporally stable and spatially uniform, constituting a relatively stable component of estuarine freshwater budget and thus a more predictable control on the estuarine salinity gradient.

Unfortunately, evaporation and precipitation are rarely included in the analytic analysis of freshwater-fishery relationships. An important reason might be the lack of long-term adequate measurements and analyses. This is particularly so for evaporation. For example, along the 560-km Texas coastline, there are only four pan evaporation stations located near estuaries available for estimating the evaporation from open water in estuarine environments. Large-aperture scintillometer and eddy covariance towers have been used for estimating evapotranspiration in inland areas, but their applications for measuring evaporation from open water are still limited (McJannet *et al.*, 2011). There is also significant uncertainty in estimating regional precipitation based on isolated rain gauges at ground stations. In contrast, the measurement of inflow requires only a stream gauge and long-time observations have been achieved for many estuaries. From the modeling perspective, the lack of evaporation process has been considered as one of the critical shortcomings in coastal hydrodynamic modeling (Li and Hodges, 2015). Our results indicate the advantage of including evaporation data to estimate water quality. First, ANN ensembles have a strong ability to analyze nonlinear behaviors of complex environmental systems. The interactions among neurons across different layers is able to capture the interlinked hydrological, geochemical and biological processes at the interface of riverine and estuarine systems, as has been demonstrated in several coastal studies (Cianfrani *et al.*, 2015; Froeschke *et al.*, 2013; Muñoz-Mas *et al.*, 2014). Second, the inclusion of evaporation and precipitation at the bay surface leads to a more thorough analysis of the estuarine freshwater budget and benefits the quantification of the accumulative effects of freshwater fluxes on estuarine water quality. This suggest that the proposed ANN ensemble approach has the potential to improve the reliability of the TxEMP-based estuarine freshwater management strategies. Improved models that more accurately identify water needs to sustain coastal ecosystems is critical to best meet environmental, potable water, and industrial needs in regions where water is limited (Hill *et al.*, 2011).

In addition to its continued, critical role in freshwater policies of Texas, the TxEMP model has been extensively analyzed over the world and considered as an important example of operational flow criteria (Gillson, 2011; Ji and Chang, 2005; Robins *et al.*, 2005; Sun *et al.*, 2015; Yáñez-Arancibia and Day, 2004). The effectiveness of this type of models largely rely on the quality of the characterized freshwater-species relationship and have profound implications on environmental management and ecosystem resilience in many estuarine systems. The proposed ANN ensemble method could improve the TxEMP model and support estuarine management. From a technical perspective, ANN ensembles has a strong predictive ability for nonlinear systems and can enhance the overall reliability and applicability of TxEMP-based management frameworks. It represents a growing interdisciplinary integration between biology and information science to take advantage of the breakthroughs in machine learning. From the operational perspective, the implementation of ANN ensembles is highly efficient at a very low cost, compared to the resource demand of physically-based process models. From a perspective of knowledge translation, the concept of ANN is well-accepted and easy to understand, making it friendly to a wide range of decision makers and stakeholders. Therefore, the ANN ensemble approach developed in this study could benefit decision makers and researchers beyond the context of the Gulf Coast. As with other modeling approaches, ANN models are reliable only under the range of conditions that are included in the training set. The established input-output linkages cannot be assumed valid in extrapolation for future scenarios that are beyond the range of the training set.

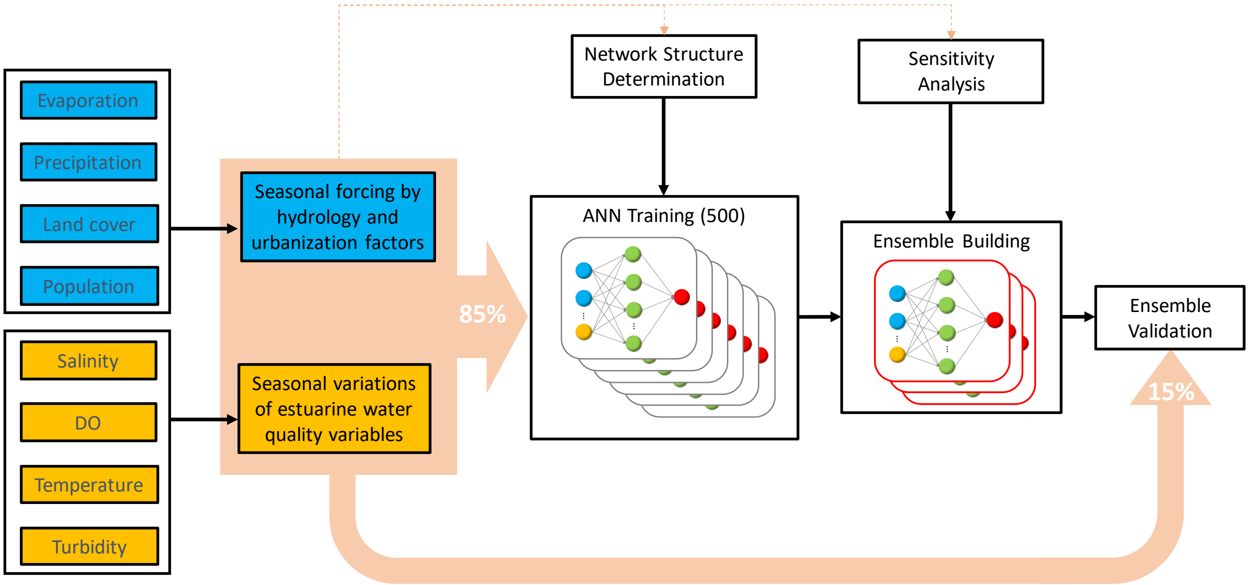

Figure 4-1. The framework of ensemble forecasting for estuarine water quality.

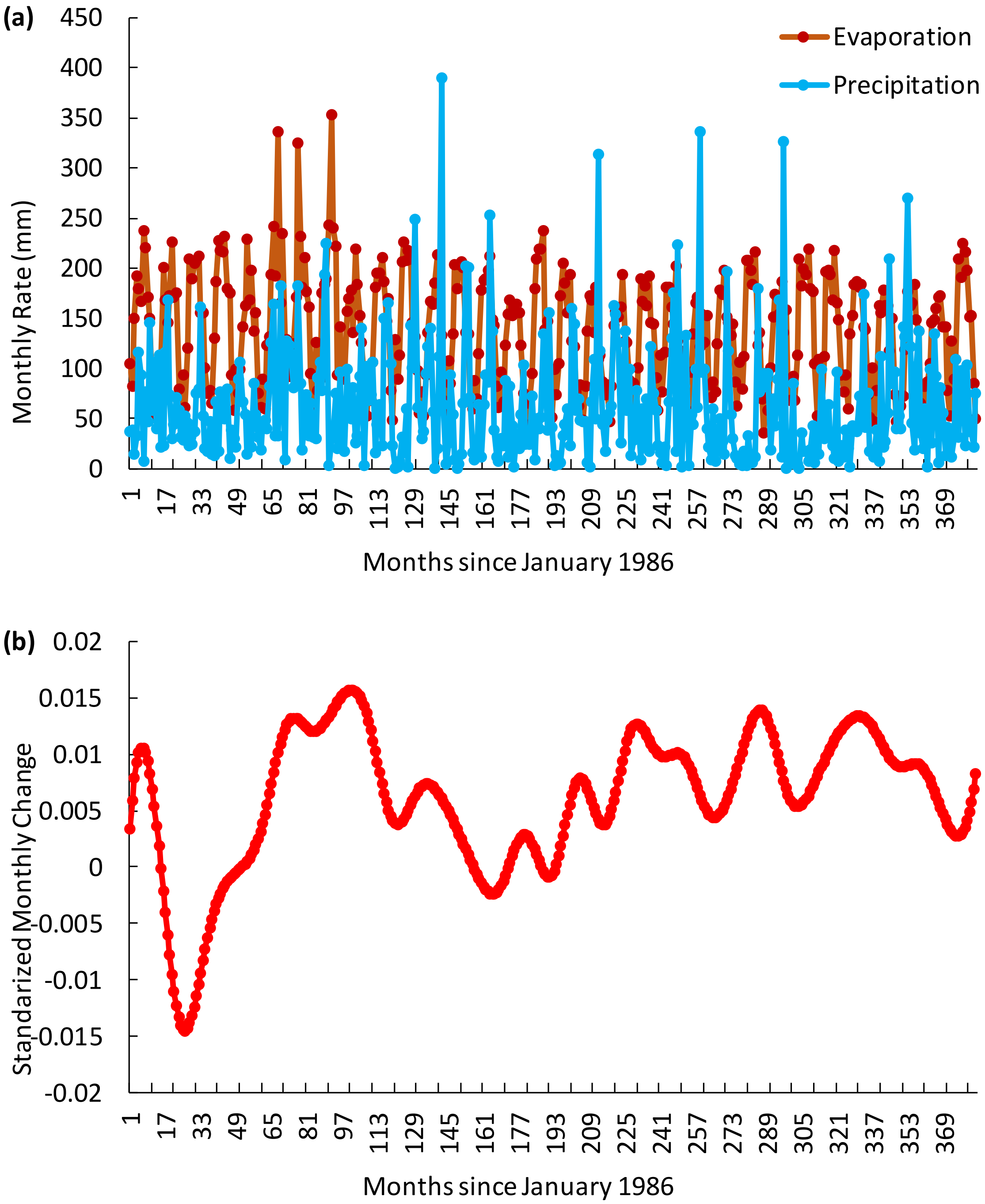

Figure 4-2. Monthly conditions of (a) evaporation and precipitation rates and (b) standardized urbanization rate.

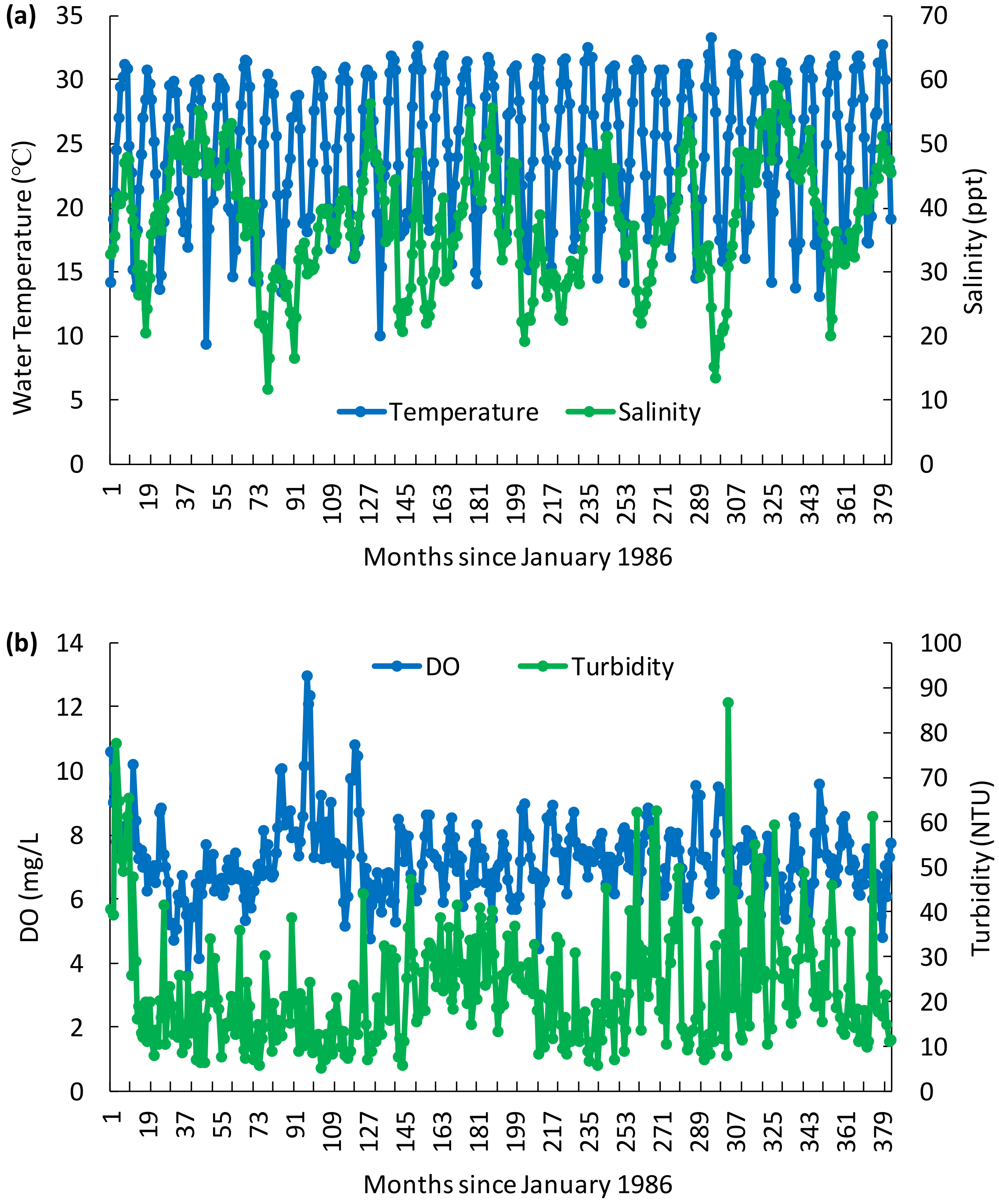

Figure 4-3. Monthly conditions of (a) water temperature and salinity and (b) dissolved oxygen and turbidity.

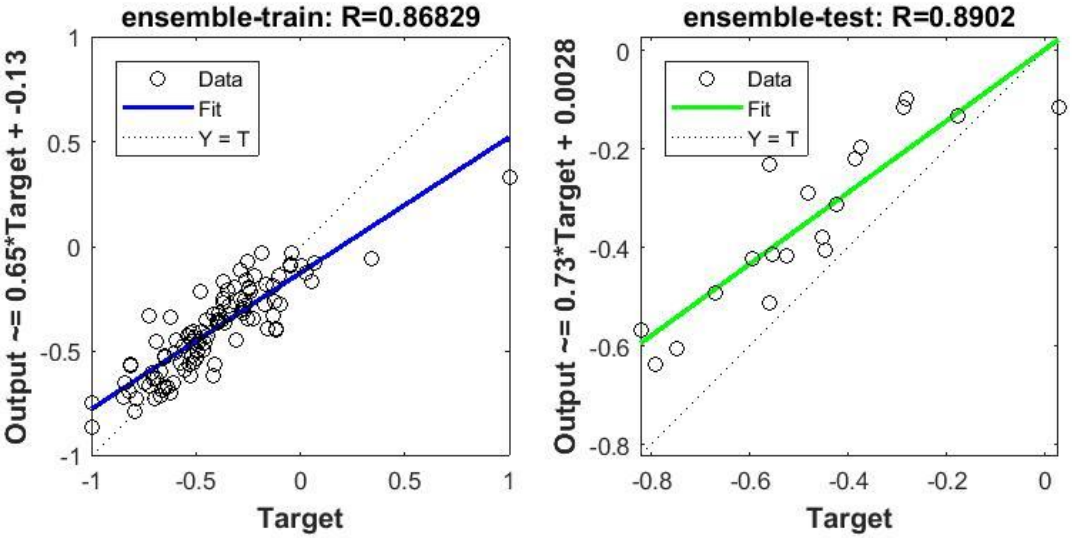

Figure 4-4. Performance of NARX model for seasonal dissolved oxygen of ULM. The left and right plots shown training and validation performance, respectively. Output and Target denote ensemble results and observation data, respectively, normalized into the range [-1, 1].

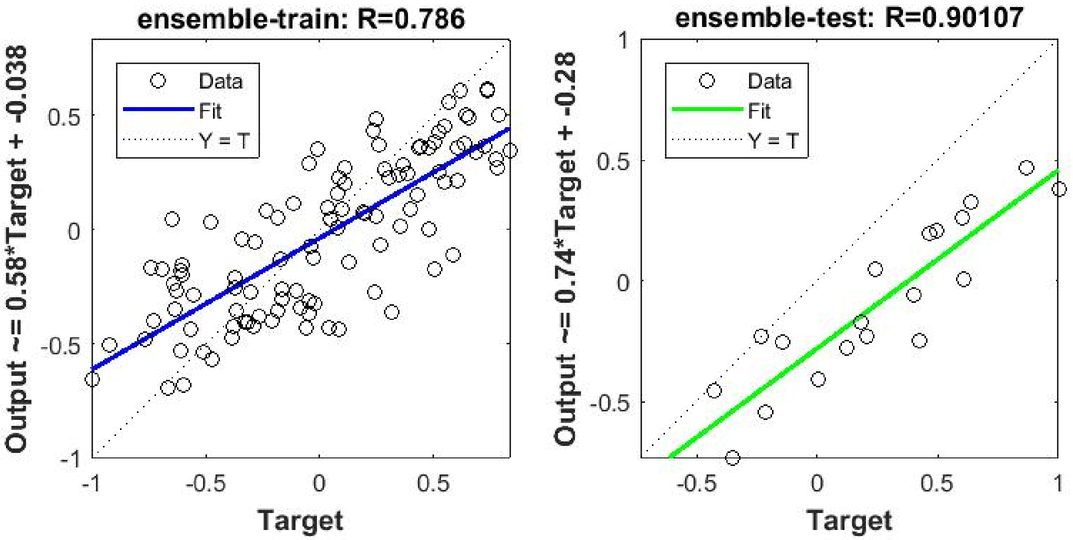

Figure 4-5 Performance of NARX model for seasonal salinity of ULM. The left and right plots shown training and validation performance, respectively. Output and Target denote ensemble results and observation data, respectively, normalized into the range [-1, 1].

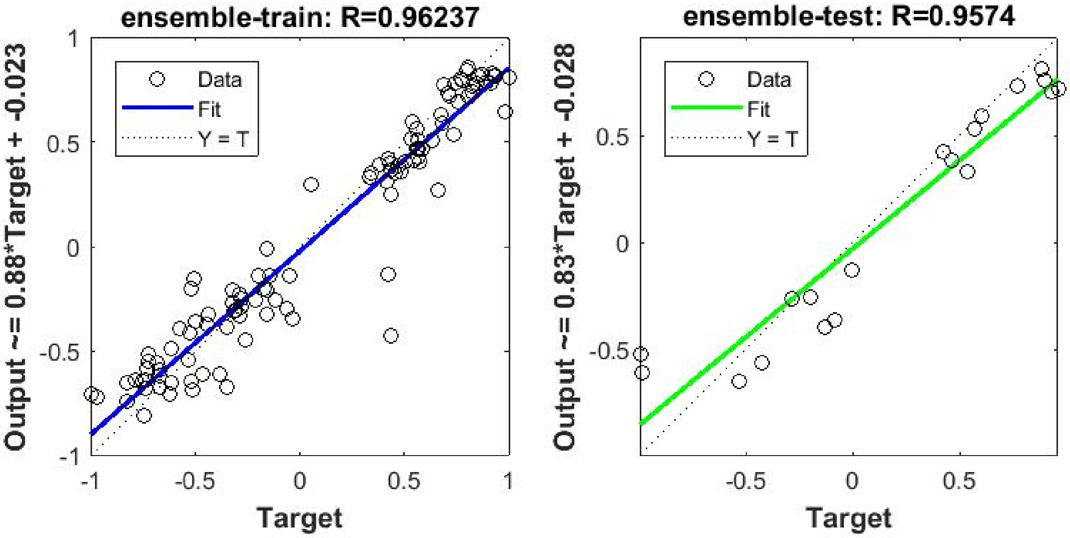

Figure 4-6. Performance of NARX model for seasonal water temperature of ULM. The left and right plots shown training and validation performance, respectively. Output and Target denote ensemble results and observation data, respectively, normalized into the range [-1, 1].

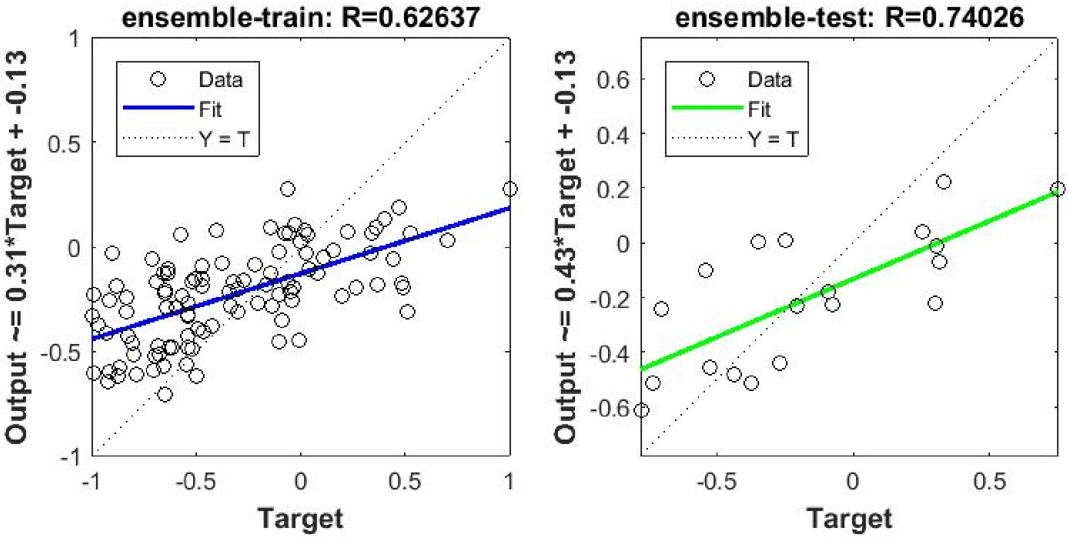

Figure 4-7. Performance of NARX model for seasonal turbidity of ULM. The left and right plots shown training and validation performance, respectively. Output and Target denote ensemble results and observation data, respectively, normalized into the range [-1, 1].

4.2 MCCA model

An integrated Markov-Chain Cellular-Automata model was developed to generate the forecasting of coastal urbanization and habitat changes. Markov Chain is an effective approach to estimate future change based on the past, while Cellular Automata is spatially explicit method to estimate where the change would occur. The combination of the two methods have been recognized a powerful modeling technique for the simulation of land cover changes at different scales.

The performance of MCCA models is often subject to limitations in identifying clear transition rules. In contrast to the short period (i.e., 10-15 years) in existing studies, the multi-decade span effectively in this project reduced the uncertainty in transition demand, i.e., the total amount of land-use change occurring in each time step among different land use categories. The raster schematization of the upper Laguna Madre region was achieved by examining the upscaling of Landsat image pixels in the range of 90-300 meters. Such resolutions were considered sufficient to reflect the fragmentation, degradation and conversion of habitat features and the growth of impervious surfaces in coastal environments. The model development emphasized: (i) the definition of an initial cell status based on land cover time series derived from satellite images; (ii) the iterative generation of a new cell status at each successive temporal step (i.e., one year or longer); and (iii) the time invariant functions for defining how the new status of a cell was determined by its previous status and the status of cells in its neighborhood. Cells of non-urban land were available to be replaced by cells of urban land, but the inversible process were not allowed to occur. Two schemes of the growth of urban land cells were considered in this study: random expansion and rule-based expansion. The random scheme assigned equal urbanized probability to all available cells. The rule-based scheme followed rational criteria, which was an urbanization probability matrix of all land cover categories derived from the 30-year land cover time series with consideration on the distance to shoreline, elevation and slope, the total number of contiguous urban cells, and the total number of urban cells in the neighborhood.

In this project, the predictor variables addressed a set of natural and anthropogenic factors such as: distance to impervious surface, distance to major roads, distance to preserved areas such as parks and recreational areas, distance to waterbodies, elevation, and slope (Figure 4-8 and Supplementary Information). The model described the transition among multiple coastal land cover categories including developed open space, developed surface, barren land, forest/woods wetland, shrubland, grassland, cropland, pasture, woody wetlands, and herbaceous wetlands. The transition areas and probabilities determined from Markov Chain analysis using two prior land use maps established the quantity of expected land cover change from each existing category to each of other categories in the next time period (Tables 4-1 and 4-2).

Patterns of suitability for difference land cover categories were produced using multi criteria evaluation, which combined a set of criteria images to achieve a single composite basis for a decision according to a specific objective (e.g., a single suitability map from which the final choice will be made). This information established the inherent suitability of each pixel for each land cover type. A contiguity filter was used to adjust the suitability of pixels far from existing areas of that class (as of that iteration), thus giving preference to contiguous suitable areas. This filter was integral to the action of the Cellular Automata component. It automatically normalized the filter kernel to force the values to sum to 1. It was passed over a Boolean image for each class from the current land cover image within each iteration. The net effect was that to be a likely choice for land cover conversion, the pixel must be both inherently suitable and near to existing areas of that class.

Figure 4-9 shows an example of the conditional probability maps derived from historical land cover changes. These maps indicate the probability that each land cover type would be found at each pixel after the specified number of time steps in forecasting. Within each time step, each land cover was considered as a target category, and all other land cover categories competed for land within the target category. The cellular automat component provided the filter for the Markov-chain component for down-weighting the conversion suitability of pixels that were distant from existing land cover categories under consideration, resulting in the pixel-wise quantification of a likely choice for land cover conversion. The conditional probability maps of other change classes are presented in Supplementary Information. The MCCA model was implemented to generate the forecasting of ULM habitat change under urbanization from the baseline using present situation (Figure 4-10).

Figure 4-8. The predictor variables based on the distance to impervious surface. Other predictor variables are presented in Supplementary Information.

Table 4-1. Matrix of transition areas.

	Class 1	Class 2	Class 3	Class 4	Class 5	Class 6	Class 7	Class 8	Class 9
Class 1	2729510	296	283	4706	1887	1837	3260	387	7236
Class 2	0	517549	0	0	0	0	0	0	0
Class 3	0	17379	366667	0	0	0	0	0	0
Class 4	20853	2419	423	191803	132	293	2000	387	43291
Class 5	1395	3844	2326	112	801850	46861	6537	600	13906
Class 6	1054	6143	3044	615	66937	4050452	19692	14363	415
Class 7	860	11998	4505	1728	2136	39342	1113206	9979	553
Class 8	1295	22913	10378	3731	6952	51726	30838	6388641	355
Class 9	21890	1799	694	218	32435	1086	584	73	883465

Table 4-2. Matrix of transition probabilities.

	C1	Class 2	Class 3	Class 4	Class 5	Class 6	Class 7	Class 8	Class 9
Class 1	0.9928	0.0001	0.0001	0.0017	0.0007	0.0007	0.0012	0.0001	0.0026
Class 2	0.0000	1.0000	0.0000	0.0000	0.0000	0.0000	0.0000	0.0000	0.0000
Class 3	0.0000	0.0453	0.9547	0.0000	0.0000	0.0000	0.0000	0.0000	0.0000
Class 4	0.0797	0.0092	0.0016	0.7332	0.0005	0.0011	0.0076	0.0015	0.1655
Class 5	0.0016	0.0044	0.0027	0.0001	0.9139	0.0534	0.0075	0.0007	0.0158
Class 6	0.0003	0.0015	0.0007	0.0001	0.0161	0.9730	0.0047	0.0035	0.0001
Class 7	0.0007	0.0101	0.0038	0.0015	0.0018	0.0332	0.9400	0.0084	0.0005
Class 8	0.0002	0.0035	0.0016	0.0006	0.0011	0.0079	0.0047	0.9803	0.0001
Class 9	0.0232	0.0019	0.0007	0.0002	0.0344	0.0012	0.0006	0.0001	0.9376

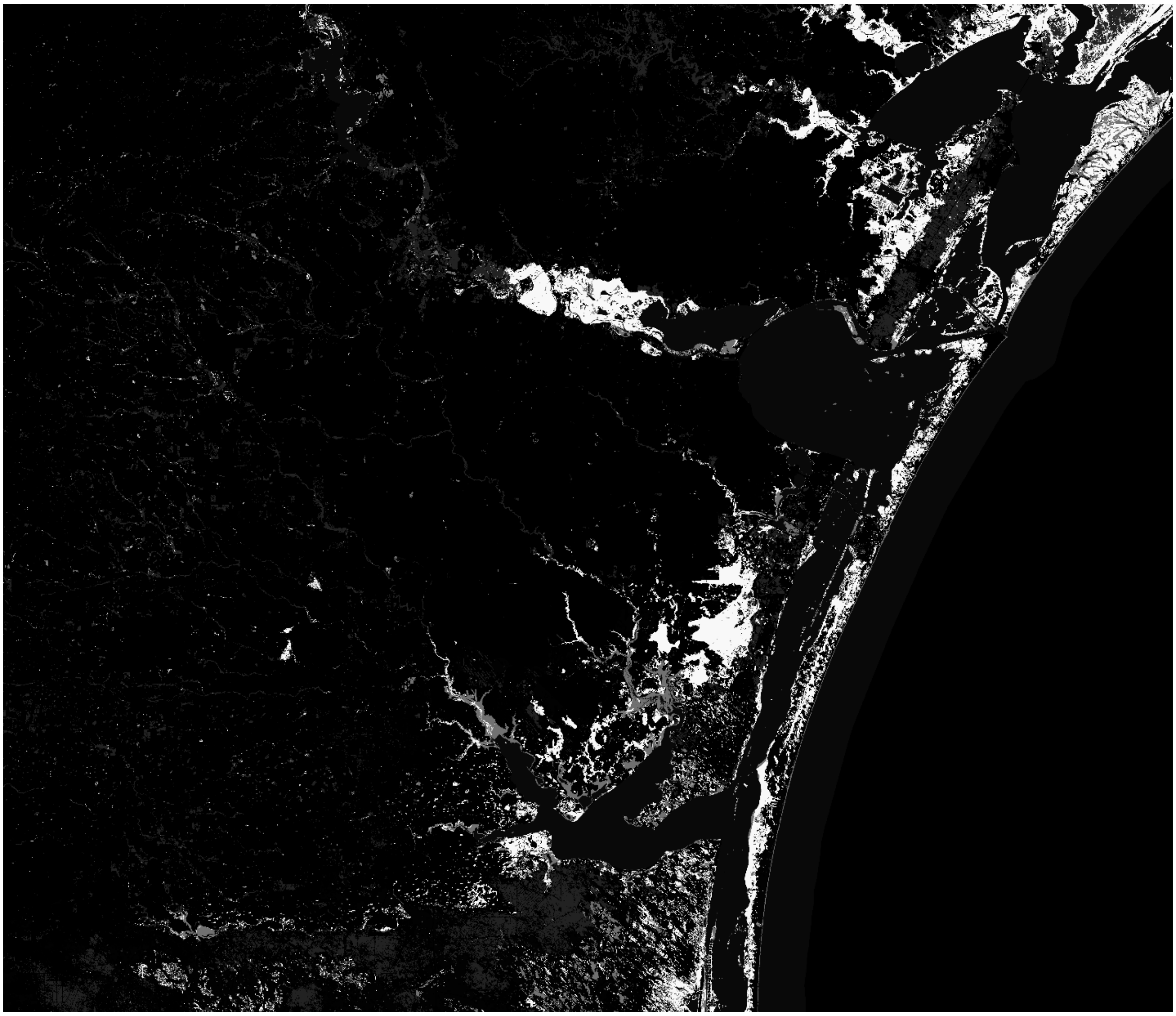

Figure 4-9. The conditional probability map of the change class 6. The maps of other change classes are presented in Supplementary Information.

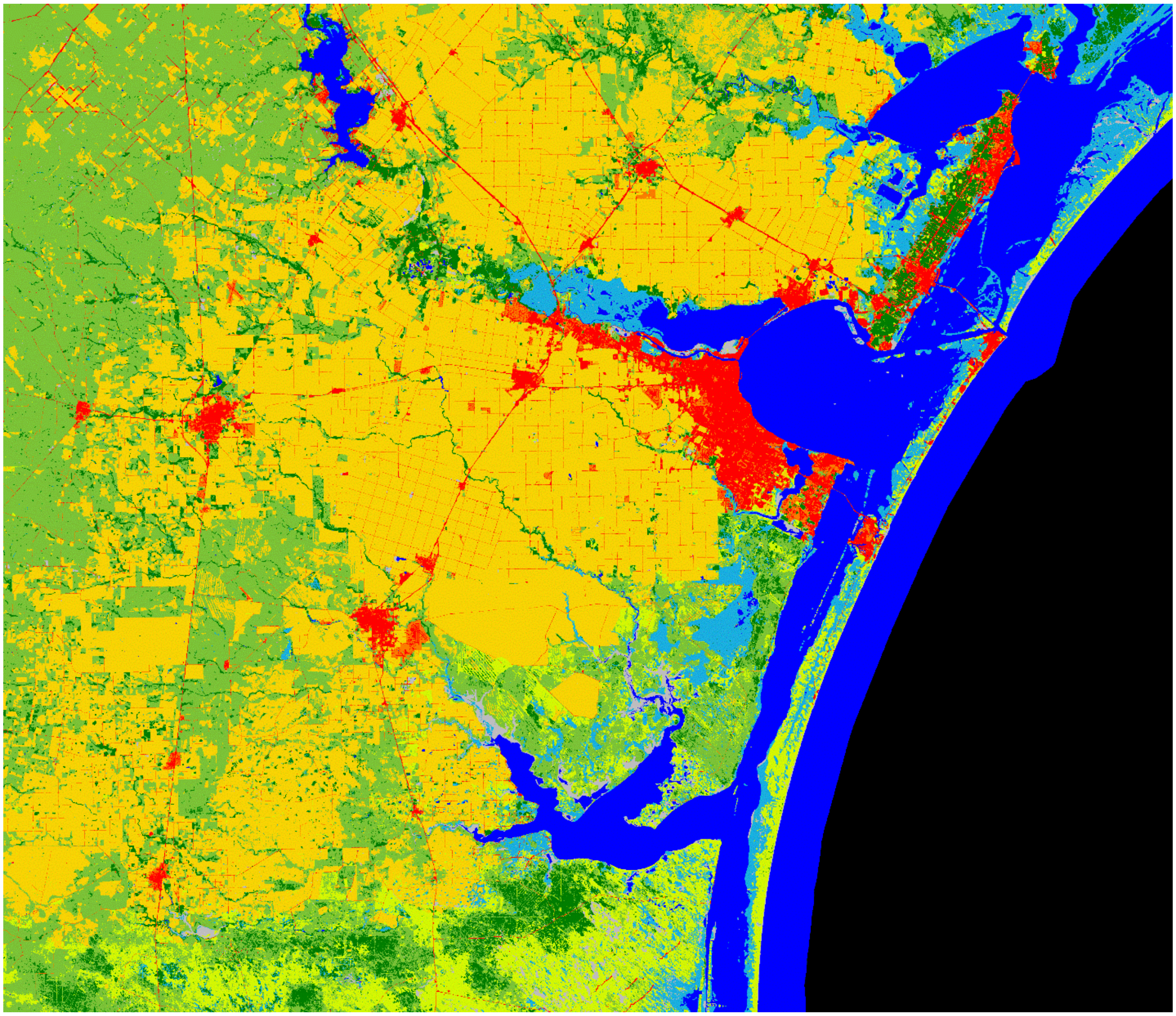

Figure 4-10. Projected condition of future land cover and habitat in ULM.

5. Outreach and Decision Support

5.1 Outreach

Aligned with the activities of the Aquatic Education Program (AEP) at the Center for Coastal Studies, the project team translated research findings into a protocol of educational materials targeted at grade 6-12 students. The designed class activities are centered on the hands-on practice of building a comparative "*Impervious vs. Permeable*" urban-rural substrate model and observing the change in runoff and its contaminant-carrying compacity in different settings.

Academic Question:

- How does the increase of impervious surfaces effect runoff and contribute to the enhanced export of contaminants?

Objective:

- To design and model an urban and rural substrate.
- To observe runoff in both an urban (impervious) setting and a more rural (permeable) environment.

Background:

- Over half the Earth's population now resides in cities. Population growth and urbanization rates in low elevation coastal zones are particularly outpacing the demographic development of inland regions. A characteristic indicator of urbanization is the increase of impervious surface, a unique land cover category that involves paved roads, sidewalks, parking lots, buildings, and other built structures, through which precipitation does not readily infiltrate into the underlying soil.
- Impervious surface affects hydrological and energy balances, as well as biological composition and ecosystem functions. Increase in impervious surface results in higher nutrient loads, increased hyposalinity impacts, elevated surface temperature, increased peak flow, and accelerated habitat degradation in many coastal urban areas and watersheds.

- The Corpus Christi-Kingsville area surrounding the Upper Laguna Madre is a fast-growing coastal area in Texas. Since 1970, its population and impervious coverage have increased by 53% and 45%, respectively. The population is projected to have a 27.5% increase by 2050, which could result in the addition of more than 100 km2 of impervious surface and an unprecedented challenge to ecosystem health and resilience.

Materials:

- Disposable foil bread pan
- Several small sponges ½ inch in height
- Scissors
- Spray Bottle of water
- Dark colored flavor of "Kool Aid" packet
- Light colored can of "Play-do" molding clay
- ½-1 inch thick book

Process:

- Begin with a brief discussion of urban and rural environments and guide the students in how their respective "substrates" are different (soil/concrete).
- Have them also discuss how the different areas have been altered by nature and humans, and how rainfall collects and/or runs off.

Rural Model:

- Have the students design a rural environment by adding and shaping sponges to fit one side of the aluminum pan and leaving the other side empty. The sponges will represent the more permeable soils found in urban areas. Have the students tilt up the sponge end of the pan on a book to raise this end approximately 1 inch to represent the gradient towards the open water end. Have the students fill their spray bottle to the top and then gently spray the water onto the land portion of the model. Observe how the rural permeable surface absorbs quite a bit of the water. Sprinkle a bit of the package of "kool aid" to represent possible contamination added to the substrate and again add more water. When the color from the "contaminants" begin to wash into the open water area of the pan (bay or lake), record the volume of water used from within the spray bottle.

Urban Model:

- Have the students rinse and clean their sponges and pan from the previous rural model. Once done, refill their spray bottle to the top with water. Rebuild the model like the previous model only this time flatten out the "play-do" (to simulate concrete) and cover over the sponges. Be sure to extend the play-do all the way to the edge of the open bay/lake area. Spray some water and observe how much of the liquid rushes off to the open area. Add the "kool-aid" contaminants and continue to spray until color is observed and collected in the open area. Record the volume of water used from within the spray bottle.

Application:

- This simple experiment should demonstrate how more impervious surfaces increase runoff and can lead to the enhanced export of contaminants to local bodies of water.

Evaluation/Extension

- Have the student research wetland functions and values and repeat the process adding various smaller wetlands and/or depressions.
- Have the students prepare water drainage questions to ask a representative from the local water drainage department.
- Have the students prepare a list of potential contaminants from both rural and urban environments.

Time Frame:

- One class period

Grade Level:

- 6-12

5.2 Decision support

Integrated decision support systems were developed using the state-of-the-art technology of Google Earth Engine Apps. It provides an effective means to create dynamic, publicly accessible user interfaces that can visualize and demonstrate the geospatial datasets for users. It allows the researches to take the advantage of a variety of interface elements and functions, leverage GEE’s data catalog and analytical power, assimilate customized research from multiple tasks, and engage stakeholders of both experts and non-experts alike. Through accessing client-side user interface (UI) widgets to construct graphical interfaces, the decision support systems can include simple input widgets like buttons and checkboxes, more complex widgets like charts and maps, panels to control the layout of the UI, and event handlers for interactions between UI widgets. Decision support systems based on GEE Apps are publicly accessible to the world from the application-specific URL generated at time of publishing. All users can view and interact with the tools without the need for register for a GEE account.

The decision support systems developed in this project employed a variety of widget and layout tools from Google Earth Engine Apps, such as ui.Lable, ui.Button, ui.Checkbox, ui.Slider, ui.DateSlider, uiTextbox, ui.Select, ui.Chart, ui.Map, ui.Map.Layer, ui.Map.Linker, ui.Panel, ui.SplitPanel. In particular, ui.Slider and ui.DateSlider allowed a user to adjust a slider to get a number within the slider range. The range of slider was configured using either the constructor or by setting properties of the slider (e.g., dates). The ui.DateSlider was useful for presenting a collection of geospatial data such as satellite images acquired in different years. Also, the ui.Map.Linker was used to synchronize the movement of multiple maps, so a user could easily compare different images (e.g., satellite images and aerial images) across different scales on the same screen. Many of these functions were tested in advance during image analysis and change detection (Figure 5-1). These preliminary efforts improved the efficiency of research tasks and gained valuable experience for develop the interface of decision support systems.

A set of three decision support systems were developed, including DSS1 – Data Management, DSS2 – Urbanization, and DSS3 – Habitat Change. DSS1 focuses on a systematic demonstration of the image data (Figure 5-2). The left panel shows the 34-year annual 30-m satellite data including three layers: RGB, NDVI and NDWI. The satellite data consist of 30-m Landsat 5 TM (1984-2012,), Landsat 7 ETM+ (1999-present), and Landsat 8 OLI (2013-

present) imagery, across a number of spectral bands: blue, green, red, near-infrared, and shore-wave infrared. The right panel shows the shows the biannual 1-m NAIP aerial imagery (2004-present, 3 or 4 bands). When a user clicks any point on the left panel, a time series chart will be generated to exhibit the change of surface reflectance and spectral indices over 30 years. In each panel, by using the date slider, a user can review the image of a particular year of interest and have an unprecedent experience of the coastal change in ULM over time. More importantly, as DSS1 is dynamically linked to the catalog of GEE, it will be automatically updated if new satellite or aerial images have been acquired and added to GEE. This ensures a better applicability and suitability with minimum maintenance cost, compared to other coastal decision support tools that are often affected by resource constraints and time lags due to local data storage and management.

DSS2 focuses on the spatial pattern and temporal characteristics of urbanization in ULM (Figure 5-3). The dataset shown is the age of impervious surface that consists of seven five-year categories, which is an important output of this project. As the development of impervious surface is a unidirectional process, the duration of imperviousness essentially reveals the trajectory of the urbanization process. Urban areas developed before 1984 would have the maximum duration. Newly-built areas are younger, and their ages suggest the timing of their construction. Through viewing the expansion of impervious surface in ULM across space and over time at different scales, a user can understand two fundamental interlinked patterns of urbanization: (i) intensification, the gradually filling of pervious gaps within existing developed areas, and (ii) expansion, the fast encroachment of farmlands and natural areas that are fringing urban centers.

DSS3 focuses on the change of habitat coupled with coastal urbanization (Figure 5-4). The dataset shown consisted over 40 types of changes among different habitat and land cover categories, demonstrating both the loss and gain of each habitat at the pixel level. A detailed legend of these change classes is presented in the widget to help users to understand the specific meaning of each color in the map. The base map layer of the system can be changed by the user, switching between a plain map with more details of roads and settlements or a satellite map with more landscape information.

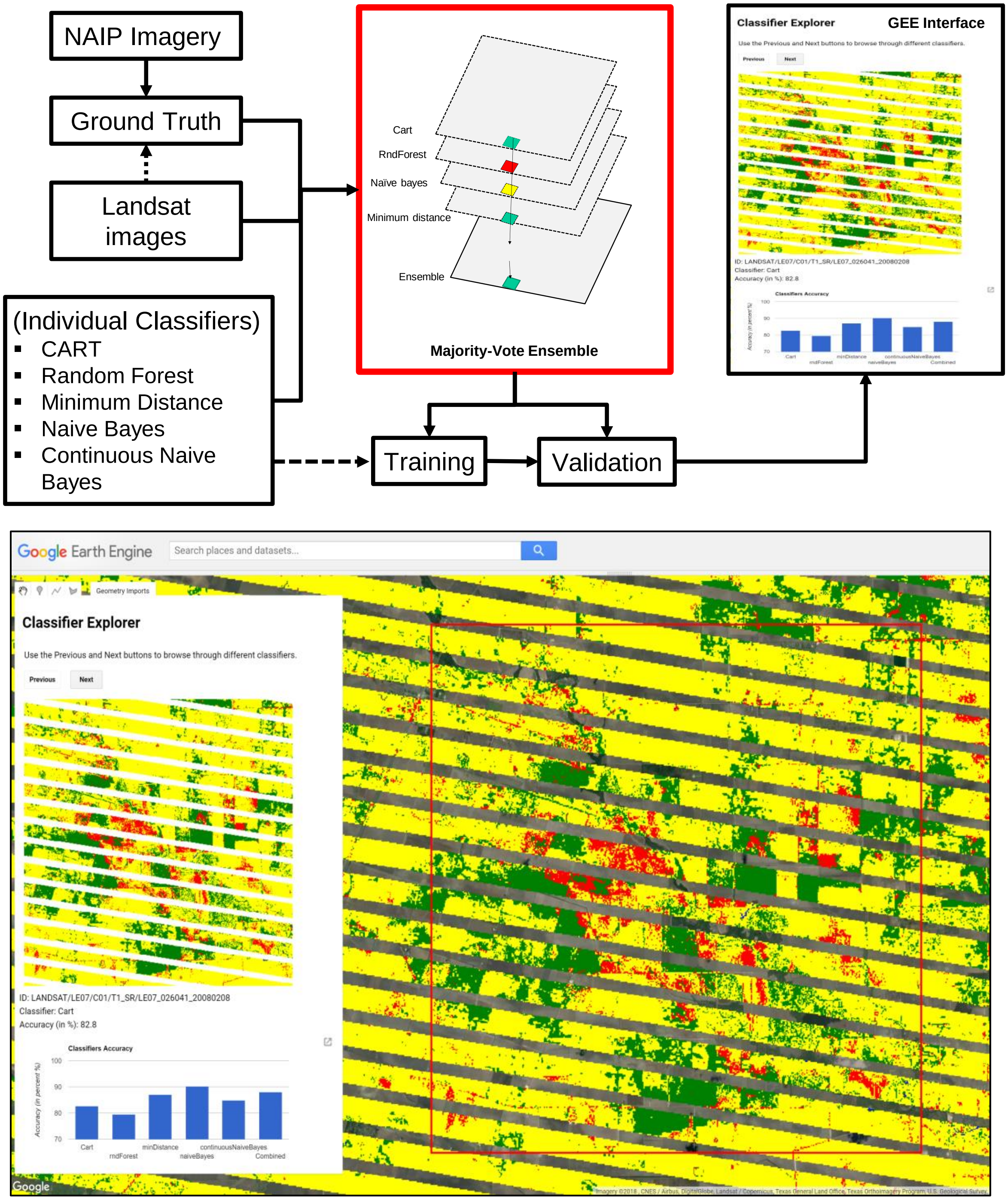

Classifier Explorer

Use the Previous and Next buttons to browse through different classifiers.

ID: LANDSAT/LE07/C01/T1_SR/LE07_026041_20080208
Classifier: Cart
Accuracy (in %): 82.8

Figure 5-1. A prototype of the land cover classification tool bases on Google Earth Engine.

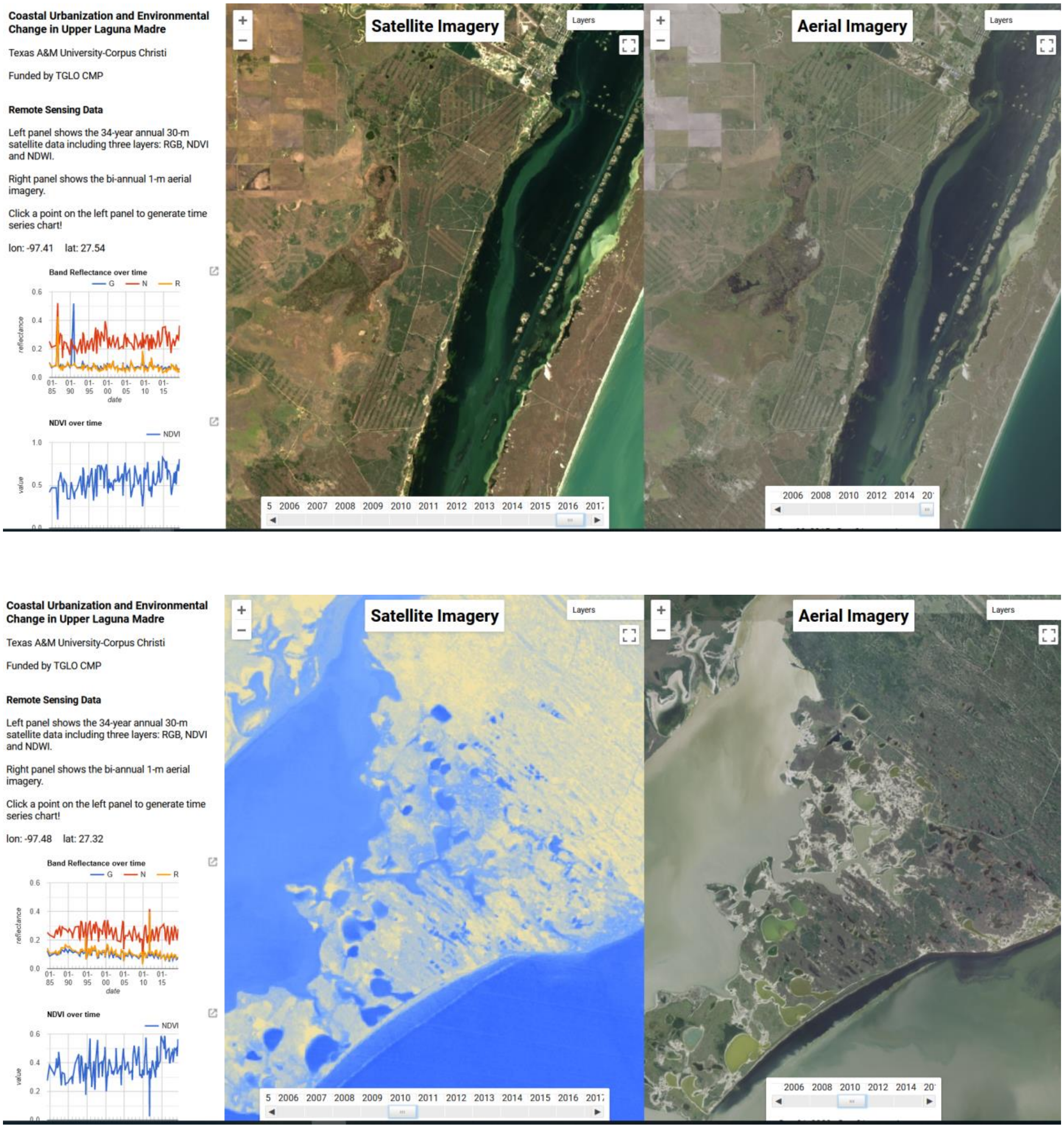

Coastal Urbanization and Environmental Change in Upper Laguna Madre

Texas A&M University-Corpus Christi

Funded by TGLO CMP

Remote Sensing Data

Left panel shows the 34-year annual 30-m satellite data including three layers: RGB, NDVI and NDWI.

Right panel shows the bi-annual 1-m aerial imagery.

Click a point on the left panel to generate time series chart!

lon: -97.41 lat: 27.54

Coastal Urbanization and Environmental Change in Upper Laguna Madre

Texas A&M University-Corpus Christi

Funded by TGLO CMP

Remote Sensing Data

Left panel shows the 34-year annual 30-m satellite data including three layers: RGB, NDVI and NDWI.

Right panel shows the bi-annual 1-m aerial imagery.

Click a point on the left panel to generate time series chart!

lon: -97.48 lat: 27.32

Figure 5-2. The interface of Decision Support System 1 - Data Management**.** The system is accessible at: https://huazhang211.users.earthengine.app/view/ulm-dss-1.

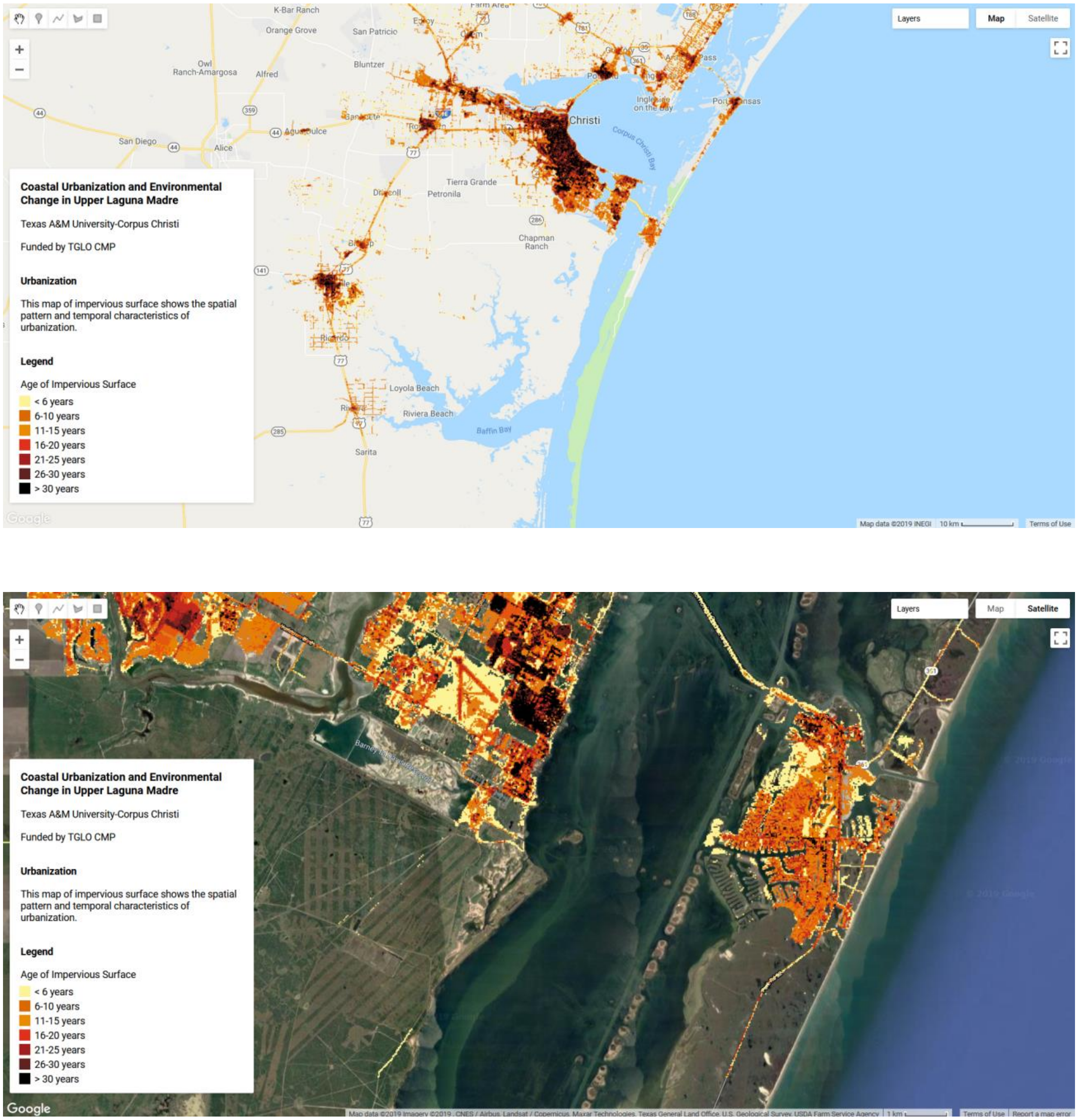

Coastal Urbanization and Environmental Change in Upper Laguna Madre

Texas A&M University-Corpus Christi

Funded by TGLO CMP

Urbanization

This map of impervious surface shows the spatial pattern and temporal characteristics of urbanization.

Legend

Age of Impervious Surface

- < 6 years
- 6-10 years
- 11-15 years
- 16-20 years
- 21-25 years
- 26-30 years
- > 30 years

Coastal Urbanization and Environmental Change in Upper Laguna Madre

Texas A&M University-Corpus Christi

Funded by TGLO CMP

Urbanization

This map of impervious surface shows the spatial pattern and temporal characteristics of urbanization.

Legend

Age of Impervious Surface

- < 6 years
- 6-10 years
- 11-15 years
- 16-20 years
- 21-25 years
- 26-30 years
- > 30 years

Figure 5-3. The interface of Decision Support System 2 - Urbanization**.** The system is accessible at: https://huazhang211.users.earthengine.app/view/ulm-dss-2.

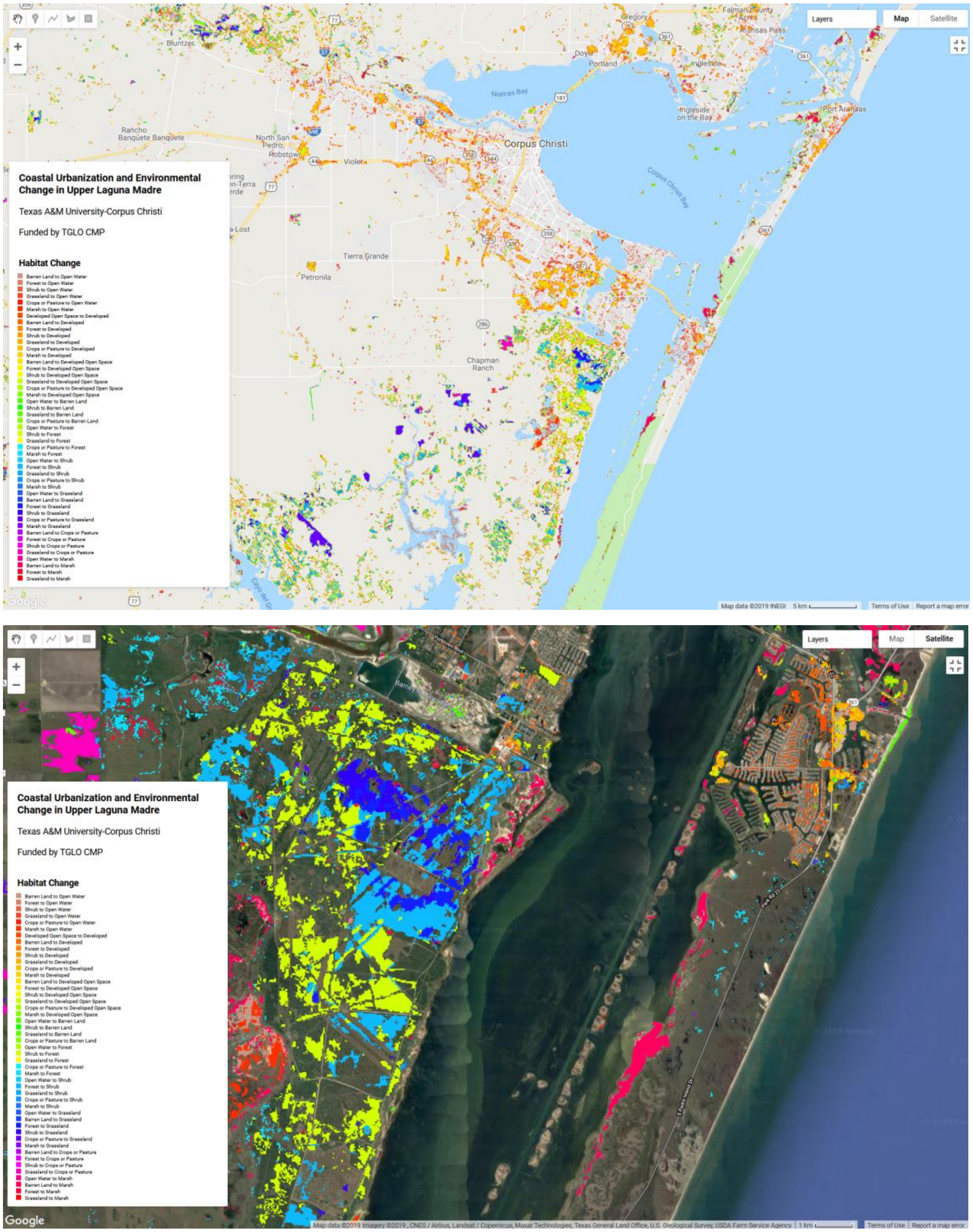

Figure 5-4. The interface of Decision Support System 3 – Habitat Change**.** The system is accessible at: https://huazhang211.users.earthengine.app/view/ulm-dss-3.

6. Conclusions

Ample studies have shown that the expansion of impervious surface is associated with the health and productivity of estuarine ecosystems, but the pattern and trend of this effect is not well understood at the regional scale and over the long term. A better understanding of the dynamics of this stress is essential toward increasing public awareness, developing sustainable strategies for land use planning, and managing freshwater inflows, nutrients, and sediments entering the estuaries. By understanding the spatiotemporal dynamics of impervious surface and its linkages to water quality degradation and habitat fragmentation, we can better understand what strategies and practices are needed to minimize the stress caused by coastal development. This project aimed to qualitatively analyze the impact of coastal development in the Corpus Christi-Kingsville metropolitan area on the water and habitat quality of ULM over the past four decades. Project activities consisted of several interlinked tasks over two years, starting with hydrological monitoring and analysis, transitioning into comprehensive remote sensing and predictive modeling, and culminating in outreach and decision support efforts.

The hydrological monitoring efforts resulted in the establishment of the first evaporation pan station in ULM. Observations at this station provided essential information to estimate monthly evaporation rates in the shallow, hypersaline ULM. Such results were extended to adjust an existing state freshwater dataset that was mainly based on evaporation stations outside UTM. The results led to the reconstructed monthly freshwater balance of ULM since January 1977.

Long-term landscape changes in ULM and its neighborhoods were characterized using a combination of satellite and aerial imagery using Google Earth Engine. Ground truth was established based on data from field surveys using small unmanned aerial vehicles and historical images from the National Agriculture Imagery Program. We developed a hybrid method to estimate annual changes of impervious surface using the time series of Landsat imagery. It built seasonal composite images within a multi-year window, trained a classification model using multiple spectral predictors, and improved the initial classification results by temporal filtering. We further developed a pseudoinvariant near-infrared threshold method for converting digital numbers into surface reflectance based on pseudoinvariant pixels identified from Landsat imagery.

The extensive remote sensing efforts provided inputs to the development of different analytic models for analyzing urbanization-induced stress on estuarine water quality and habitat, including: (i) a nonlinear autoregressive network ensemble with exogenous inputs as a cost-effective tool to characterize nonlinear relationships; (ii) an integrated Markov-Chain Cellular-Automata model as a spatially-explicit tool to estimate the evolution of landscape. These predictive tools could generate future patterns of land cover and habitat under different scenarios of environmental change and socioeconomic development, providing essential information for the planning and management of coastal land and water resources.

Finally, a set of decision support systems was established for enhancing the awareness of urbanization process and its impact on coastal ecosystems. Built on Google Earth Engine Apps, these decision support systems are publicly accessible to the world, and users can view and interact with the tools without the need to register for a Google Earth Engine account.

The achievements of this project highlighted the advantages of Google Earth Engine, a revolutionary geospatial tool that can process decadal satellite images through customized algorithms and cloud computation. The integration of Google Earth Engine, process-baes models, and analytic tools provided a highly-efficient means to analyze the spatiotemporal dynamics of linkages among regional impervious surface, freshwater fluxes, and estuarine health over the long term. Results this project have been disseminated through peer-reviewed papers and GIS platforms. They could provide scientific support to state agencies and local stakeholder in ULM and other coastal regions and inform the development of effective management and conservation strategies.

Overall, this project provided an improved understanding of long-term environmental and ecological consequences of urbanization in ULM. The data and tools derived from this project could help scientists and managers to better manage coastal land and water resources and to ensure adequate and appropriately-timed freshwater inflow to the environment. In doing so, this project contributed to the development of sustainable development strategies that could provide needed jobs, stimulate economic activity, minimize the stress on coastal ecosystems, and ascertain the sources and timing of freshwater inflows needed to protect the quality and functions of coastal natural resource areas in ULM. Through generating the first dataset of 35-year changes of impervious surface and estuarine habitats and disseminating them through online GIS platforms, this project provided the public with a real-world example with comprehensive materials to link regional, long-term urbanization processes to the overall health of coastal ecosystems. The deliverables of this projected could help fulfill the public need to know the health of their bays and estuaries and the complex effects of urbanization on various coastal natural resource areas.

References

Alcázar, J., Palau, A., Vega-Garcı´a, C., 2008. A neural net model for environmental flow estimation at the Ebro River Basin, Spain. Journal of Hydrology, 349(1-2): 44-55. DOI:10.1016/j.jhydrol.2007.10.024

Anderson, C., Carter, G., Funderburk, W., 2016. The Use of Aerial RGB Imagery and LIDAR in Comparing Ecological Habitats and Geomorphic Features on a Natural versus Man-Made Barrier Island. Remote Sensing, 8(7). DOI:10.3390/rs8070602

Arnold, C.L., Gibbons, C.J., 1996. Impervious surface coverage - The emergence of a key environmental indicator. Journal of the American Planning Association, 62(2): 243-258. DOI:10.1080/01944369608975688

Barrie, G.M., Worden, R.H., Barrie, C.D., Boyce, A.J., 2015. Extensive evaporation in a modern temperate estuary: Stable isotopic and compositional evidence. Limnol. Oceanogr., 60(4): 1241-1250. DOI:10.1002/lno.10091

Bighash, P., Murgulet, D., 2015. Application of factor analysis and electrical resistivity to understand groundwater contributions to coastal embayments in semi-arid and hypersaline coastal settings. Sci Total Environ, 532: 688-701. DOI:10.1016/j.scitotenv.2015.06.077

Bishop, B., Dietterick, B., White, R., Mastin, T., 2014. Classification of Plot-Level Fire-Caused Tree Mortality in a Redwood Forest Using Digital Orthophotography and LiDAR. Remote Sensing, 6(3): 1954-1972. DOI:10.3390/rs6031954

Brabec, E., Schulte, S., Richards, P.L., 2002. Impervious surfaces and water quality: A review of current literature and its implications for watershed planning. Journal of Planning Literature, 16(4): 499-514. DOI:10.1177/088541202400903563

Bumguardner, M.L., Munster, C.L., Provin, T., Ha, M., 2013. SOIL LOSS DUE TO RESIDUE REMOVAL IN THE OSO CREEK WATERSHED, TEXAS. Trans. ASABE, 56(1): 83-90.

Buzzelli, C., Doering, P.H., Wan, Y., Sun, D., Fugate, D., 2014. Modeling ecosystem processes with variable freshwater inflow to the Caloosahatchee River Estuary, southwest Florida. I. Model development. Estuarine, Coastal and Shelf Science, 151: 256-271. DOI:10.1016/j.ecss.2014.08.028

Byrd, K.B. et al., 2018. A remote sensing-based model of tidal marsh aboveground carbon stocks for the conterminous United States. ISPRS Journal of Photogrammetry and Remote Sensing, 139: 255-271. DOI:10.1016/j.isprsjprs.2018.03.019

Campbell, J.B., Wynne, R.H., 2011. Introduction to Remote Sensing. The Guilford Press.

Cannon, A.J., Whitfield, P.H., 2002. Downscaling recent streamflow conditions in British Columbia, Canada using ensemble neural network models. Journal of Hydrology, 259(1–4): 136-151. DOI:http://dx.doi.org/10.1016/S0022-1694(01)00581-9

Chan, J.C.W., Paelinckx, D., 2008. Evaluation of Random Forest and Adaboost tree-based ensemble classification and spectral band selection for ecotope mapping using airborne hyperspectral imagery. Remote Sensing of Environment, 112(6): 2999-3011. DOI:10.1016/j.rse.2008.02.011

Cianfrani, C., Satizábal, H.F., Randin, C., 2015. A spatial modelling framework for assessing climate change impacts on freshwater ecosystems: Response of brown trout (Salmo trutta L.) biomass to warming water temperature. Ecological Modelling, 313: 1-12. DOI:10.1016/j.ecolmodel.2015.06.023

Di, Q. et al., 2016. Assessing PM2.5 Exposures with High Spatiotemporal Resolution across the Continental United States. Environ Sci Technol, 50(9): 4712-21. DOI:10.1021/acs.est.5b06121

Feng, M. et al., 2013. Global surface reflectance products from Landsat: Assessment using coincident MODIS observations. Remote Sensing of Environment, 134: 276-293. DOI:10.1016/j.rse.2013.02.031

Flood, N., 2014. Continuity of Reflectance Data between Landsat-7 ETM+ and Landsat-8 OLI, for Both Top-of-Atmosphere and Surface Reflectance: A Study in the Australian Landscape. Remote Sensing, 6(9): 7952-7970. DOI:10.3390/rs6097952

Foga, S. et al., 2017. Cloud detection algorithm comparison and validation for operational Landsat data products. Remote Sensing of Environment, 194: 379-390. DOI:10.1016/j.rse.2017.03.026

Froeschke, B.F., Tissot, P., Stunz, G.W., Froeschke, J.T., 2013. Spatiotemporal Predictive Models for Juvenile Southern Flounder in Texas Estuaries. North American Journal of Fisheries Management, 33(4): 817-828. DOI:10.1080/02755947.2013.811129

Gevaert, C.M., Persello, C., Sliuzas, R., Vosselman, G., 2017. Informal settlement classification using point-cloud and image-based features from UAV data. ISPRS Journal of Photogrammetry and Remote Sensing, 125: 225-236. DOI:10.1016/j.isprsjprs.2017.01.017

Gillson, J., 2011. Freshwater Flow and Fisheries Production in Estuarine and Coastal Systems: Where a Drop of Rain Is Not Lost. Reviews in Fisheries Science, 19(3): 168-186. DOI:10.1080/10641262.2011.560690

Gobel, P., Dierkes, C., Coldewey, W.C., 2007. Storm water runoff concentration matrix for urban areas. Journal of Contaminant Hydrology, 91(1-2): 26-42. DOI:10.1016/j.jconhyd.2006.08.008

Gong, P. et al., 2013. Finer resolution observation and monitoring of global land cover: first mapping results with Landsat TM and ETM+ data. International Journal of Remote Sensing, 34(7): 2607-2654. DOI:10.1080/01431161.2012.748992

Granitto, P.M., Verdes, P.F., Ceccatto, H.A., 2005. Neural network ensembles: evaluation of aggregation algorithms. Artificial Intelligence, 163(2): 139-162. DOI:10.1016/j.artint.2004.09.006

Gray, J., Song, C., 2013. Consistent classification of image time series with automatic adaptive signature generalization. Remote Sensing of Environment, 134: 333-341. DOI:https://doi.org/10.1016/j.rse.2013.03.022

Hadjimitsis, D.G., Clayton, C.R.I., Retalis, A., 2009. The use of selected pseudo-invariant targets for the application of atmospheric correction in multi-temporal studies using satellite remotely sensed imagery. International Journal of Applied Earth Observation and Geoinformation, 11(3): 192-200. DOI:10.1016/j.jag.2009.01.005

Hagan, M.T., Menhaj, M.B., 1994. Training feedforward networks with the Marquardt algorithm. IEEE Transactions on Neural Networks, 5(6): 989-993. DOI:10.1109/72.329697

Hamedianfar, A., Shafri, H.Z.M., Mansor, S., Ahmad, N., 2014. Improving detailed rule-based feature extraction of urban areas from WorldView-2 image and lidar data. International Journal of Remote Sensing, 35(5): 1876-1899. DOI:10.1080/01431161.2013.879350

Hansen, L.K., Salamon, P., 1990. Neutral Network Ensembles. Ieee Transactions on Pattern Analysis and Machine Intelligence, 12(10): 993-1001. DOI:10.1109/34.58871

Hart, S.J., Veblen, T.T., 2015. Detection of spruce beetle-induced tree mortality using high- and medium-resolution remotely sensed imagery. Unknown.

Hartfield, K., van Leeuwen, W., 2018. Woody Cover Estimates in Oklahoma and Texas Using a Multi-Sensor Calibration and Validation Approach. Remote Sensing, 10(4). DOI:10.3390/rs10040632

Heydari, S.S., Mountrakis, G., 2018. Effect of classifier selection, reference sample size, reference class distribution and scene heterogeneity in per-pixel classification accuracy using 26 Landsat sites. Remote Sensing of Environment, 204: 648-658. DOI:10.1016/j.rse.2017.09.035

Hill, E.M., Nicolau, B.A., Zimba, P.V., 2011. Habitat Management History of the Nueces Estuary, Texas, USA. Texas Water Journal, 2(1): 97-111.

Hogland, J., Anderson, N., St. Peter, J., Drake, J., Medley, P., 2018. Mapping Forest Characteristics at Fine Resolution across Large Landscapes of the Southeastern United States Using NAIP Imagery and FIA Field Plot Data. ISPRS International Journal of Geo-Information, 7(4). DOI:10.3390/ijgi7040140

Homer, C., Huang, C., Yang, L., Wylie, B., Coan, M., 2004. Development of a 2001 National Land-Cover Database for the United States. Photogrammetric Engineering & Remote Sensing, 70(7): 829-840. DOI:10.14358/PERS.70.7.829

Hu, X.F., Weng, Q.H., 2011. Impervious surface area extraction from IKONOS imagery using an object-based fuzzy method. Geocarto International, 26(1): 3-20. DOI:10.1080/10106049.2010.535616

Huang, H. et al., 2017. Mapping major land cover dynamics in Beijing using all Landsat images in Google Earth Engine. Remote Sensing of Environment, 202: 166-176. DOI:10.1016/j.rse.2017.02.021

Imen, S., Chang, N.B., Yang, Y.J., 2015. Developing the remote sensing-based early warning system for monitoring TSS concentrations in Lake Mead. J Environ Manage, 160: 73-89. DOI:10.1016/j.jenvman.2015.06.003

Imhoff, M.L., Zhang, P., Wolfe, R.E., Bounoua, L., 2010. Remote sensing of the urban heat island effect across biomes in the continental USA. Remote Sensing of Environment, 114(3): 504-513. DOI:10.1016/j.rse.2009.10.008

Irish, J.L. et al., 2010. Potential implications of global warming and barrier island degradation on future hurricane inundation, property damages, and population impacted. Ocean & Coastal Management, 53(10): 645-657. DOI:10.1016/j.ocecoaman.2010.08.001

Jeong, D.-I., Kim, Y.-O., 2005. Rainfall-runoff models using artificial neural networks for ensemble streamflow prediction. Hydrological Processes, 19(19): 3819-3835. DOI:10.1002/hyp.5983

Ji, J.-H., Chang, N.-B., 2005. Risk assessment for optimal freshwater inflow in response to sustainability indicators in semi-arid coastal bay. Stochastic Environmental Research and Risk Assessment, 19(2): 111-124. DOI:10.1007/s00477-004-0219-z

Kim, H.-C., Montagna, P.A., 2012. Effects of climate-driven freshwater inflow variability on macrobenthic secondary production in Texas lagoonal estuaries: A modeling study. Ecological Modelling, 235-236: 67-80. DOI:10.1016/j.ecolmodel.2012.03.022

Kuang, W., Chi, W., Lu, D., Dou, Y., 2014. A comparative analysis of megacity expansions in China and the U.S.: Patterns, rates and driving forces. Landscape and Urban Planning, 132: 121-135. DOI:10.1016/j.landurbplan.2014.08.015

Lavin, M.F., Godinez, V.M., Alvarez, L.G., 1998. Inverse-estuarine features of the Upper Gulf of California. Estuar. Coast. Shelf Sci., 47(6): 769-795. DOI:10.1006/ecss.1998.0387

Lee, H.K., 2017. The potential implementation of green infrastructure assessment using high-resolution National Agriculture Imagery Program data for sustainable hazard mitigation. International Journal of Sustainable Development & World Ecology, 25(4): 371-381. DOI:10.1080/13504509.2017.1409821

Lee, S., Lathrop, R.G., 2006. Subpixel analysis of Landsat ETM+ using Self-Organizing Map (SOM) neural networks for urban land cover characterization. Ieee Transactions on Geoscience and Remote Sensing, 44(6): 1642-1654. DOI:10.1109/tgrs.2006.869984

Li, H. et al., 2017. Mapping Urban Bare Land Automatically from Landsat Imagery with a Simple Index. Remote Sensing, 9(3): 249. DOI:10.3390/rs9030249

Li, X., Gong, P., Liang, L., 2015. A 30-year (1984–2013) record of annual urban dynamics of Beijing City derived from Landsat data. Remote Sensing of Environment, 166: 78-90. DOI:10.1016/j.rse.2015.06.007

Li, X., Zhou, Y., 2017. Urban mapping using DMSP/OLS stable night-time light: a review. International Journal of Remote Sensing, 38(21): 6030-6046. DOI:10.1080/01431161.2016.1274451

Li, Z., Hodges, B.R., 2015. Modeling Salnity Fluxes in the Nueces Delta, TWDB, Austin, TX.

Liu, X. et al., 2018. High-resolution multi-temporal mapping of global urban land using Landsat images based on the Google Earth Engine Platform. Remote Sensing of Environment, 209: 227-239. DOI:10.1016/j.rse.2018.02.055

Liu, Y. et al., 2017. Using data from Landsat, MODIS, VIIRS and PhenoCams to monitor the phenology of California oak/grass savanna and open grassland across spatial scales.

Agricultural and Forest Meteorology, 237-238: 311-325. DOI:10.1016/j.agrformet.2017.02.026

Lu, D.S., Weng, Q.H., 2006. Use of impervious surface in urban land-use classification. Remote Sensing of Environment, 102(1-2): 146-160. DOI:10.1016/j.rse.2006.02.010

Lu, D.S., Weng, Q.H., Li, G.Y., 2006. Residential population estimation using a remote sensing derived impervious surface approach. International Journal of Remote Sensing, 27(16): 3553-3570. DOI:10.1080/01431160600617202

Luo, J., Du, P., Alim, S., Xie, X., Xue, Z., 2014. Annual Landsat analysis of urban growth of Nanjing City from 1980 to 2013, 2014 Third International Workshop on Earth Observation and Remote Sensing Applications (EORSA), Changsha.

Maier, H.R., Jain, A., Dandy, G.C., Sudheer, K.P., 2010. Methods used for the development of neural networks for the prediction of water resource variables in river systems: Current status and future directions. Environmental Modelling & Software, 25(8): 891-909. DOI:10.1016/j.envsoft.2010.02.003

Maxwell, A.E., Warner, T.A., Vanderbilt, B.C., Ramezan, C.A., 2017. Land Cover Classification and Feature Extraction from National Agriculture Imagery Program (NAIP) Orthoimagery: A Review. Photogrammetric Engineering & Remote Sensing, 83(11): 737-747. DOI:10.14358/PERS.83.10.737

McJannet, D.L., Cook, F.J., McGloin, R.P., McGowan, H.A., Burn, S., 2011. Estimation of evaporation and sensible heat flux from open water using a large-aperture scintillometer. Water Resources Research, 47(5): n/a-n/a. DOI:10.1029/2010WR010155

Melesse, A.M., Ahmad, S., McClain, M.E., Wang, X., Lim, Y.H., 2011. Suspended sediment load prediction of river systems: An artificial neural network approach. Agricultural Water Management, 98(5): 855-866. DOI:10.1016/j.agwat.2010.12.012

Mertes, C.M., Schneider, A., Sulla-Menashe, D., Tatem, A.J., Tan, B., 2015. Detecting change in urban areas at continental scales with MODIS data. Remote Sensing of Environment, 158: 331-347. DOI:https://doi.org/10.1016/j.rse.2014.09.023

Meyer, J.L., Paul, M.J., Taulbee, W.K., 2005. Stream ecosystem function in urbanizing landscapes. Journal of the North American Benthological Society, 24(3): 602-612. DOI:10.1899/04-021.1

Midekisa, A. et al., 2017. Mapping land cover change over continental Africa using Landsat and Google Earth Engine cloud computing. PLoS One, 12(9): e0184926. DOI:10.1371/journal.pone.0184926

Mignot, E., Paquier, A., Haider, S., 2006. Modeling floods in a dense urban area using 2D shallow water equations. Journal of Hydrology, 327(1-2): 186-199. DOI:10.1016/j.jhydrol.2005.11.026

Millie, D.F. et al., 2012. Modeling microalgal abundance with artificial neural networks: Demonstration of a heuristic 'Grey-Box' to deconvolve and quantify environmental influences. Environmental Modelling & Software, 38: 27-39. DOI:10.1016/j.envsoft.2012.04.009

Milne, H., 1976. Some factors affecting egg production in waterfowl populations. Wildfowl, 27: 141-142.

Mohan, J.A., Walther, B.D., 2015. Spatiotemporal Variation of Trace Elements and Stable Isotopes in Subtropical Estuaries: II. Regional, Local, and Seasonal Salinity-Element Relationships. Estuaries Coasts, 38(3): 769-781. DOI:10.1007/s12237-014-9876-4

Montagna, P., Vaughan, B., Ward, G., 2011. The Importance of Freshwater Inflows to Texas Estuaries. In: Griffin, R.C. (Ed.), Water Policy in Texas: Responding to the Rise of Scarcity. Routledge, Washington, DC, pp. 250.

Montagna, P.A., Kalke, R.D., Ritter, C., 2002. Effect of restored freshwater inflow on macrofauna and meiofauna in upper Rincon Bayou, Texas, USA. Estuaries, 25(6B): 1436-1447. DOI:10.1007/bf02692237

Muñoz-Mas, R., Martínez-Capel, F., Garófano-Gómez, V., Mouton, A.M., 2014. Application of Probabilistic Neural Networks to microhabitat suitability modelling for adult brown trout (Salmo trutta L.) in Iberian rivers. Environmental Modelling & Software, 59: 30-43. DOI:10.1016/j.envsoft.2014.05.003

Nagel, P., Yuan, F., 2016. High-resolution Land Cover and Impervious Surface Classifications in the Twin Cities Metropolitan Area with NAIP Imagery. Photogrammetric Engineering & Remote Sensing, 82(1): 63-71. DOI:10.14358/pers.83.1.63

Neumann, B., Vafeidis, A.T., Zimmermann, J., Nicholls, R.J., 2015. Future coastal population growth and exposure to sea-level rise and coastal flooding--a global assessment. PLoS One, 10(3): e0118571. DOI:10.1371/journal.pone.0118571

NRC, 1997. Striking a Balance: Improving Stewardship of Marine Areas, National Research Council, Washington, DC.

Nuttle, W.K., Fourqurean, J.W., Cosby, B.J., Zieman, J.C., Robblee, M.B., 2000. Influence of net freshwater supply on salinity in Florida Bay. Water Resources Research, 36(7): 1805-1822. DOI:10.1029/1999wr900352

Padró, J.-C. et al., 2017. Radiometric Correction of Simultaneously Acquired Landsat-7/Landsat-8 and Sentinel-2A Imagery Using Pseudoinvariant Areas (PIA): Contributing to the Landsat Time Series Legacy. Remote Sensing, 9(12). DOI:10.3390/rs9121319

Paul, M.J., Meyer, J.L., 2001. Streams in the urban landscape. Annual Review of Ecology and Systematics, 32: 333-365. DOI:10.1146/annurev.ecolsys.32.081501.114040

Pelletier, C., Valero, S., Inglada, J., Champion, N., Dedieu, G., 2016. Assessing the robustness of Random Forests to map land cover with high resolution satellite image time series over large areas. Remote Sensing of Environment, 187: 156-168. DOI:10.1016/j.rse.2016.10.010

Piyoosh, A.K., Ghosh, S.K., 2017. Semi-automatic mapping of anthropogenic impervious surfaces in an urban/suburban area using Landsat 8 satellite data. GIScience & Remote Sensing, 54(4): 471-494. DOI:10.1080/15481603.2017.1282414

Pons, X., Pesquer, L., Cristóbal, J., González-Guerrero, O., 2014. Automatic and improved radiometric correction of Landsat imagery using reference values from MODIS surface reflectance images. International Journal of Applied Earth Observation and Geoinformation, 33: 243-254. DOI:10.1016/j.jag.2014.06.002

Powell, G.L., Matsumoto, J., Brock, D.A., 2002. Methods for Determining Minimum Freshwater Inflow Needs of Texas Bays and Estuaries. Estuaries, 25(6B): 1262-1274.

Qiu, C., Wan, Y., 2013. Time series modeling and prediction of salinity in the Caloosahatchee River Estuary. Water Resources Research, 49(9): 5804-5816. DOI:10.1002/wrcr.20415

Ridd, P.V., Stieglitz, T., 2002. Dry season salinity changes in arid estuaries fringed by mangroves and saltflats. Estuar. Coast. Shelf Sci., 54(6): 1039-1049. DOI:10.1006/ecss.2001.0876

Robins, J.B., Halliday, I.A., Staunton-Smith, J., Mayer, D.G., Sellin, M.J., 2005. Freshwater-flow requirements of estuarine fisheries in tropical Australia: a review of the state of knowledge and application of a suggested approach. Marine and Freshwater Research, 56(3): 343-360. DOI:http://dx.doi.org/10.1071/MF04087

Rouse, J.W., Haas, R.H., Schell, J.A., Deering, D.W., 1974. Monitoring vegetation systems in the Great Plains with ERTS. In: Freden, S.C., Mercanti, E.P., Becker, M.A. (Eds.), Third Earth Resources Technology Satellite-1 Symposium. NASA.

Schneider, A., Mertes, C.M., 2014. Expansion and growth in Chinese cities, 1978–2010. Environmental Research Letters, 9(2): 024008. DOI:10.1088/1748-9326/9/2/024008

Schoenbaechler, C., Guthrie, C.G., Lu, Q., 2011. Coastal Hydrology for the Laguna Madre Estuary with Emphasis on the Lower Laguna Madre, Texas Water Development Board, Austin, TX.

Sexton, J.O. et al., 2013. Urban growth of the Washington, D.C.–Baltimore, MD metropolitan region from 1984 to 2010 by annual, Landsat-based estimates of impervious cover. Remote Sensing of Environment, 129: 42-53. DOI:10.1016/j.rse.2012.10.025

Shapero, M., Dronova, I., Macaulay, L., 2017. Implications of changing spatial dynamics of irrigated pasture, California's third largest agricultural water use. Sci Total Environ, 605-606: 445-453. DOI:10.1016/j.scitotenv.2017.06.065

Shi, C., Wang, L., 2014. Incorporating spatial information in spectral unmixing: A review. Remote Sensing of Environment, 149: 70-87. DOI:10.1016/j.rse.2014.03.034

Shu, C., Burn, D.H., 2004. Artificial neural network ensembles and their application in pooled flood frequency analysis. Water Resources Research, 40: W09301. DOI:10.1029/2003wr002816

Singh, K.K., Madden, M., Gray, J., Meentemeyer, R.K., 2018. The managed clearing: An overlooked land-cover type in urbanizing regions? PLoS One, 13(2): e0192822. DOI:10.1371/journal.pone.0192822

Small, C., 2002. Multitemporal analysis of urban reflectance. Remote Sensing of Environment, 81(2): 427-442. DOI:https://doi.org/10.1016/S0034-4257(02)00019-6

Sumner, D.M., Belaineh, G., 2005. Evaporation, precipitation, and associated salinity changes at a humid, subtropical estuary. Estuaries, 28(6): 844-855. DOI:10.1007/bf02696014

Sun, H., Koch, M., 2001. Case Study: Analysis and Forecasting of Salinity in Apalachicola Bay, Florida, Using Box-Jenkins ARIMA Models. Journal of Hydraulic Engineering, 127(9): 718-727. DOI:doi:10.1061/(ASCE)0733-9429(2001)127:9(718)

Sun, T., Zhang, H., Yang, Z., Yang, W., 2015. Environmental flow assessments for transformed estuaries. Journal of Hydrology, 520: 75-84. DOI:http://dx.doi.org/10.1016/j.jhydrol.2014.11.015

Sun, Z., Wang, C., Guo, H., Shang, R., 2017. A Modified Normalized Difference Impervious Surface Index (MNDISI) for Automatic Urban Mapping from Landsat Imagery. Remote Sensing, 9(9): 942. DOI:10.3390/rs9090942

Torbick, N., Corbiere, M., 2015. Mapping urban sprawl and impervious surfaces in the northeast United States for the past four decades. GIScience & Remote Sensing, 52(6): 746-764. DOI:10.1080/15481603.2015.1076561

Ucar, Z., Bettinger, P., Merry, K., Akbulut, R., Siry, J., 2018. Estimation of urban woody vegetation cover using multispectral imagery and LiDAR. Urban Forestry & Urban Greening, 29: 248-260. DOI:10.1016/j.ufug.2017.12.001

Vermote, E., Justice, C., Claverie, M., Franch, B., 2016. Preliminary analysis of the performance of the Landsat 8/OLI land surface reflectance product. Remote Sensing of Environment, 185: 46-56. DOI:10.1016/j.rse.2016.04.008

Vogl, T.P., Mangis, J.K., Rigler, A.K., Zink, W.T., Alkon, D.L., 1988. Accelerating the convergence of the back-propagation method. Biological Cybernetics, 59(4): 257-263. DOI:10.1007/bf00332914

Wan, Y., Wan, C., Hedgepeth, M., 2015. Elucidating multidecadal saltwater intrusion and vegetation dynamics in a coastal floodplain with artificial neural networks and aerial photography. Ecohydrology, 8(2): 309-324. DOI:10.1002/eco.1509

Wang, J., Deng, Z., 2016. Modeling and Prediction of Oyster Norovirus Outbreaks along Gulf of Mexico Coast. Environ Health Perspect, 124(5): 627-33. DOI:10.1289/ehp.1509764

Wang, J., Song, J.W., Chen, M.Q., Yang, Z., 2015. Road network extraction: a neural-dynamic framework based on deep learning and a finite state machine. International Journal of Remote Sensing, 36(12): 3144-3169. DOI:10.1080/01431161.2015.1054049

Weng, Q., 2012. Remote sensing of impervious surfaces in the urban areas: Requirements, methods, and trends. Remote Sensing of Environment, 117: 34-49. DOI:10.1016/j.rse.2011.02.030

Wetz, M.S., Hayes, K.C., Fisher, K.V., Price, L., Sterba-Boatwright, B., 2016. Water quality dynamics in an urbanizing subtropical estuary(Oso Bay, Texas). Mar Pollut Bull, 104(1-2): 44-53. DOI:10.1016/j.marpolbul.2016.02.013

WHO, 2016. Global report on urban health: equitable, healthier cities for sustainable development.

Wickham, J.D. et al., 2013. Accuracy assessment of NLCD 2006 land cover and impervious surface. Remote Sensing of Environment, 130: 294-304. DOI:10.1016/j.rse.2012.12.001

Woodward, B.D. et al., 2018. CO-RIP: A Riparian Vegetation and Corridor Extent Dataset for Colorado River Basin Streams and Rivers. ISPRS International Journal of Geo-Information, 7(10). DOI:10.3390/ijgi7100397

Wu, C., 2004. Normalized spectral mixture analysis for monitoring urban composition using ETM+ imagery. Remote Sensing of Environment, 93(4): 480-492. DOI:https://doi.org/10.1016/j.rse.2004.08.003

Wu, Q. et al., 2019. Integrating LiDAR data and multi-temporal aerial imagery to map wetland inundation dynamics using Google Earth Engine. Remote Sensing of Environment, 228: 1-13. DOI:10.1016/j.rse.2019.04.015

Wu, W., Dandy, G.C., Maier, H.R., 2014. Protocol for developing ANN models and its application to the assessment of the quality of the ANN model development process in drinking water quality modelling. Environmental Modelling & Software, 54: 108-127. DOI:10.1016/j.envsoft.2013.12.016

Wulder, M.A. et al., 2019. Current status of Landsat program, science, and applications. Remote Sensing of Environment, 225: 127-147. DOI:10.1016/j.rse.2019.02.015

Xian, G., Homer, C., 2010. Updating the 2001 National Land Cover Database Impervious Surface Products to 2006 using Landsat Imagery Change Detection Methods. Remote Sensing of Environment, 114(8): 1676-1686. DOI:10.1016/j.rse.2010.02.018

Xu, H., 2006. Modification of normalised difference water index (NDWI) to enhance open water features in remotely sensed imagery. International Journal of Remote Sensing, 27(14): 3025-3033. DOI:10.1080/01431160600589179

Xu, J. et al., 2018. Measuring spatio-temporal dynamics of impervious surface in Guangzhou, China, from 1988 to 2015, using time-series Landsat imagery. Sci Total Environ, 627: 264-281. DOI:10.1016/j.scitotenv.2018.01.155

Yáñez-Arancibia, A., Day, J.W., 2004. The Gulf of Mexico: towards an integration of coastal management with large marine ecosystem management. Ocean & Coastal Management, 47(11–12): 537-563. DOI:http://dx.doi.org/10.1016/j.ocecoaman.2004.12.001

Yang, F., Matsushita, B., Fukushima, T., 2010. A pre-screened and normalized multiple endmember spectral mixture analysis for mapping impervious surface area in Lake Kasumigaura Basin, Japan. ISPRS Journal of Photogrammetry and Remote Sensing, 65(5): 479-490. DOI:https://doi.org/10.1016/j.isprsjprs.2010.06.004

Zha, Y., Gao, J., Ni, S., 2003. Use of normalized difference built-up index in automatically mapping urban areas from TM imagery. International Journal of Remote Sensing, 24(3): 583-594. DOI:10.1080/01431160304987

Zhou, Z.H., Wu, J.X., Tang, W., 2002. Ensembling neural networks: Many could be better than all. Artificial Intelligence, 137(1-2): 239-263. DOI:10.1016/s0004-3702(02)00190-x

Zhu, Z. et al., 2016. Including land cover change in analysis of greenness trends using all available Landsat 5, 7, and 8 images: A case study from Guangzhou, China (2000–2014). Remote Sensing of Environment, 185: 243-257. DOI:10.1016/j.rse.2016.03.036

Supplementary Information

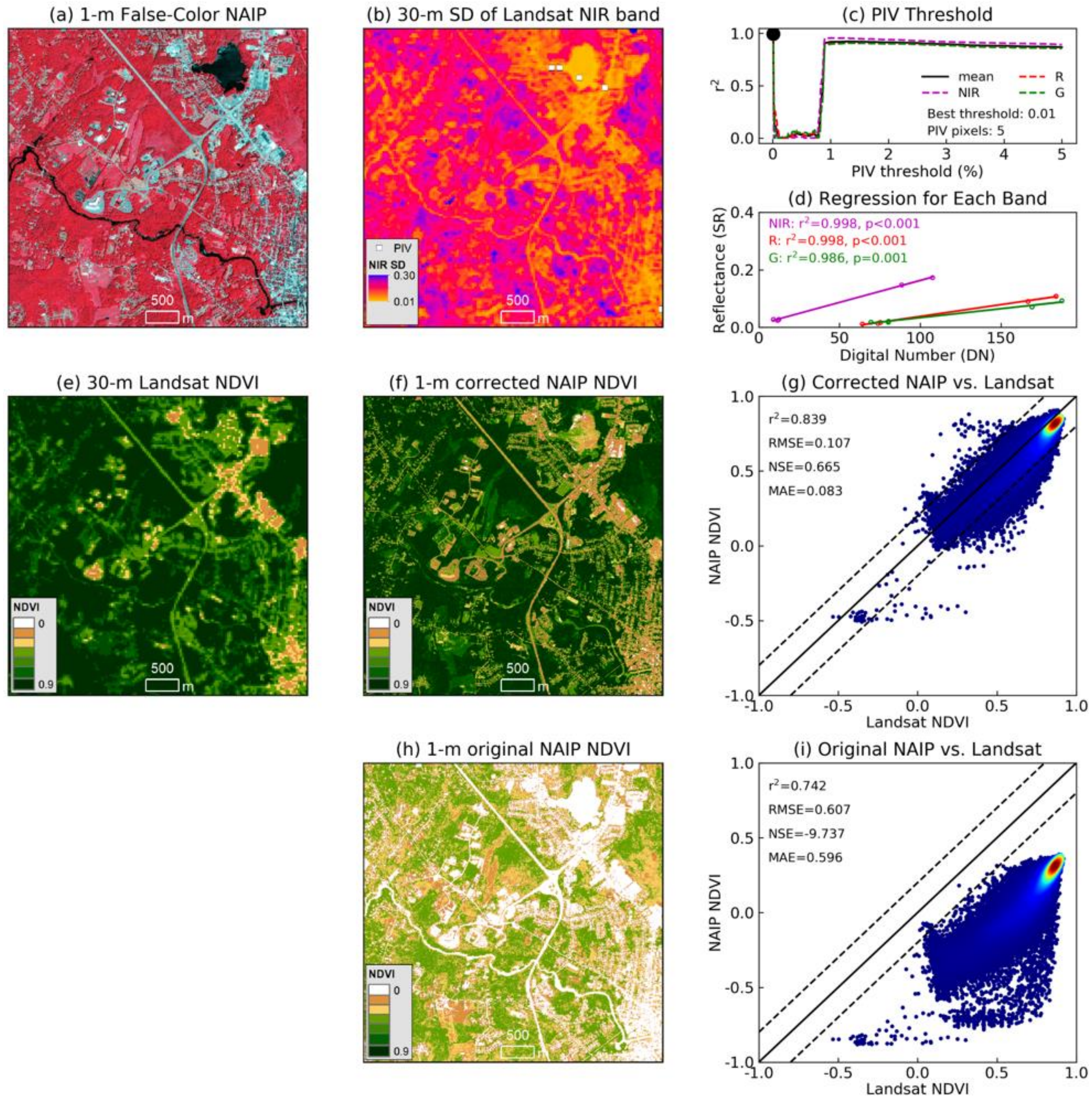

Figure S1. Application of PINT at the test site 3.

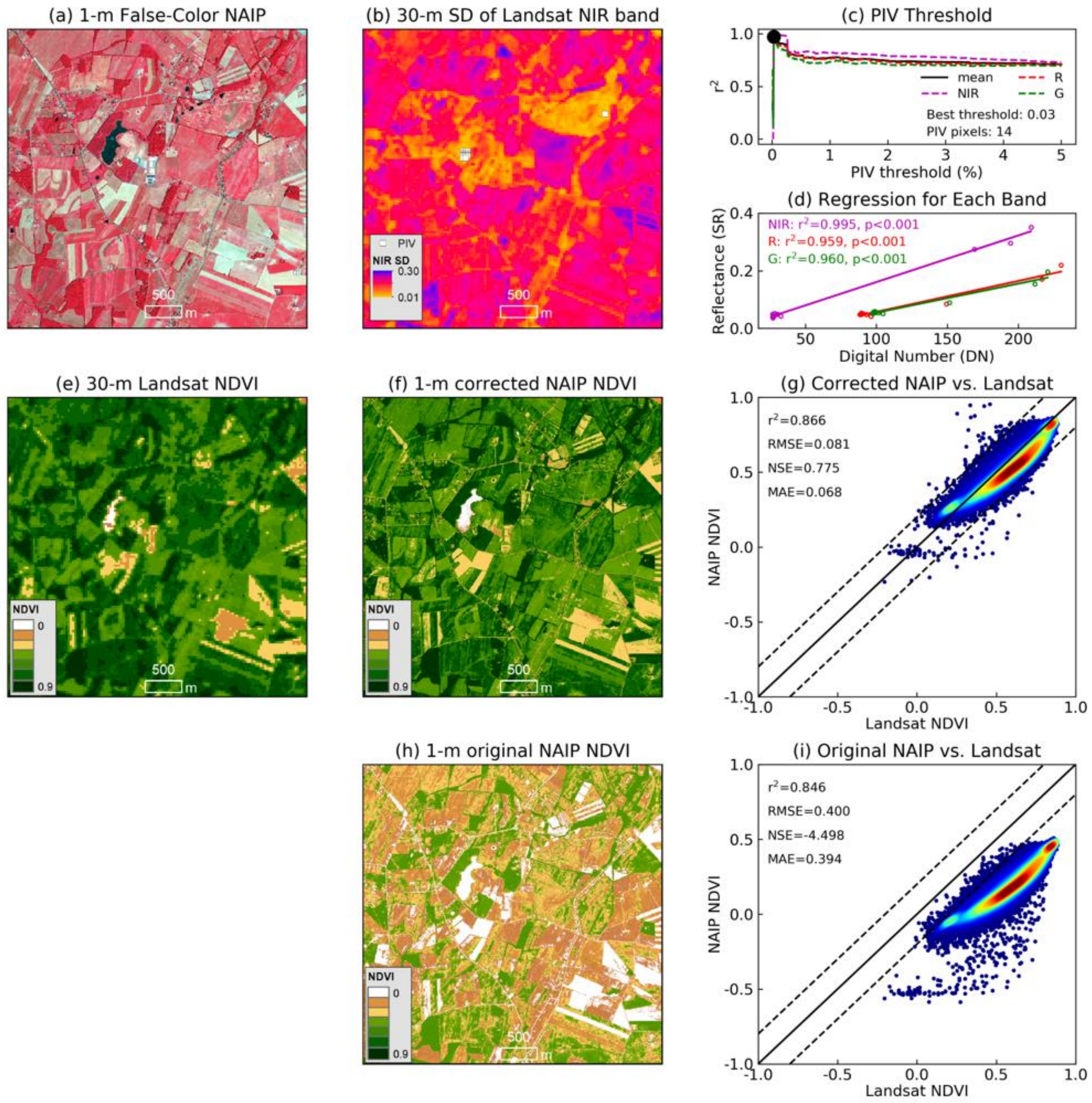

Figure S2. Application of PINT at the test site 4.

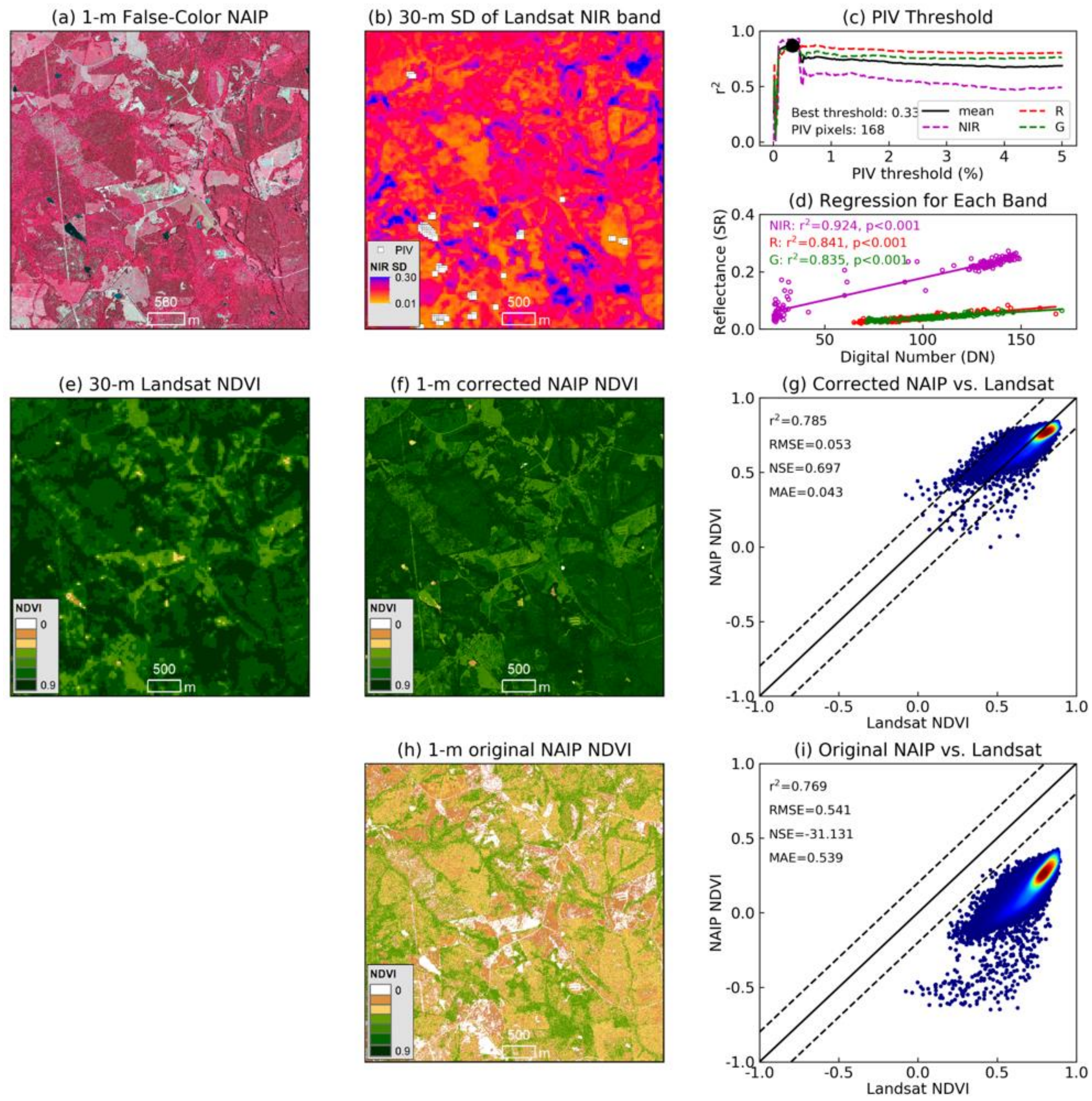
(a) 1-m False-Color NAIP

(b) 30-m SD of Landsat NIR band

(c) PIV Threshold

(d) Regression for Each Band

(e) 30-m Landsat NDVI

(f) 1-m corrected NAIP NDVI

(g) Corrected NAIP vs. Landsat

(h) 1-m original NAIP NDVI

(i) Original NAIP vs. Landsat

Figure S3. Application of PINT at the test site 5.

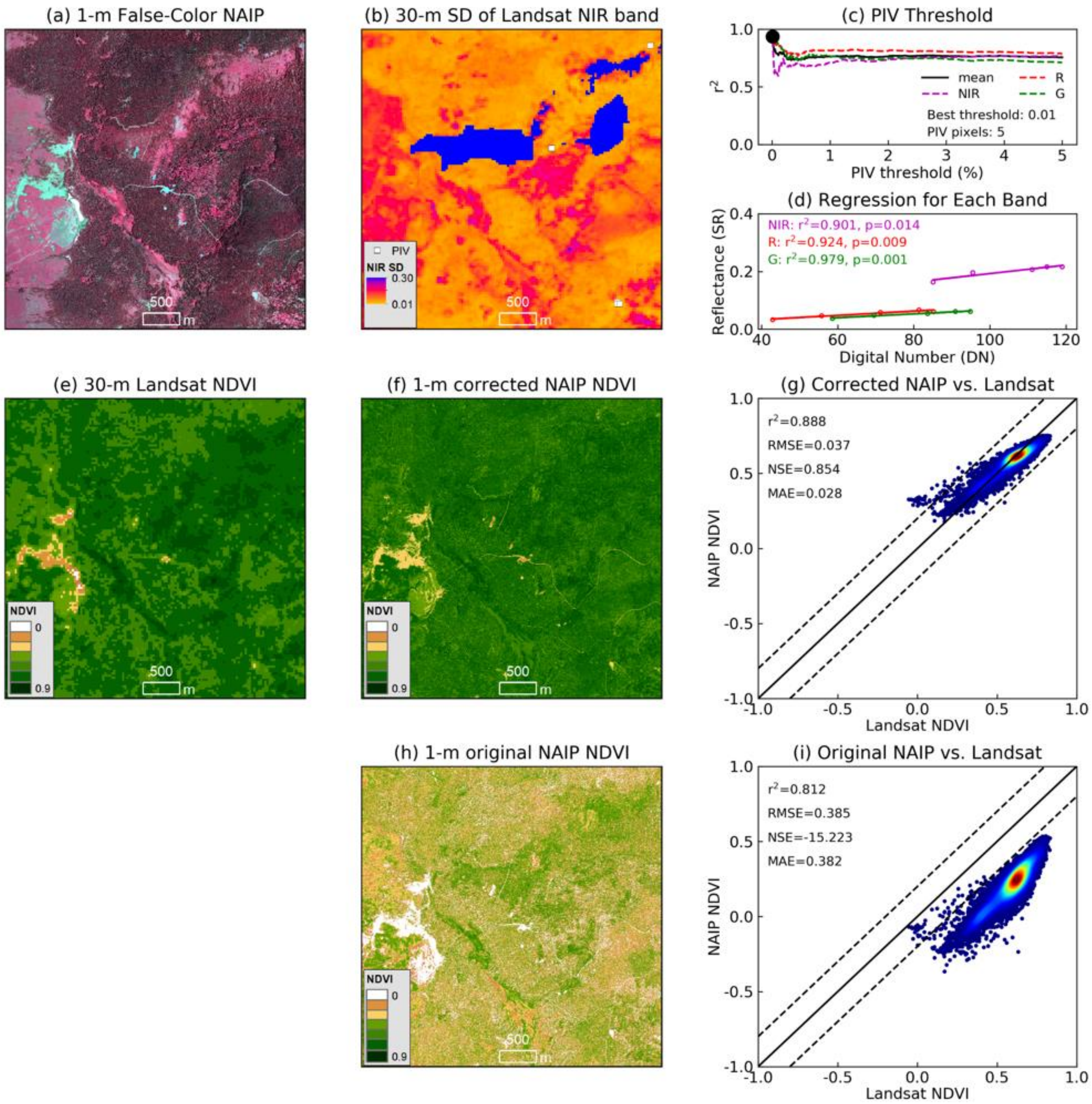

Figure S4. Application of PINT at the test site 6.

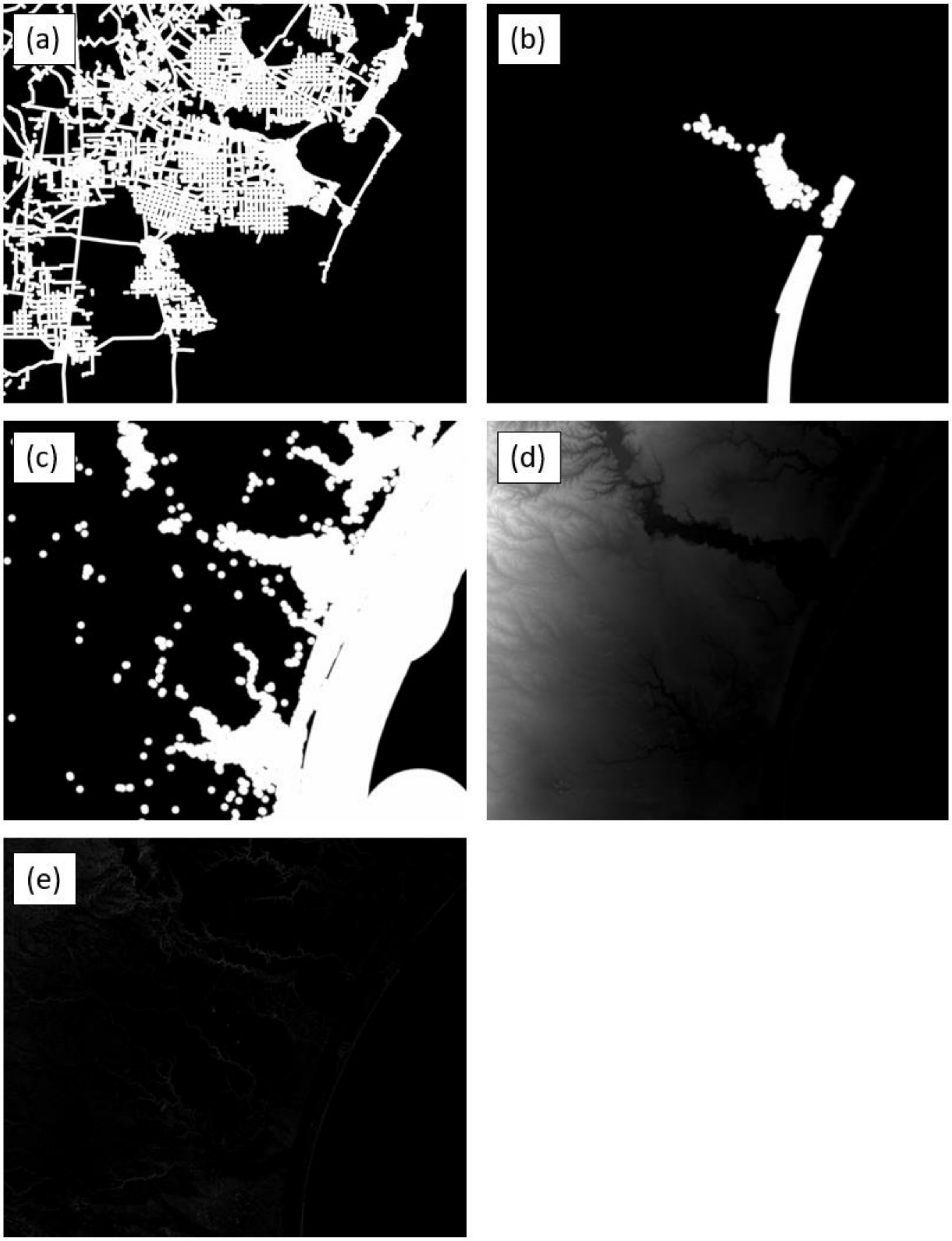

Figure S5. Predictor variables for the MCCA model.

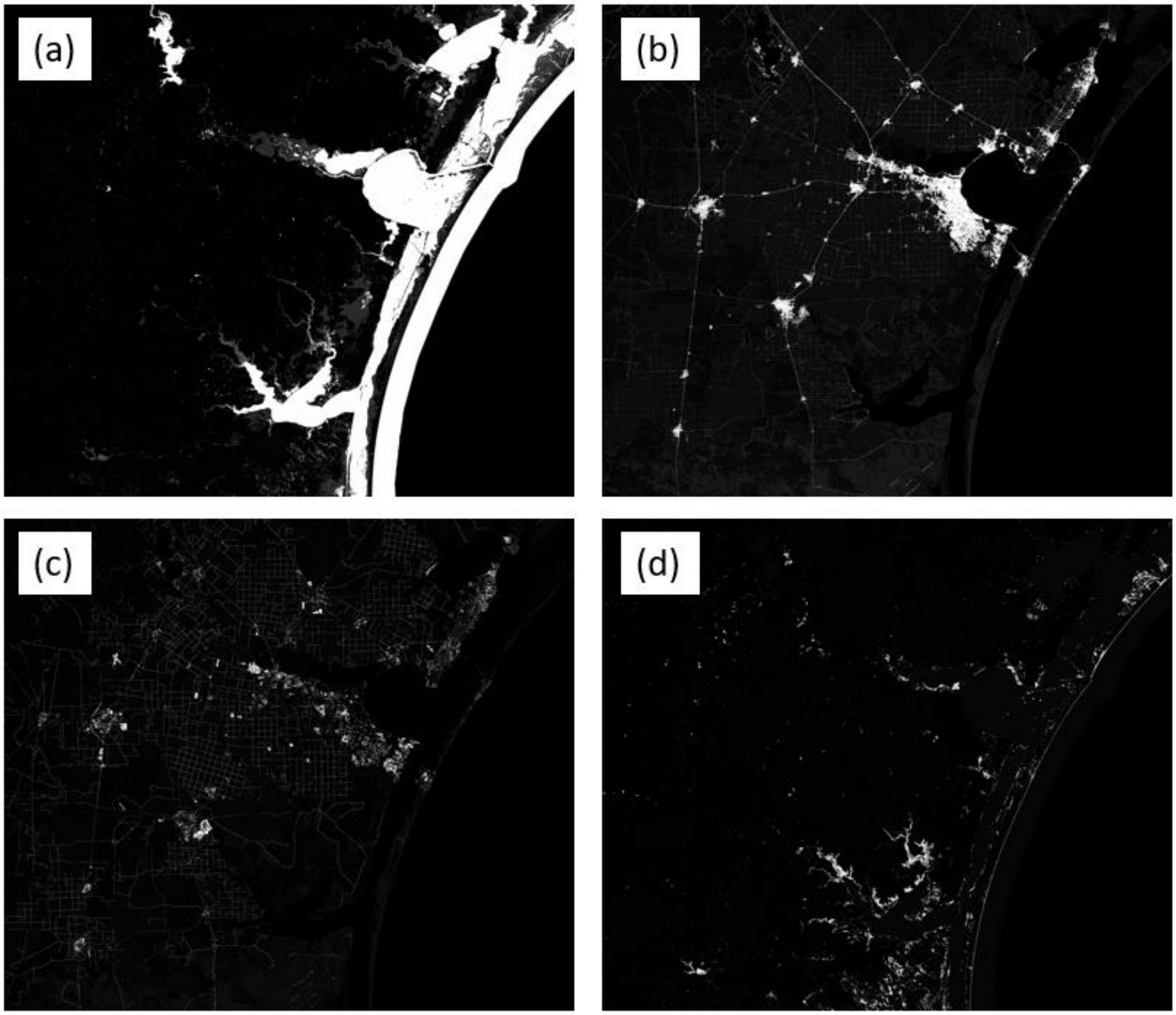

Figure S6. Conditional probability maps for the change classes 1, 2, 3, and 4 from the MCCA model.

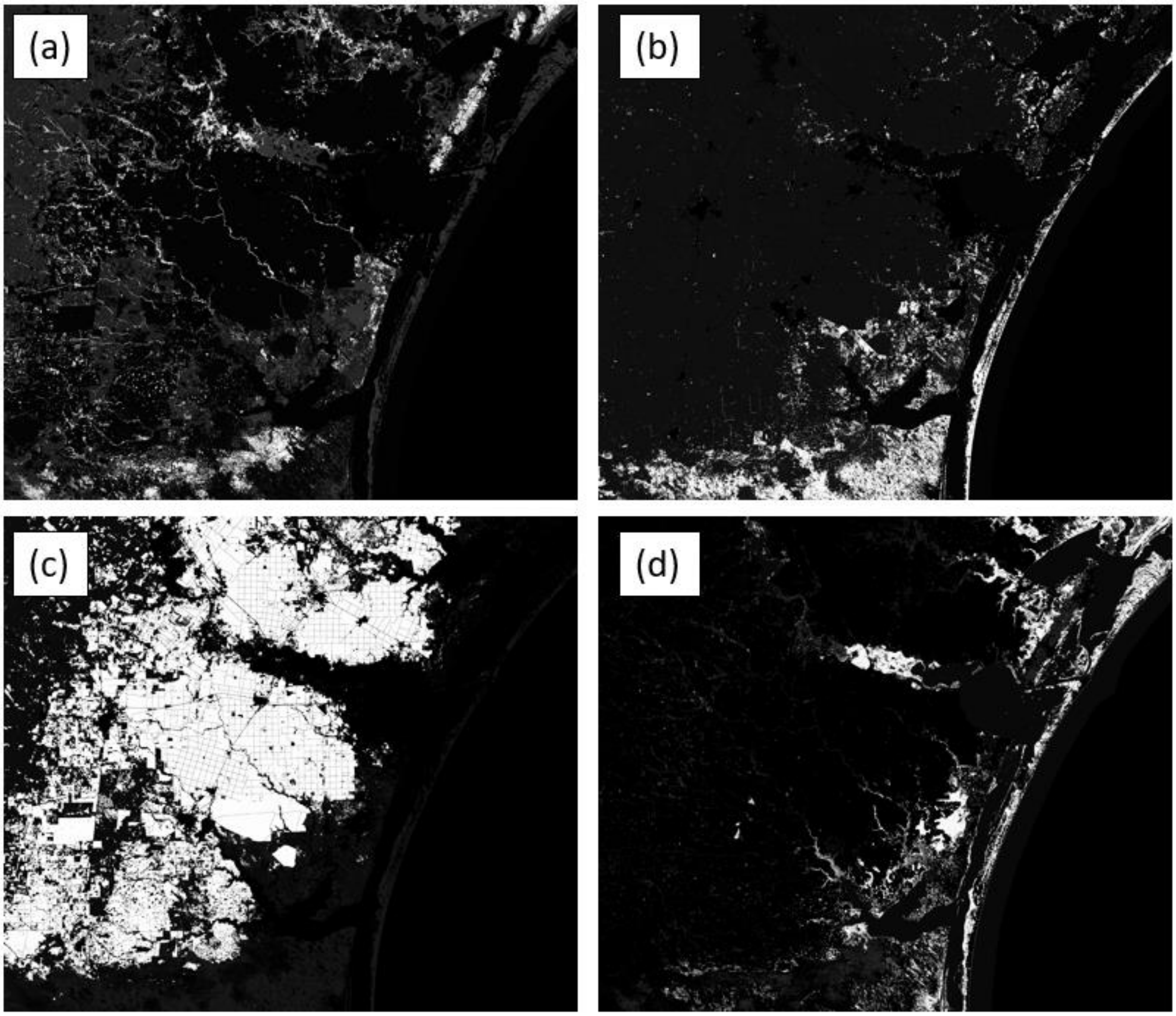

Figure S7. Conditional probability maps for the change classes 5, 7, 8, and 9 from the MCCA model.